Aus der Universitäts-Augenklinik
der Universitätsmedizin Rostock

Challenges in the Evaluation of Multifocal Intraocular Lenses

Kumulative Dissertation
zur Erlangung des akademischen Grades
Doctor medicinae (Dr. med.)

vorgelegt der Medizinischen Fakultät der Universität Rostock
von

Ricardo Elsner
geb. am 26.06.1998 in Dresden

Rostock, den 25.10.2025

https://doi.org/10.18453/rosdok_id00005805

Gutachter

1. Gutachter: Prof. Dr.-Ing. Niels Grabow — Universitätsmedizin Rostock

2. Gutachter: Prof. Dr. Achim Langenbucher — Universität des Saarlandes

3. Gutachter: Prof. Dr. rer. nat. Oliver Stachs — Universitätsmedizin Rostock

Datum der Einreichung: 25.10.2025

Datum der Verteidigung: 28.04.2026

Table of Contents

List of Abbreviations

ANSI .... American National Standards Institute

CMOS .... Complementary Metal-Oxide Semiconductor

CIE .... International Commission on Illumination

CSI .... Cross-Sectional Images

DMIOL .... Diffractive Multifocal Intraocular Lens

EDOF .... Extended Depth of Focus

HDR .... High Dynamic Range

ISO .... International Organization for Standardization

IOL .... Intraocular Lens

LCA .... Longitudinal Chromatic Aberration

LED .... Light Emitting Diode

MIOL .... Multifocal IOL

MPE .... Maximum Permissible Exposure

MTF .... Modulation Transfer Function

NIR .... Near-Infrared Light

PMMA .... Polymethylmethacrylat

PSF .... Point Spread Function

RA-CSI .... Rotationally Averaged Cross-Sectional Image

SNR .... Signal-to-Noise-Ratio

TFC .... Through-Focus-Curve

1. Introduction

The primary cause of blindness worldwide, as per the World Health Organization, are cataracts [1]. A cataract is an opacification or clouding of the eye's natural crystalline lens, most commonly due to age-related changes in lens proteins and cumulative oxidative damage [2]. This process leads to progressive, painless visual impairment, including blurring, glare, and reduced contrast sensitivity [3]. Cataract surgery, one of the most commonly performed procedures worldwide, involves replacing the natural lens of the eye with an artificial intraocular lens (IOL). The development and design of IOLs trace back to the 1940s, inspired by observations that World War II pilots with fragments of airplane cockpit glass in their eyes exhibited minimal inflammatory reactions, indicating the material's ocular biocompatibility. Sir Harold Ridley noted that these fragments were made of polymethylmethacrylate (PMMA) which was essential in his decision to use PMMA as the material for the first IOL. Then in 1949, the first IOLs were implanted by Ridley, marking the beginning of a transformative era in cataract surgery and visual rehabilitation [4].

Despite initial skepticism and resistance from the ophthalmic community, IOLs gradually gained acceptance, particularly after improvements in surgical technique and lens design in the 1970s and 1980s [5,6]. The 1970s came with rapid innovation, with the introduction of anterior and posterior chamber lenses and the rise of major manufacturers. The transition from rigid PMMA to foldable silicone and acrylic polymers enabled smaller incisions, faster recovery, and complemented the development of phacoemulsification [7–9]. Subsequent decades brought further refinements, including heparin-coated surfaces to reduce postoperative inflammation and the advent of multifocal and accommodating IOLs to address presbyopia [10,11]. Recent decades have focused on optimizing optical quality, biocompatibility, and customization, with ongoing research into new materials and advanced-technology IOLs, e.g., multifocal IOLs (MIOLs) or extended depth of focus (EDOF) IOLs [9,12,13].

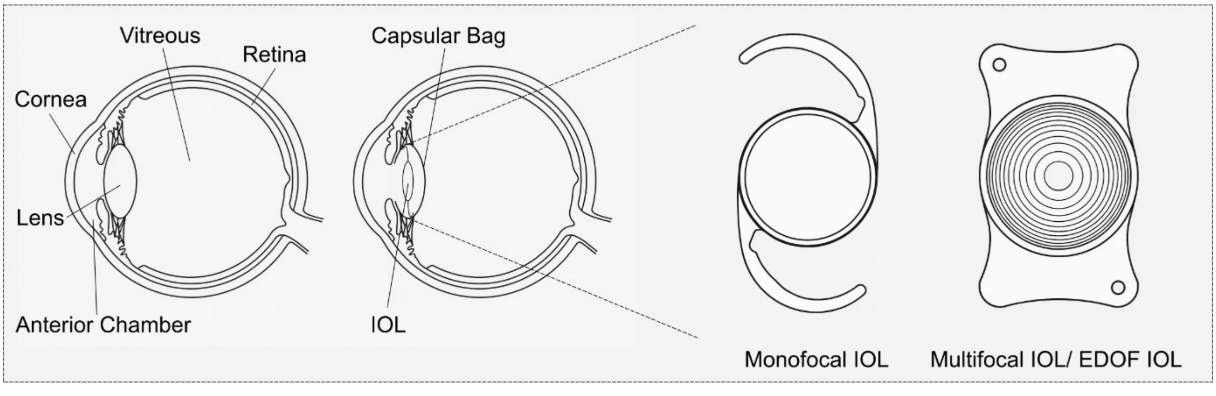

Figure 1: Scheme of IOL implantation into the human eye. From left to right: schematic representation of the anatomy of the human eye; IOL implantation into the capsular bag after removal of the crystalline lens; scheme of a monofocal IOL with C-haptics; scheme of a multifocal or EDOF IOL with diffractive zone pattern on the surface (Source: Created by the author).

Fig. 1 shows an example of the implantation of an IOL into the capsular bag after removal of the crystalline lens. Currently, in 2025, patients and doctors in Germany can choose between more than 200 IOL designs from more than 20 different manufacturers (https://www.iol-finder.de, an open-source e-book). While monofocal IOLs provide clear vision at a single distance, generally for far vision, patients often require spectacles for other distances, generally for near and intermediate vision. MIOLs, on the other hand, offer the promise of spectacle independence by providing multiple focal points, achieved through refractive, diffractive, or hybrid principles [12,14–17].

The basic principle behind trifocal IOLs is the division of incoming light into three distinct focal points (far, intermediate, and near) using diffractive or refractive optical designs. This allows for improved spectacle independence across a range of visual tasks, particularly enhancing intermediate vision compared to earlier bifocal designs, which only provided distance and near focus. Trifocal IOLs achieve this for example by incorporating multiple diffractive steps or zones on the lens surface (based on the Fresnel zone plate), each corresponding to a different focal length, thereby distributing light intensity to all three foci simultaneously. Such designs, however, can be associated with increased photic phenomena such as halos and glare, and may reduce contrast sensitivity compared to monofocal lenses [18–22]. Fig. 2 gives an overview on the aforementioned optic principles.

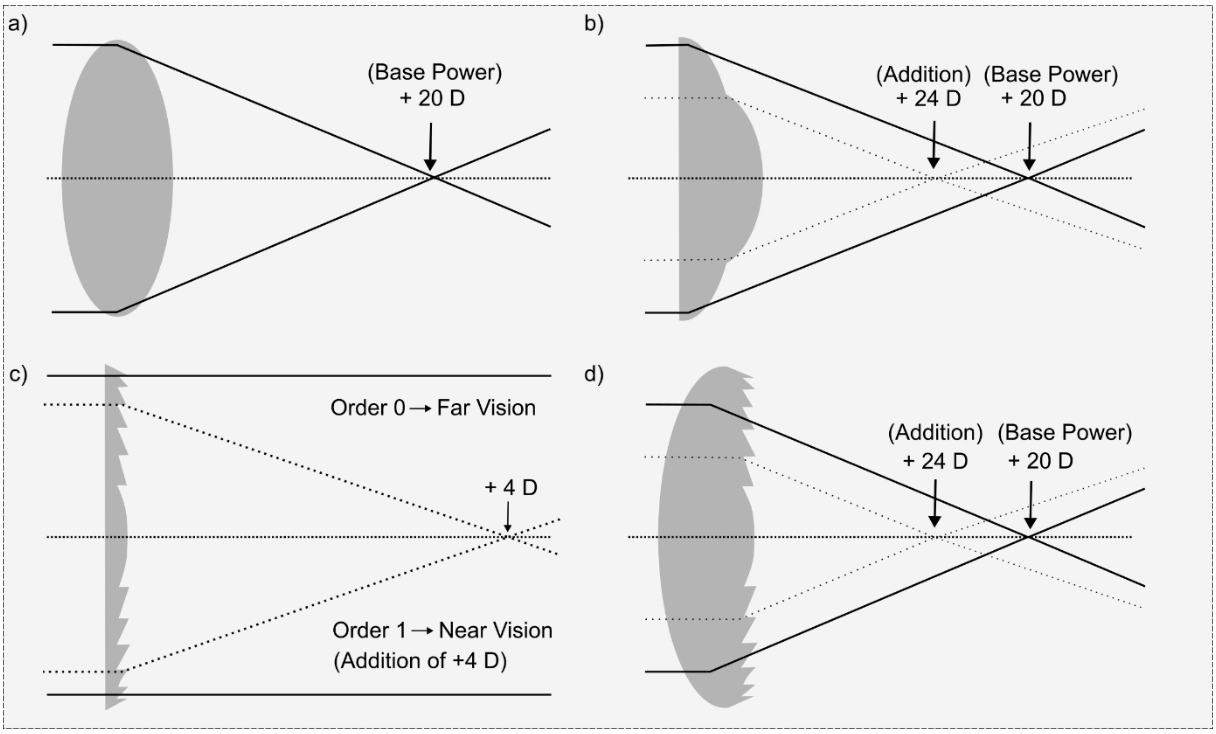

Figure 2: Principles of refractive and diffractive optics in IOLs. a) shows a monofocal refractive IOL with a base power of +20 D; b) shows a bifocal refractive MIOL with an additional power of +4 D in the center; c) depicts a diffraction surface profile based on the Fresnel zone plate resulting in an additional focus induced by the 1st diffraction order; d) gives an example of a bifocal MIOL with a refractive base power of +20 D and a diffractive additional power for near vision; D = diopters (Source: Created by the author).

EDOF IOLs use optical engineering, such as echelette diffractive patterns, manipulation of spherical aberration, or small-aperture designs, to create a single elongated focal point rather than multiple discrete foci and to minimize the drop in visual acuity between focal points [12]. Contrary to multifocal IOLs, this is supposed to result in a continuous range of clear vision, especially from distance to intermediate, with some functional near vision, with the intention to reduce the risk of dysphotopsias (halos, glare) and contrast loss compared to MIOLs [19,21–23]. According to the German Society of Cataract and Refractive Surgery, the proportion of all multifocal and EDOF IOLs (including presbyopia-correcting toric IOLs) was 6.9 % in 2022/2023, while in previous years, between 2.6% and 5.5% of all implants had been multifocal lenses [24,25]. Despite their advantages, patients implanted with MIOLs often experience dysphotopsias, particularly under low-light conditions, e.g. while driving at night [26,27].

The perception of halos is influenced by various factors, including the spectral characteristics of the light source, the lens design, and the human visual system's sensitivity to glare. To evaluate and quantify glare symptoms, Meikis et al. developed the Rostock Glare Perimeter method to measure age-related differences in disability glare and to detect binocular summation effects in healthy individuals, particularly at small visual field angles with high angular resolution [28].

Traditional methods of studying halos rely on subjective feedback from patients through questionnaires [29,30] or interactive simulators [31,32]. However, these approaches are limited by the inherent subjectivity of human perception. Objective methods, such as the use of camera-based systems, provide complementary insights but require calibration to align with the logarithmic nature of human visual perception [33].

The experimental evaluation of IOLs is essential to verify their imaging properties and assess their performance against manufacturers' claims. Optical benches have become the standard for preclinical testing, enabling the analysis of key metrics such as modulation transfer functions (MTFs), point spread functions (PSFs), and through-focus energy distributions [34–38]. The PSF describes how a point source of light is imaged by an optical system and also accounts for optical aberrations. In that context, the Airy disc is the ideal, diffraction-limited case of the PSF for a circular aperture. A narrower and more concentrated PSF indicates better optical quality and less light scatter, correlating with sharper retinal images. PSF is particularly useful for assessing the degree of halos and glare, which are relevant for multifocal and trifocal IOLs [22,39]. The MTF quantifies the ability of an IOL to transfer contrast at different spatial frequencies from the object to the image. Higher MTF values at a given spatial frequency indicate better contrast and resolution. The MTF is measured at various focal points to compare the optical quality of monofocal, trifocal, and EDOF IOLs.

Defocus curves plot subjective visual acuity as a function of defocus (diopters), providing a profile of functional vision across different distances, while through focus curves objectively plot the light intensity along the optical axis over a range of distances. Trifocal IOLs show three distinct peaks corresponding to their three focal points, while EDOF IOLs demonstrate a smoother, plateau-like curve, indicating continuous vision over a range of distances but typically less near acuity than trifocal IOLs [40,41].

These metrics are essential for comparing IOL designs. The introduction of ISO standard 11979-2 in 2000 established guidelines for optical bench setups, ensuring consistency and comparability across studies. The current standards are described by guidelines from 2024 [42]. Modern optical benches allow for the capture of three-dimensional point spread functions (3D-PSFs), providing detailed insights into the light distribution caused by IOLs. A 3D-PSF is a three-dimensional representation of how an optical system (such as an IOL or microscope objective) responds to a point source of light. This data can be used to calculate cross-sectional images (CSIs) which are two-dimensional slices through the 3D-PSF generated by an IOL. These images visualize how light from a point source is distributed in space after passing through the lens, providing a direct, spatial representation of the lens's focusing properties and aberrations.

While CSI-techniques such as the fluorescein bath method [43,44] and optical bench light sheet-based imaging [45] are well-established, they are limited by the finite width of the light sheet or extracted volume, reducing image quality and signal-to-noise ratio [40,44,46].

This work builds on these techniques and demonstrates IOL performance results from an in-house optical bench and a novel algorithm – improving the quality of CSIs and enabling more accurate comparisons between MIOL designs under varying conditions.

Additionally, we show that the performance of MIOLs is highly wavelength-dependent, as diffractive efficiency decreases with longer wavelengths [47,48]. While most MIOLs are optimized for green light (546 ±10 nm) due to the eye's peak sensitivity [49], clinical evaluations often employ near-infrared (NIR) light (780–1000 nm) for its practical advantages, such as the low NIR sensitivity of the human retina with reduced glare and increased retinal reflectivity [50,51]. This wavelength mismatch introduces challenges in assessing optical performance. In some MIOLs, NIR light disproportionately directs energy into the far focus, compromising the functionality of the near and intermediate foci. Studies have shown that this leads to discrepancies in wavefront aberrometry and double-pass measurements, potentially misrepresenting the IOL's true optical behavior [52–55].

The challenges in evaluating MIOLs extend beyond optical bench setups and photic phenomena to include discrepancies in simulation and measurement data. While prior studies have used experimentally derived surface topography data for simulations [55,56], this work employs manufacturer-specified surface profiles to improve accuracy of optics simulations for the investigated IOL. This approach enables a more precise analysis of wavelength- and pupil-size-dependent effects on diffraction efficiency and order distribution in an optical bench setup.

2. Purpose of work

This research addresses critical challenges in evaluating the optical and perceptual performance of multifocal intraocular lenses (MIOLs) at the example of the diffractive trifocal AT Lisa Tri 839MP (Carl Zeiss Meditec AG, Berlin, Germany). By employing a new approach and comparative analyses, it bridges the gaps between experimental setups, simulation techniques, and clinical applications.

A key focus is improving optical bench methods traditionally used for MIOL evaluation. While light sheet-based techniques, including those in optical benches [45] or those using fluorescein/ouzo/milk baths [43,44], have been widely used to visualize CSIs of IOLs, these setups are limited by the finite thickness of the light sheet, which reduces image quality and obscures fine structures.

This research uses a novel image-processing algorithm that uses the rotational symmetry of IOL designs to enhance the quality of CSIs derived from optical bench data. Comparative analyses between the new method and the conservative fluorescein bath approach demonstrate advantages in terms of fine feature visibility, and overall image clarity. By automating the acquisition of 3D-PSFs and applying this algorithm, the study provides a more accurate representation of the optical properties of rotationally symmetric MIOLs.

Further, this work explores the wavelength-dependent behavior of diffractive MIOLs, particularly under near-infrared (NIR) illumination, using the AT LISA Tri 839MP as a model. The research demonstrates that the investigated IOL's near and intermediate foci substantially lose in intensity under NIR illumination, effectively making the IOL monofocal. These findings underscore the importance of visible-light-based techniques (400 - 700 nm) for accurate MIOL evaluation and warn against methodological flaws in NIR-based assessments.

By using true surface topography data in comparative optical simulations, this research provides valuable insights into the wavelength-dependent performance of the investigated IOL. Through these contributions, this work advances understanding and evaluation methods, paving the way for improved patient outcomes in cataract and presbyopia treatments.

3. Methods

3.1. IOLs and model corneas

The studied IOLs were a diffractive trifocal IOL (AT LISA tri 839MP, Carl Zeiss Meditec AG, Jena, Germany) with a base refractive power of +22.5 D for the far focus, and additional powers of +3.33 D for near focus and +1.66 D for intermediate focus [Pub. I and II] and the same IOL with an optical base power of +25.0 D [Pub. III]. The investigated IOL type is a rotationally symmetric IOL which essentially means that its optical design and properties are identical at every meridian around its optical axis; in other words, its structure and refractive or diffractive features are invariant with rotation about the center of the lens. This symmetry means that, apart from mechanical imprecision, the IOL's optical performance, such as PSF, MTF, and through-focus curve does not change with the orientation of the lens in the eye or on the optical bench.

The model corneas used in the experiments are designed to replicate the optical properties of the human cornea, including refractive power and spherical aberration. The model cornea used in the fluorescein bath setup (MC 1) [Pub. II] is made of PMMA and has an anterior surface radius of 9.1 mm and a posterior surface radius of 6.5 mm. The anterior surface is shaped as a prolate ellipsoid with a negative asphericity of -0.4. It has a refractive index of 1.492. Within the optical bench setup [Pub. I and Pub. III] the VirtIOL model cornea (MC 2) (Edmund Optics, Barrington, USA), an achromatic lens with an effective focal length of 40 mm and neutral spherical aberration, was integrated into the model eye. Both used model corneas have identical optical properties.

3.2. Cross sectional imaging techniques for IOLs

3.2.1. Fluorescein bath light sheet method

In this technique, a thin sheet of light illuminates the IOL placed within a fluorescein-filled bath, positioned behind a model cornea (MC 1). The excitation of fluorescein highlights the light distribution through a diffractive trifocal IOL. A camera, aligned perpendicularly to the light sheet, is centered on its plane, captures the emitted light resulting from scattering and fluorescence. The observed intensity distribution in the CSIs depends on both the thickness of the light sheet and the degree of decentering or tilting of the IOL.

The setup uses a 532 nm laser diode as a light source. A 3.5 mm diameter round laser beam is reduced by a factor of ten by the beam expander and then focused through a converging lens onto a Powell lens, which transforms the Gaussian beam into a flat-top intensity profile, creating a uniform light sheet with a thickness of 0.35 mm. To collimate the diverging beam, a cylindrical lens is positioned after the Powell lens. An adjustable iris diaphragm further controls the length of the laser line, set to 5 mm for this experiment. Fig. 3 gives a schematic overview of the fluorescein bath setup based on the works of Reiß et al. [43].

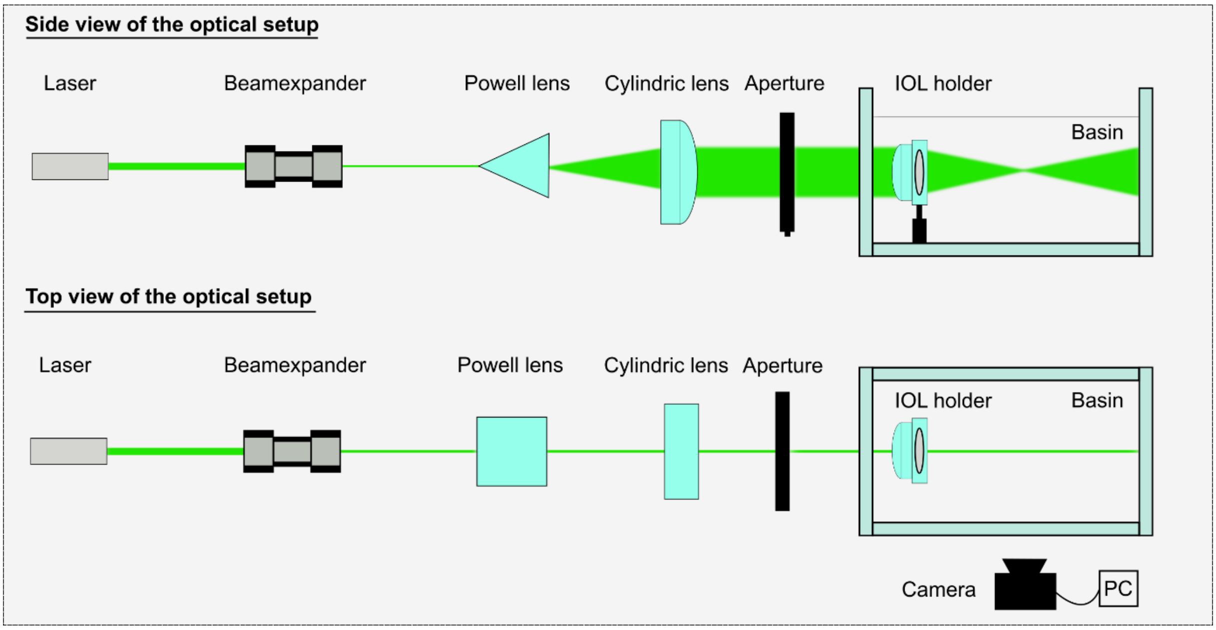

Figure 3: Scheme of the fluorescein bath method. Side (top) and top (bottom) views of the optical setup for the fluorescein bath method. A laser beam is passing a beam expander, shaped into a light sheet by a Powell lens, and further collimated by a cylindrical lens before passing through an adjustable aperture. The light-sheet then illuminates the IOL integrated into an IOL holder with a model cornea - all immersed in a fluorescein-filled basin. The resulting light distribution is recorded by a camera and analyzed via a connected computer (Source: Created by the author).

The collimated light sheet passes through the model cornea and the MIOL in the fluorescein solution (see Fig. 4 a). The model cornea design follows the principles outlined by Holladay et al. [57]. The focal points formed by the MIOL are visible within the CSI of the fluorescein bath (highlighted in Fig. 4 b). The magnified section in Fig. 4 c) shows both the near and far foci by tracing the beam path, as schematically represented in Fig. 4 a).

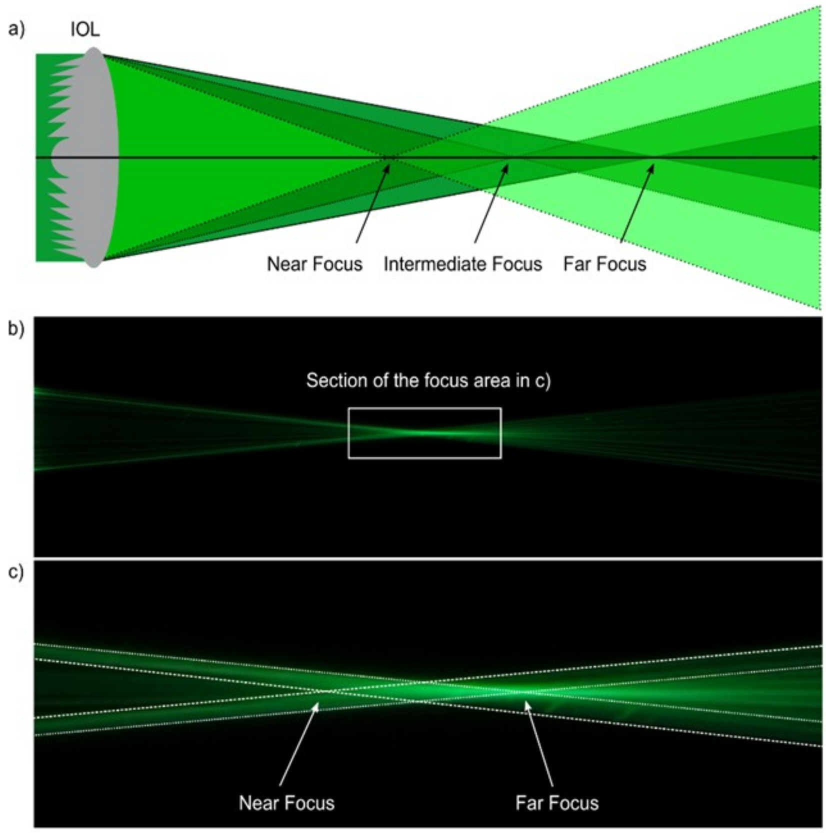

Figure 4: CSI of a diffractive trifocal IOL. a) Schematic representation of the light distribution of the near, intermediate and far focus, b) light distribution in a fluorescein bath recorded with a laterally positioned camera. The focal area is marked with a white rectangle, whereby the different foci cannot be delimited. c) shows the magnification of the cut-out area from b), the course of the rays is drawn in so that the near and far focus can be differentiated, but the intermediate focus is not visible separately. Reprinted with permission from Elsner et al. © Thieme Klinische Monatsblätter der Augenheilkunde [Pub. II].

3.2.2. Optical bench based light sheet method

Our custom-designed optical bench follows the ISO 11979-2:2024-12 standard [42] and is based on optical bench designs used by other research groups studying the imaging properties of IOLs [45,58,59]. Fig. 5 provides a schematic overview of the experimental setup used to capture the light distribution of the IOL.

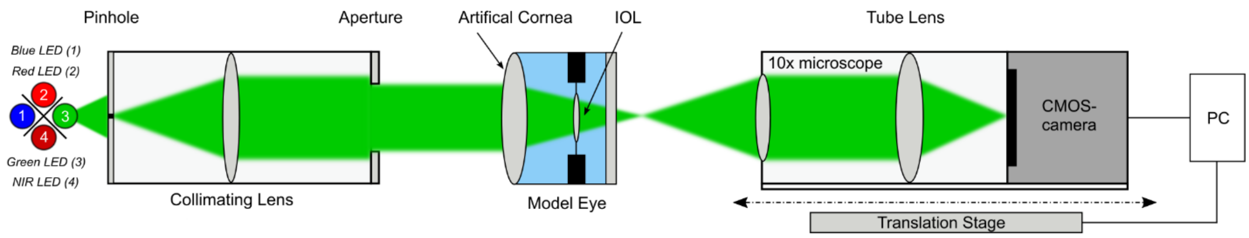

Figure 5: Schematic diagram of the optical bench for measuring the three-dimensional point spread function of intraocular lenses. The blue colored area within the model eye represents distilled water. To investigate the IOLs performance under different wavelengths four different light sources, a blue (1), red (2), green (3), and NIR (4) LED, were installed into the optical setup. Reprinted with permission from Elsner et al. © Translational Vision Science and Technology [Pub. III].

Unlike in [Pub. I and II] where only a green LED (λ_c = 530 nm, λ_{FWHM} = 47 nm) was used, the optical bench was equipped with three additional LEDs in [Pub. III]: a blue LED (λ_c = 463 nm, λ_{FWHM} = 23 nm), a red LED (λ_c = 628 nm, λ_{FWHM} = 15 nm) and a NIR LED (λ_c = 789 nm, λ_{FWHM} = 32 nm). The spectral characteristics of each LED were measured using a fiber optic spectrometer (AVASPEC-ULS4096CL-EVO, Avantes, Apeldoorn, The Netherlands). Fig. 6 gives an overview of the applied spectra, central wavelengths λ_c and the associated full width half maximum (FWHM).

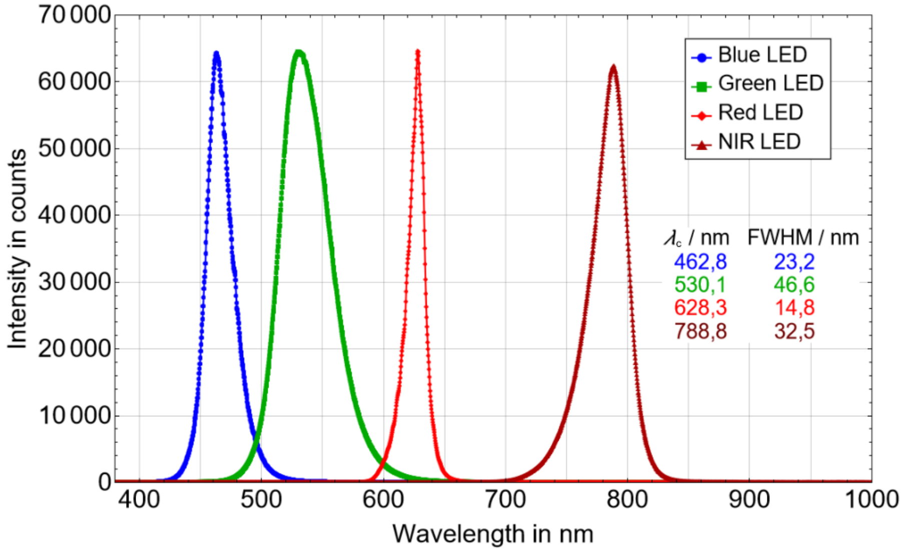

Figure 6: Overview of spectral bandwidths. For each light source the associated spectral bands are shown, specified by central wavelength λ_c and FWHM. The intensity of each spectrum is given in counts of the spectrometer (Source: Created by the author).

The light beam is first focused through a 10 µm pinhole (Thorlabs, Newton, NJ, USA) and subsequently collimated using an achromatic lens (f = 150 mm, AC254-150-A1, Thorlabs, Newton, NJ, USA). The diameter of the collimated beam can be adjusted using an aperture (SM1D12C, Thorlabs, Newton, NJ, USA). The model eye used in this setup was originally developed for the VirtIOL device (10Lens S.L.U., Terrassa, Spain), a see-through system designed for the simulated implantation of IOLs [60–62].

The model eye consists of a model cornea (MC 2), an IOL holder with the IOL under testing in water immersion, and a rear window. However, since one surface of the achromatic model cornea is in contact with water, it no longer retains its achromatic properties. As a result, it does not fully comply with the ANSI Z80.35:2018 [63] and ISO 11979-2:2024 [42] specifications. Nevertheless, this study focuses on the effects of monochromatic light on the tested IOL rather than the impact of polychromatic light. Therefore, the exact degree of chromatic aberration at each focal point is not relevant to the conclusions drawn in this work.

The illuminated area on the model cornea is adjusted using the iris diaphragm (aperture) positioned in the collimated beam right front of the model eye. The illuminated IOL diameter d_{IOL} was determined for a set of diameters d_A of the iris diaphragm using Ansys Zemax OpticStudio (ANSYS Inc. Headquarters, Canonsburg, PA 15317, USA). An almost linear relationship exists between the two diameters (see Table 1).

d_A in mm	2.5	3.0	3.5	4.0	4.5	5.0	5.5	6.0
d_{IOL} in mm	2.12	2.54	2.96	3.38	3.80	4.22	4.65	5.07

Table 1: Relationship between diameter of aperture d_A and diameter of illuminated IOL surface d_{IOL}. An almost linear relationship exists between the two diameters for the various pupil diameters that were set during the measurement series in this work.

A microscope objective (IC-10 MD Plan, NA = 0.25, Olympus, Shinjuku, Japan) captures the light distribution in the focal plane of the model eye. A 12-bit monochrome CMOS camera (UE-3880CP-M-GL, IDS Imaging, Obersulm, Germany) with a resolution of 3088 × 2076 pixels and a pixel size of 2.4 µm is mounted on a motorized translation stage (TRA25PPM actuator and NSC200 controller, Newport Corp., Irvine, CA, USA). The stage moves along the optical axis in increments of s_i = 7.63 µm, allowing for sequential imaging of the 2D-PSF at different axial positions. The camera and stage movements are controlled through a custom LabVIEW 2019 SP1 (National Instruments, Austin, TX, USA) script, enabling automated acquisition of multiple images at each position. The resulting image stacks represent a 3D-PSF of the investigated IOL, with measurements taken for apertures d_A ranging from 2.5 mm to 6.0 mm in 0.5 mm increments. For each axial position within the stack, six individual images of the 2D-PSF and the background signal were captured, allowing for precise reconstruction of the IOL's 3D light distribution.

3.3. Optical bench analysis

3.3.1. Image analysis algorithm for cross-sectional image determination

A proprietary algorithm, introduced in [Pub. I], was developed in Mathematica 12.0 (The Wolfram Centre, Oxfordshire, UK) and used for automated analysis of the captured 3D-PSFs within the optical bench setup. The algorithm was used for image analysis in [Pub. I-III] of this work. Since the diffractive MIOL under investigation and its resulting 3D-PSF are rotationally symmetric, an annulus integration method was employed. The general procedure is as follows: Each camera image is divided into a small central disk and surrounding concentric annuli of a specific width. The intensity within each ring is then summed, normalized by its area, and plotted as a function of the ring number starting from the image center. A Gaussian function is fitted to this distribution. These arrays are then combined to generate a CSI, which, along with its mirror image across the optical axis, forms the averaged cross-section of the 3D-PSF. This process is explained in detail in [Pub. I], along with a method to address the decrease in resolution caused by the annulus integration approach. Fig. 7 gives an overview of the general workflow.

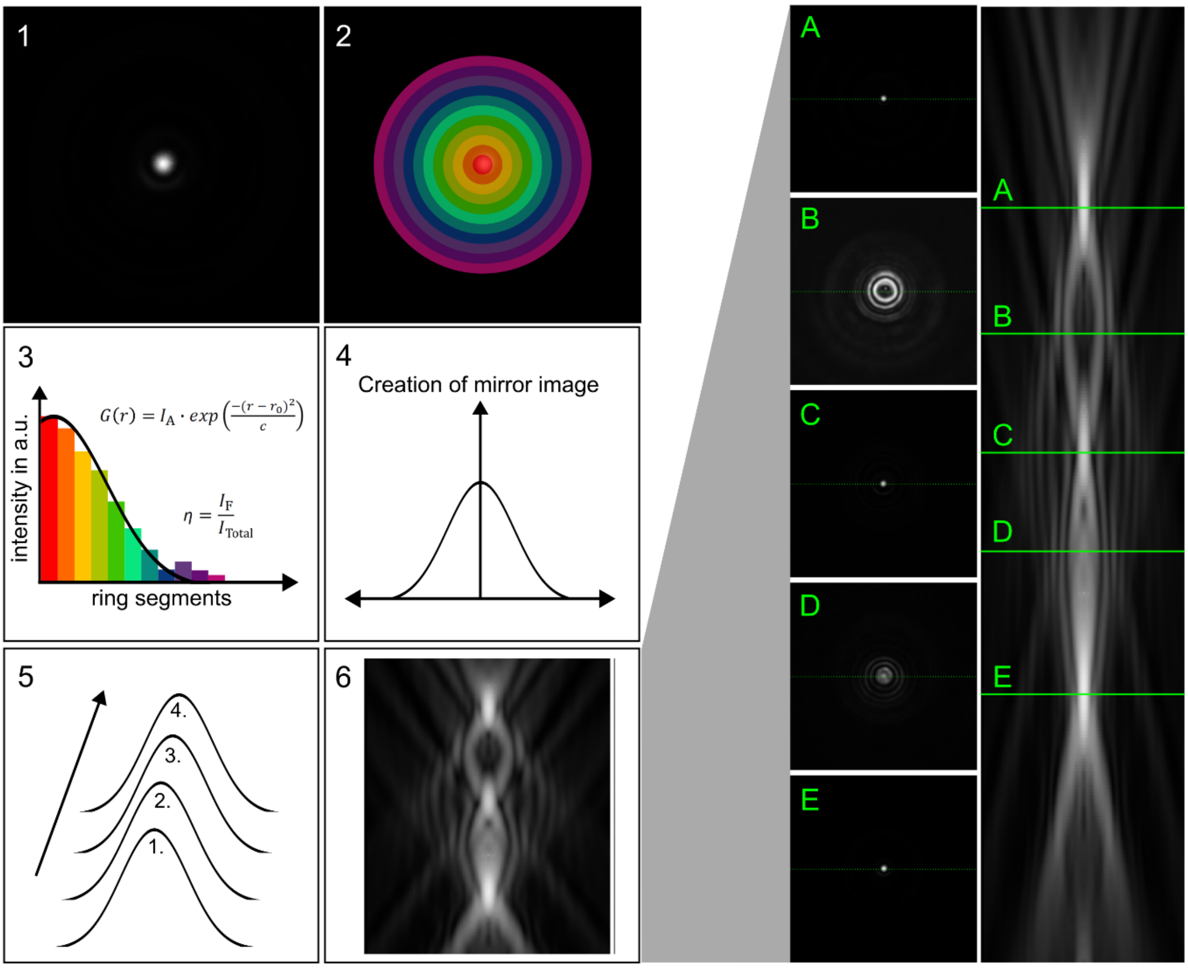

Figure 7: Overview diagram for the determination of intensity distributions and generation of rotationally averaged CSIs (RA-CSIs) using a dedicated image processing algorithm. For details, see text. On the left: 1) recording of a 2D-PSF; 2) determination of 2D-PSF pixels in annulus integration mask; 3) summed pixel intensities within each annulus area and Gaussian fit function *G*(r) over the distribution to calculate integral for energy efficiency *η*; 4) creation of mirror image on the optical axis based on the calculated intensities; 5) creation of RA-CSI by displaying 2D-PSF images of each travel position (e.g. 1.-4.) side by side; 6) final RA-CSI. On the right: The RA-CSI results from the fusion of 281 single 2D-PSF images and is shown in logarithmic scaling. There are five 2D-PSF images (A-E) in scaled, linear representation, taken at the position of the near focus (A), intermediate focus (C), far focus (E), and at two positions between the foci (B and D). r – radial distance from center, r_0 - center position of Gaussian curve, I_A – amplitude of Gaussian curve, c – scaling parameter for Gaussian width. I_F – intensity in focus, I_{Total} – total intensity over the sensor (Source: Created by the author).

For each axial position, the averaged 12-bit camera images and corresponding background images are imported and subtracted. Negative pixel values are replaced with zero values. To ensure proper alignment of each 2D-PSF image along the optical axis, each image is centered using the 2D-PSF image's midpoint in a pre-processing step. The annulus integration method uses an annuli mask, which divides the image into a central disk and surrounding concentric rings with a constant width of 4 pixels. The pixel locations for the disk and each annulus are classified and stored in an annuli mask file, calculated only once since the image resolution remains constant throughout the experiments. The total intensity within each ring is calculated by summing the pixel intensities, resulting in an intensity function based on the concentric rings. As the radius increases linearly from the center, the area of each annulus also increases linearly, causing a proportional increase in noise. This noise is corrected using a linear correction function. Further information about the image analysis algorithm is given in [Pub. I]. In the following, the rotationally averaged cross sectional images are referred to as RA-CSIs.

In the next steps the generation of through-focus curves and energy efficiencies is being discussed. Through-focus curves illustrate the intensity variation along the optical axis. The area used to calculate the through-focus intensity could be as small as one pixel. However, then the noise is greater compared to the averaged intensity of a small area around the focal point on the optical axis. To achieve the best signal-to-noise ratio a pixel area of 11 x11 pixel was chosen which is aligned to the optical axis. The intensity values within the pixel area of each 2D-PFS image are aligned side by side and then depicted as a through-focus curve.
In this work, we distinguish between two energy efficiency measures that may appear similar. Scalar diffraction efficiency, as commonly defined in scalar diffraction theory (e.g., Faklis and Morris [48]), treats light as a scalar wave and is expressed in arbitrary units (cf. Fig. 13). It essentially corresponds to the through-focus intensity curve, representing the distribution of on-axis energy. In contrast, the energy efficiency η is theoretically defined as the ratio of the light intensity at the focal point (I_{F}), which ideally corresponds to the intensity (I_{Airy}) of the focal points Airy disc, to the total incident light (I_{L}) (cf. Fig. 14). In practice, the total intensity of an image (I_{Total}) is the sum of (I_{L}) and the sensor noise (I_{Noise}), with defocused light excluded from the noise calculation, as described in Equation 1:

$$\eta = \frac{I_{\mathrm{F}}}{I_{\mathrm{L}} + I_{\mathrm{Noise}}} = \frac{I_{\mathrm{Airy}}}{I_{\mathrm{Total}}} \tag{1}$$

Unlike scalar diffraction efficiency, this metric also provides information on the proportion of light distributed into the surrounding halo pattern. However, it does not specify the halo intensity as it is an integrated value.

3.3.2. Camera specifications

Cameras are widely used in laboratory environments to detect light signals. Within the optical bench setup a 12-bit monochrome CMOS camera (UE-3880CP-M-GL, IDS Imaging, Obersulm, Germany) was installed [Pub. I and III]. For the fluorescein bath setup a Nikon D3 camera (Nikon Corp., Tokyo, Japan) with a 12.0-megapixel CMOS sensor was used [Pub. II]. In that context, the most important specifications are quantum efficiency (QE), bit depth, dynamic range, and signal-to-noise ratio (SNR).

QE of a camera sensor is defined as the ratio of the number of generated charge carriers (electrons or holes) to the number of incident photons on the sensor. It expresses how efficiently incoming photons are converted into an electrical signal and is typically given as a percentage. QE depends on the wavelength of the incident light, with certain wavelengths being detected more efficiently than others [64].

Bit depth refers to how many digital brightness levels a camera sensor can represent after analog-to-digital conversion and primarily affects the digital resolution of signal processing. For instance, in 8-bit images, signals can be represented with values ranging from 0 to 255, whereas in 12-bit images, the resolution increases to values between 0 and 4096 [65].

Dynamic range refers to the range of light intensities a sensor can capture from the darkest detectable signal to the brightest before saturation and is usually expressed in stops (exposure value) or as a ratio (e.g., 1:20,000) [65].

SNR is a measure of the signal strength relative to the noise and is a quality measure. A higher SNR implies either a stronger signal or lower noise and vice versa. SNR depends on both the signal strength and the noise level. In this work, the SNR is defined as described in Equation 2:

$$SNR = \frac{A_S - A_N}{\sigma_N} \qquad (2)$$

A_S and A_N, as the averaged amplitude of the captured signal and averaged amplitude of the noise, respectively, and σ_N denotes the variance of the noise [66,67].

3.3.3. Optics simulation

An optical simulation procedure was employed to validate the experimental results of green and near infrared light (NIR) measurements in [Pub. III]. This simulation was conducted using Ansys Zemax OpticStudio 2023 R2.00, enhanced with a user-defined surface model to accurately represent diffractive surface topographies and advanced mathematical methods for calculating diffraction efficiencies [47]. The simulation model consisted of an in-silico representation of the artificial model eye used in the laboratory experiments. It included the same components: a model cornea (achromatic doublet with an effective focal length of 40.0 mm), the immersion medium (pure water), the IOL prescription (AT LISA tri 839MP +25.0 D), and a glass (B270) exit window (see Fig. 8).

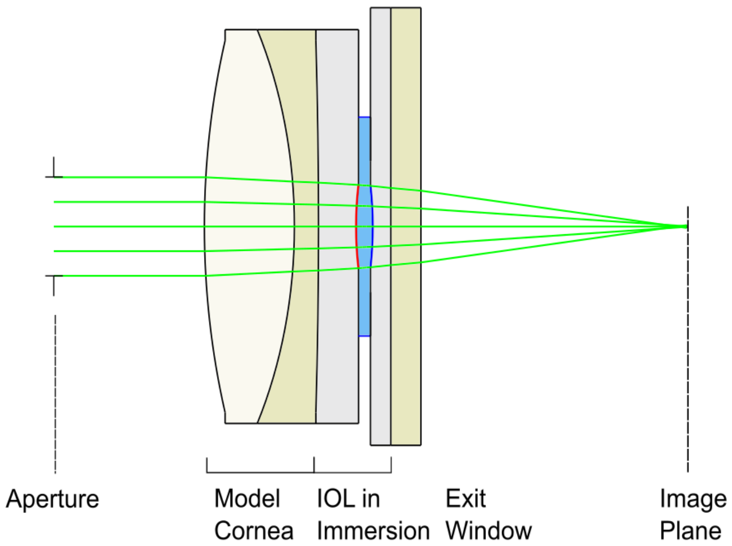

Figure 8: Optical layout of simulation environment. From left to right: The collimated light beam passes the aperture, continues through the model cornea and enters the IOL at the red surface (left side from the blue highlighted IOL immersed in distilled water, shown in gray) indicating a true topographical surface modeling of the diffractive profile. The rays then traverse an exit window before converging at the image plane on the right. Reprinted with permission from Elsner et al. © Translational Vision Science and Technology [Pub. III].

All optical materials were defined using dispersion formulas (Schott) to cover the entire polychromatic spectral range. Simulations were conducted using the same four spectral bands described in the experimental setup (cf. Fig. 6). The spectral intensity distribution for each band was resampled into 12 weighted wavelength data points to enable accurate polychromatic simulation.

The system aperture, placed in front of the artificial model, was set to diameters of 3.5 mm and 4.5 mm, corresponding to d_{IOL} = 2.96 mm and d_{IOL} = 3.80 mm on the IOL surface, to simulate the effects of photopic and scotopic pupil sizes on the imaging properties of the IOL. A through-focus diffraction efficiency analysis was performed by varying the detector distance relative to the exit window. In the simulation, an absolute x-axis was defined, with 0 mm corresponding to the back of the rear window of the model eye. In contrast, the experimental measurement data was represented on a relative x-axis. To enable side-by-side comparison, the relative x-axis of the experimental data was shifted so that the far focus overlapped with the green spectral band at d_{IOL} = 2.96 mm (cf. Fig. 13).

4. Results

4.1. Comparison of fluorescein bath and optical bench light sheet methods

To compare conventional approaches as the fluorescein bath method and our RA-CSI method, the cross-sectional images in Fig. 9 show the observed light distributions of the AT LISA Tri 839MP using a fluorescein bath (Fig. 9 (a)) and the optical bench with the new image processing algorithm (Fig. 9 (b)) at a d_{IOL} of approximately 5 mm. The intensities are presented on a linear scale. A comparison of the images reveals that while ray trajectories are discernible with the fluorescein bath light sheet method, foci are limited or indistinguishable. The detail magnification, scaled in the µm range, highlights the limitations of the fluorescein bath light sheet setup but does not imply a general restriction of this methodology. In contrast, the new method (Fig. 9 (b)) enables a clearer localization of multiple foci. The near focus is observed at approximately 0.4 mm, the intermediate focus at 0.9 mm, and the far focus at 1.5 mm axial positions. For more details see [Pub. II].

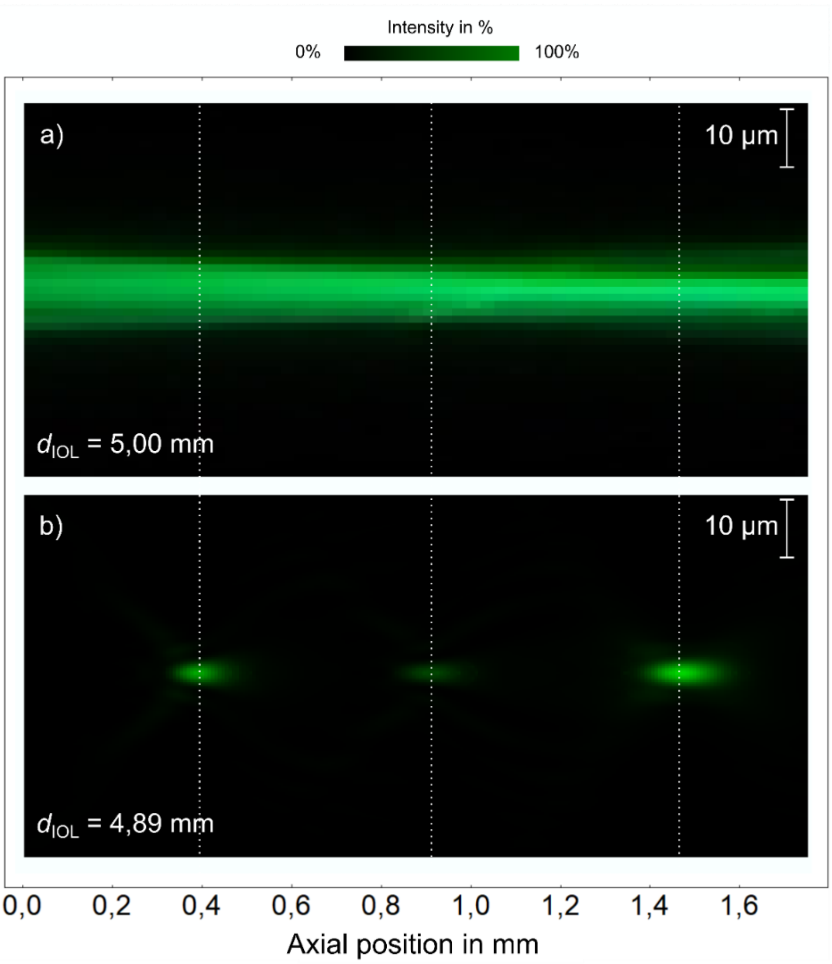

Figure 9: Comparison between fluorescein bath CSI and RA - CSI. Comparison of the cross-sectional images of the AT LISA tri 839MP (+ 22.5 D) recorded using a) a fluorescein bath and b) an optical bench (pupil diameter $d_{IOL} \approx 5.00$ mm) in a linear intensity scaling. a) shows the light distribution recorded with a lateral camera in a fluorescein bath illuminated using a laser. The individual foci cannot be delimited. b) shows the light distribution of the same IOL illuminated by a green LED, calculated from the 3D-PSF values by means of an annulus integration method. Here, all foci are well distinguishable. Reprinted with permission from Elsner et al. © Thieme Klinische Monatsblätter der Augenheilkunde [Pub. II].

4.2. Influence of light sheet thickness on cross-sectional images

CSIs of the 3D-PSFs of IOLs are used to analyze their image-forming properties. These images are typically acquired using light sheet-based techniques. However, the non-negligible thickness of the light sheets imposes limitations on the image quality of the resulting cross sections. To analyze the influence of light sheet thickness, simulated CSIs were extracted by accumulating intensity data from narrow volumes of the 3D-PSF with simulated light sheet thicknesses of 15 (a), 150 (b), and 1500 (c) pixels from the averaged and background corrected images of the image stack. These specific pixel ranges were chosen to align with prior research and optical configurations:

- (a): Chosen to examine fine wave propagation intensities within a narrow volume along the optical axis.
- (b): Corresponding to the light sheet thicknesses used in fluorescein bath studies by Reiß et al. (0.35 mm) [43] and Eppig et al. (0.3 mm) [44], which translate to an average sensor width of approximately 150 pixels (≈ 159 px and ≈ 136 px, respectively) for the optical bench camera setup and the tested MIOL.
- (c): Aligning with the approach of Peteclczyc et al. [45], who used a broader light sheet thickness to calculate through-focus PSFs.

These simulated light sheet thicknesses translate to the experimental light sheet thicknesses (t) of 4.3 µm (a), 43 µm (b), and 430 µm (c), respectively, on the sensor. Here, an image stack consisting of six images and six background images per axial position in a 12-bit format were captured using the optical bench for an aperture diameter d_A = 3 mm. This aperture size complies with ISO standard 11979-2:2024 [42], reflecting the reduced pupil diameter typical of cataract patients under photopic conditions [68,69]. Using the initial steps of the new algorithm, the background-corrected, centered 3D-PSFs were determined. Fig. 10 presents simulated CSIs with intensity values scaled linearly (left) and logarithmically (right) due to the linear response of the camera sensor and the logarithmic sensitivity of human eye [33]. The lateral image areas of the CSIs were trimmed and stretched to three times their original width perpendicular to the optical axis to improve the visibility of light rays. Each CSI was scaled to its maximum intensity.

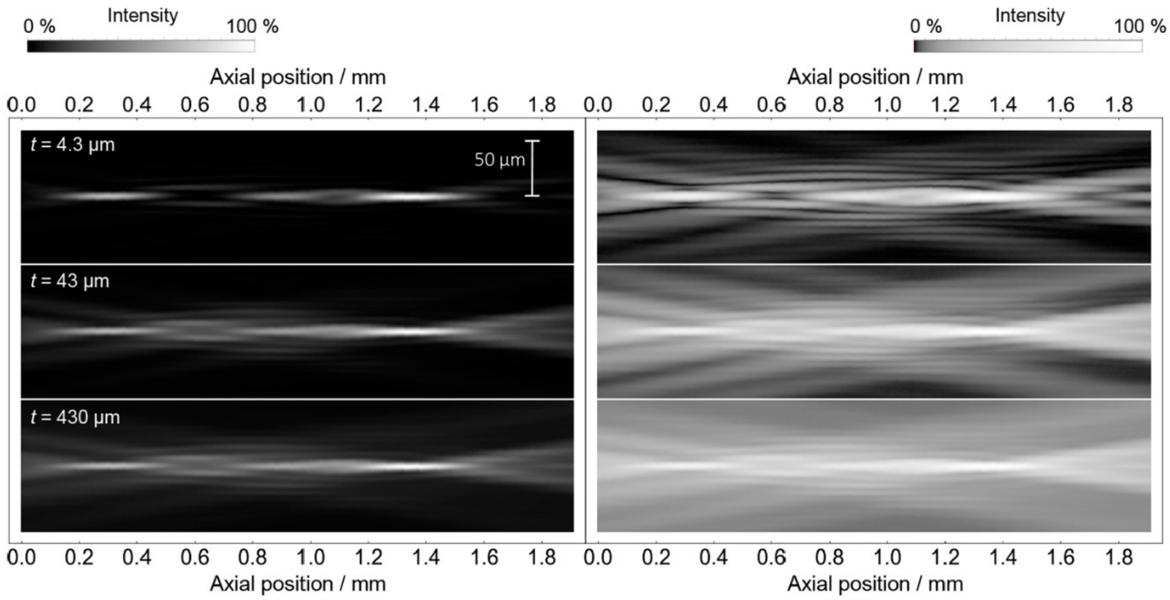

Figure 10: Simulated CSIs of AT LISA Tri 839MP (+22.5 D). The CSIs are shown with intensity-dependent gray values for varying light sheet widths *t*. The left column displays linearly scaled intensities, and the right column shows logarithmically scaled intensities for an illuminated IOL diameter of d_A = 3 mm. The near focus appears at an axial position of approximately 0.3 mm, the intermediate focus at about 0.9 mm, and the far focus at roughly 1.35 mm. Reprinted with permission from © Optical Society of America [Pub. I].

The simulated CSI for *t* = 4.3 µm light sheet thickness reveals three well-defined focal points, with minimal overlap and visible ray extensions in the off-axis areas along the optical axis (see Fig. 10, top left). As the light sheet thickness increases, the separation between intermediate and far focus smears due to contrast loss, and ray extensions become more pronounced (see Fig. 10, middle and bottom left). These additional structures near the optical axis, particularly around the intermediate focus, are identified as halos caused by out-of-focus energy from other focal points [70]. These halos reduce visual acuity at specific distances [71].

Logarithmic scaling highlights fine structures across the image area for *t* = 4.3 µm, e.g. transitions between intermediate and far focus. An additional focal point is visible at 1.9 mm axial distance, likely corresponding to a negative diffraction order [72] (see Fig. 10, top right). The alternating bright and dark stripes appearing in the off-axis regions are most likely due to interference effects between light beams from different MIOL zones.

Increasing the light sheet thickness (*t*) results in overlapping intensities, elevated background signals from outer regions, and diminished fine structure contrast for both linear and logarithmic scaling (see Fig. 10, bottom left and right).

For consistency with previous studies using fluorescein baths [43,44], a light sheet thickness of *t* = 43 µm (b) was used for simulated CSI calculations in subsequent analyses.

4.3. Comparison of simulated CSIs to rotationally averaged CSIs

Several MIOLs have a rotationally symmetric design, a property that we take advantage of to enhance image quality and increase the SNR. The new algorithm was applied to the acquired 3D-PSFs to calculate RA-CSIs and was then compared with simulated CSIs regarding image quality, SNR, and the visibility of fine features. For the aperture configuration d_A= 3 mm, the influence of background correction and averaging was analyzed as follows:

Fig. 11 (a and e): Only one single 2D-PSF image per axial position was used.

Fig. 11 (b and f): Only the first background image per axial position was subtracted.

Fig. 11 (c and g): All six 2D-PSF and background images per axial position were averaged after subtraction.

Fig. 11 (d and h): The averaged and background-corrected images were evaluated with the new algorithm (RA-CSIs).

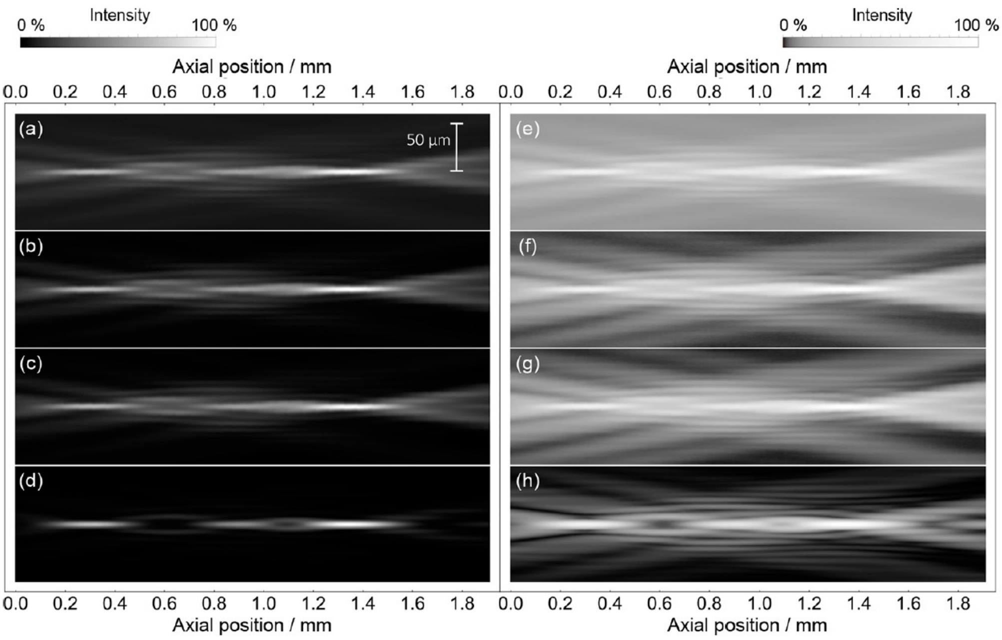

Figure 11: Comparison of simulated and RA-CSIs of AT LISA Tri 839MP (+22.5 D). The left column shows linearly scaled intensities, while the right column displays logarithmically scaled intensities. CSIs were acquired from different image stacks with an aperture of d_A =3 mm and are shown in panels (a) - (h). Panels (a) and (e) display single captures at each axial position without background-signal correction, and panels (b) and (f) show the same data with single background-signal correction. Panels (c) and (g) illustrate six-fold averaged, background-corrected data, all computed using the light sheet thickness (t = 43 µm). In contrast, panels (d) and (h) present averaged, background-corrected data calculated via the new algorithm (RA-CSIs). Each CSI is normalized to the maximum gray value. The near, intermediate, and far focus appear at approximately 0.3 mm, 0.9 mm, and 1.35 mm along the axial direction, respectively. Reprinted with permission from Sievers et al. © Optical Society of America [Pub. I].

The simulated CSIs were calculated using the light sheet thickness t = 43 µm and compared to the new algorithm. CSIs in Fig. 11 (a) - (d) are linearly scaled, while those in Fig. 11 (e) - (h) are logarithmically scaled. In all CSIs, the near focus is located at ~0.3 mm, the intermediate focus at ~0.9 mm, and the far focus at ~1.35 mm. The near and intermediate foci are well separated, with a depth-of-focus behavior in-between, most likely in the interplay with spherical aberrations. Halos are also evident at the focal points, particularly around the intermediate focus.

The comparison of Fig. 11 (a) - (c) shows no apparent differences in shape, contrast, or intensity under linear scaling. However, in the defocus zone between intermediate and far focus, separation of the focal points remains unclear. Under logarithmic scaling (Fig. 11 (e) - (g)), the impact of background correction and averaging becomes evident. Background correction eliminates a gray overlay in Fig. 11 (f), while averaging enhances the visibility of fine details, as seen in the images off-axis areas (Fig. 11 (g)).

The RA-CSIs produced by the new algorithm (see Fig. 11 (d)) separate the three focal points in linear scaling, with minimal intensity in defocus regions. Although interference effects at the outer focal areas are inevitably visible, they are less pronounced than in the simulated CSIs. Fine features in the off-axis areas, such as those at ~0.8 mm and near the lateral edges, are also reduced. In the logarithmic representation (see Fig. 11 (h)), the new method distinctly reveals the three focal points and associated ray patterns. Additionally, a fourth focal point at ~1.9 mm is visible but clinically irrelevant, as it lies behind the retina.

The SNR was calculated for the focal points using Eq. 2, with values derived from intensity response along the optical axis and 2D-PSF images associated with each focal point, respectively (see Table 1 [Pub. I]). Background correction improved the SNR by a factor of ~1.3 for the CSI. Averaging of the 2D-PSF images increased the SNR by a factor of ~2.49 for the CSI. Both background correction and image averaging increased the SNR by a factor of ~3.24. However, the new algorithm increased SNR values by approximately two orders of magnitude for the RA-CSIs.

Both Fig. 11 and the SNR values highlight the improvements in image quality and fine feature visibility achieved by the new algorithm. To further explore its capabilities, wavelength dependent though-focus-curves and energy efficiencies of the investigated trifocal diffractive IOL are presented in the following chapter.

4.4. Wavelength dependence of IOL performance

The through-focus curves for the AT Lisa Tri 839MP (+25.0 D) under green light (shown in green) and NIR light (shown in dark red) across d_{IOL} ranging from 2.12 mm to 4.22 mm are presented in Fig. 12. Each diagram compares two d_{IOL}, with dashed lines representing the smaller d_{IOL} and solid lines the larger. Under green light, the through-focus curve for $d_{IOL} \approx 2.12$ mm (left diagram, dashed green line) displays two extended intensity distributions, indicating bifocal behavior with EDOF characteristics (see Fig. 12, top). When d_{IOL} increases to ~2.5 mm (solid line), the IOL exhibits trifocal behavior. In Fig. 12 (bottom), three distinct foci are visible for both wavelengths. As d_{IOL} increases the near and far foci shift to greater axial positions, while the intermediate focus remains largely independent of pupil size.

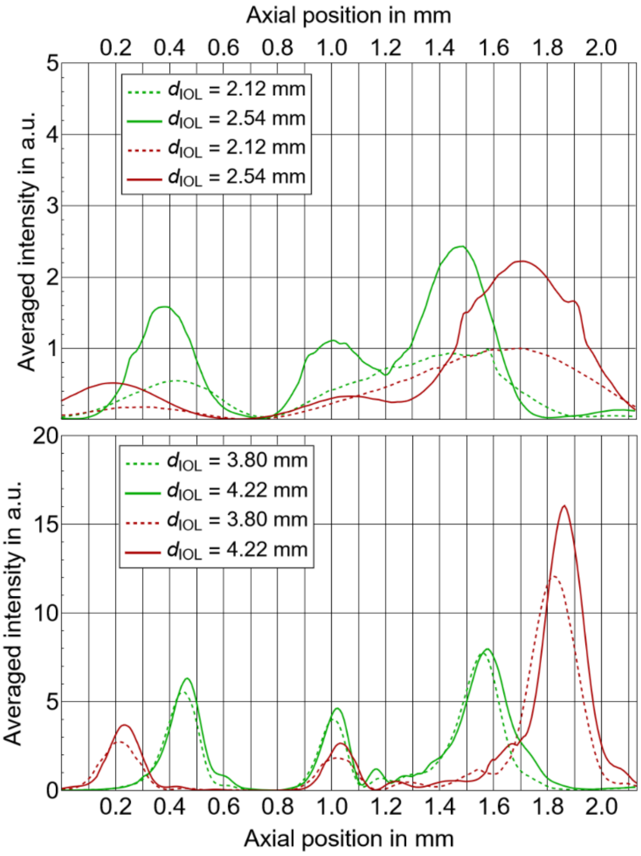

Figure 12: Overview of the through-focus curves (TFC) measured under 530 nm (green lines) and 789 nm (NIR, dark red lines) illumination for a AT LISA tri 839MP (+25.0 D) in a model eye (using MC 2) across four d_{IOL}. The figure shows that under NIR illumination more intensity gets directed into the far focus compared to green light, with less intensity being distributed into the near and intermediate focus. A wavelength dependent axial shift of the foci can be noticed, with a greater shift for greater wavelengths. The overall intensity increases with growing d_{IOL}. Top: TFC data for d_{IOL} of 2.12 & 2.54 mm. For a 2.12 mm, the IOL demonstrates a bifocal character under both green and NIR illumination (intensity scaled from 0 to 5 for better visibility of graphs). Bottom: TFC data for d_{IOL} 3.80 & 4.22 mm. (Source: Created by the author).

The greatest axial shift with increasing pupil size occurs in the far focus under NIR light, followed by the far focus under green light. The distance between near and far foci ($D_{NEAR\text{-}FAR}$) remains stable for green light, but increases under NIR light for increasing d_{IOL}. This suggests a stronger dependence on pupil size under NIR light compared to green light. Switching from green to NIR light increases $D_{NEAR\text{-}FAR}$ from ~1.10 mm to ~1.60 mm (see Fig. 12). Interestingly, for the same MIOL, more intensity gets directed into the far focus under NIR illumination compared to green light, while the near and intermediate loose in intensity (Fig. 12, bottom). For d_{IOL} = 2.12 mm, the IOL shows a smeared overlap of near and intermediate foci, reflecting bifocal behavior. For larger d_{IOL}, the IOL exhibits trifocal behavior across all tested wavelengths. More details about the specific shifts in focus position and intensity are given in [Pub. III]. Optical simulations using blue, green, red and NIR light confirmed the experimental results (see Fig. 13).

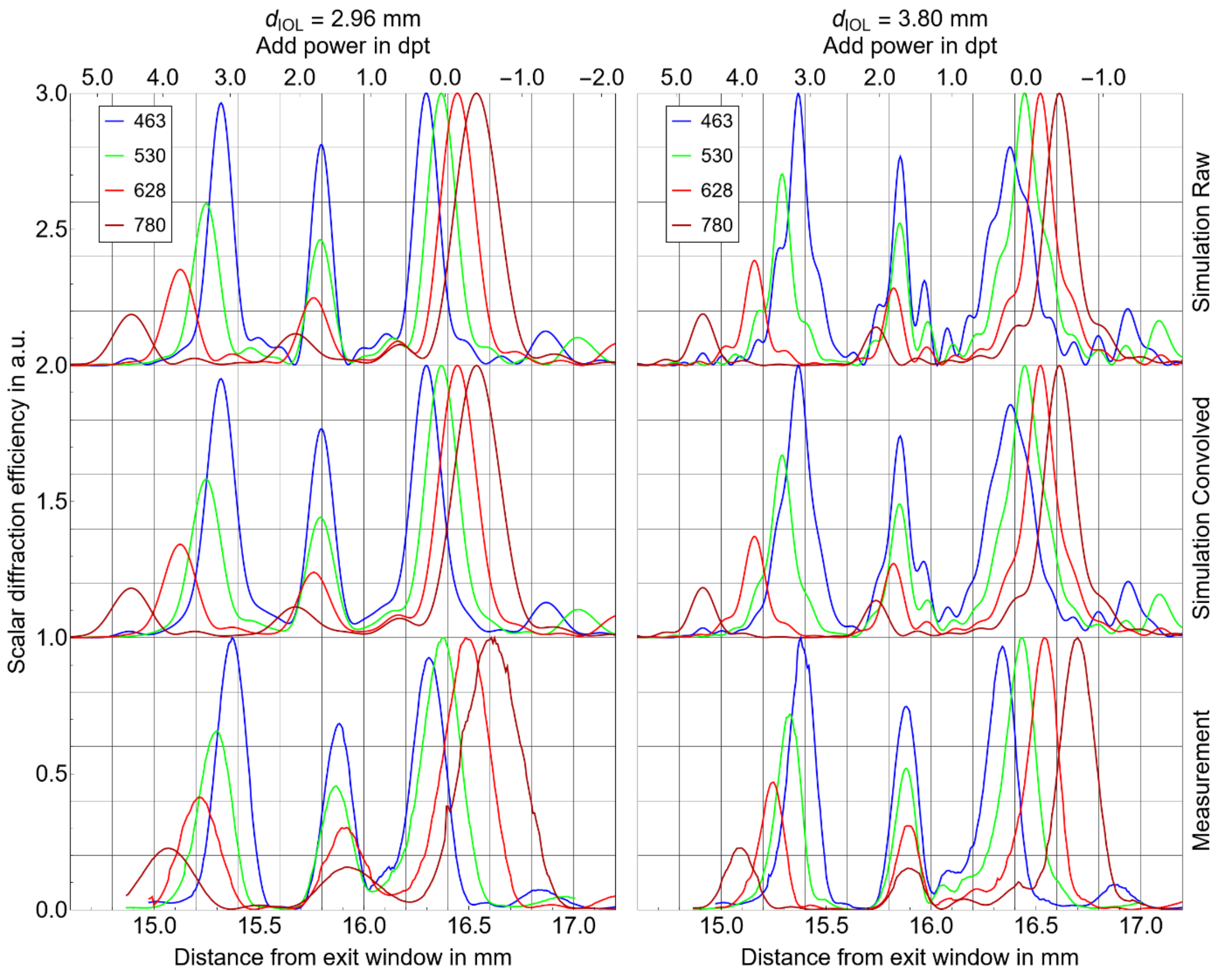

Figure 13: Focal wavelength dependency of AT LISA tri 839MP (+25.0 D). This figure shows the through-focus curves for four different wavelengths (463 nm – blue lines, 530 nm - green lines, 628 nm – red lines and 789 nm – purple lines) and two d_{IOL}, (A) 2.96 mm and (B) 3.80 mm. For clarity, the simulated curves (top) are shifted by +2, while in the middle, they are convolved with a 10 µm Gaussian filter, to account for the microscope's depth of field, and shifted by +1 to better match the measurement data (bottom). With increasing wavelength more light gets directed into the far focus and the distance between near and far focus increases. Reprinted with permission from Elsner et al. © Translational Vision Science and Technology [Pub. III].

The top row shows simulation data, while the bottom row presents measurement data. Results for smaller (d_{IOL} = 2.96 mm, d_A = 3,5 mm) and larger (d_{IOL} = 3.80 mm, d_A = 4,5 mm) pupil sizes are displayed on the left and right, respectively, with intensity curves normalized. The simulation data, convolved with a Gaussian filter (10 µm width) to account for the microscope's depth of field, aligns well with the measurement data. With increasing wavelength more light gets directed into the far focus (see Fig. 13, far focus position ≈16.5 mm/ +0 D), with the near and intermediate foci exhibiting a decrease in scalar diffraction efficiency in simulation (middle row) and measurement data (bottom row).

With increasing wavelength, the distance between near and far foci ($D_{NEAR\text{-}FAR}$) grows, shifting the near focus to smaller axial positions and the far focus to larger ones.

Energy efficiency (η) quantifies the proportion of light contributing to each focus. Fig. 14 compares energy efficiency as a function of pupil size for green light (left) and NIR light (right), highlighting differences between design wavelengths (green) and NIR light. While the far-focus through-focus intensity increases with pupil diameter (see Fig. 12), the energy efficiency decreases with increasing pupil size due to losses in halos and higher-order aberrations.

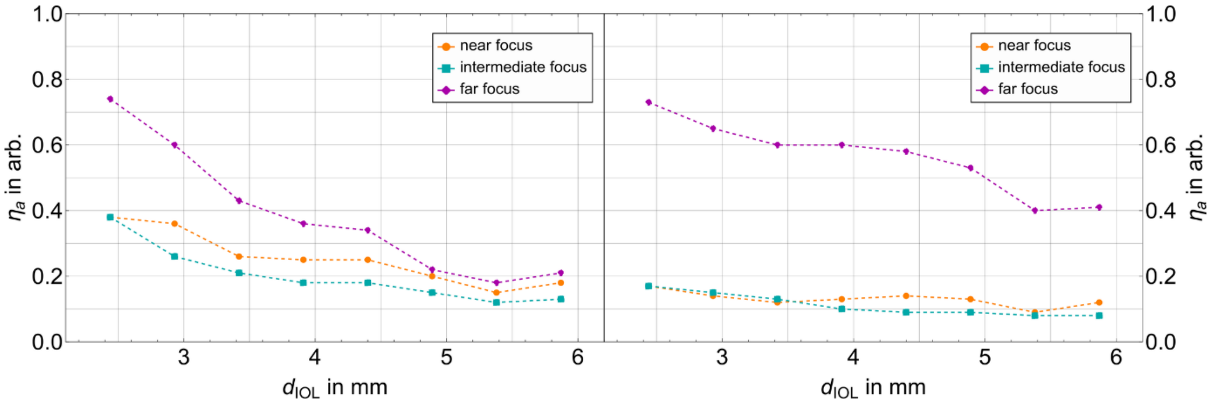

Figure 14: Energy efficiencies of AT Lisa Tri 839MP (+25.0 D). These plots illustrate how the AT LISA tri 839MP, Carl Zeiss Meditec AG, Germany distributes energy to its near (●), intermediate (■), and far (♦) foci across different pupil sizes. The left panel shows results under 530 nm illumination (green light), and the right panel under 789 nm (NIR) illumination. Under NIR light, much more energy is shifted to the far focus, with significantly less directed to the near and intermediate foci - resulting in a predominantly monofocal behavior at NIR wavelengths. Reprinted with permission from Elsner et al. © Translational Vision Science and Technology [Pub. III].

Under green light, the far focus is nearly twice as efficient as the near and intermediate foci for small pupils but converges at larger pupil sizes. Under NIR light, however, the far focus remains more than four times as efficient as the other foci, even for larger pupils. Comparing both wavelengths, energy efficiency for the near and intermediate foci decreases from ~ 25 % (near) and ~ 18 % (intermediate) under green light to ~ 14 % (near) and ~ 9 % (intermediate) under NIR light at a d_A = 4.5 mm. This aperture was chosen for comparability of previous studies on wavelength dependence of the investigated IOL by Vega et al. [55] (see Table 3 [Pub.III]).

Our findings demonstrate that under NIR light, significantly more energy is directed to the far focus compared to green light, where the energy distribution is more balanced. Consequently, while this specific diffractive IOL behaves as trifocal under visible light, it transitions to nearly monofocal under NIR light. This behavior should be considered in the clinical application of NIR-based devices (cf. Table 2) to evaluate diffractive IOLs.

5. Discussion

The evaluation of multifocal IOLs presents several challenges, particularly in accurately assessing their optical and perceptual performance. This synopsis highlights key findings from three distinct studies, presenting a unified perspective on advanced methodologies, wavelength-dependent behaviors, and perceptual phenomena associated with MIOLs.

Traditional light sheet-based methods, including those in optical benches [45] or those using fluorescein/ouzo/milk baths [43,44], have been integral in generating CSIs to evaluate MIOLs. However, the inherent limitations of light sheet thickness constrain image quality, obscuring fine features such as halos and higher diffraction orders. Fluorescence intensity loss along the optical axis, scattering artifacts from particles in the fluorescein bath are factors that can lead to inaccurate representations of IOL optics.

This research shows that image quality in optical bench analysis depends on light sheet thickness with thinner sheets giving better results. Artifacts and off-axis features are more prominent due to background signal and image averaging over the illuminated light sheet. The proprietary image analysis algorithm improves image quality by exploiting the rotational symmetry of IOLs, see [Pub. I]. It generates rotationally averaged cross-sectional images (RA-CSIs) with higher SNR and better visibility of fine features, such as higher diffraction orders. This way, the MIOL's different focal points can be well distinguished (see Fig. 9 and 11). Further, an additional focus could be detected (see Fig. 10), likely corresponding to higher diffraction orders due to the diffractive nature of the investigated MIOL [37,72]. Contrast loss in the fluorescein based or simulated CSI-techniques often renders them undetectable.

Comparative analyses reveal that this new method provides superior fine-structure visibility, accurately delineating focal points and diffraction orders, see [Pub. II]. The new method also identified additional depth-of-focus behavior, most likely in the interplay with spherical aberrations, between intermediate and far focus regions for certain pupil sizes of the investigated IOL (see Fig. 11).

Moreover, this research shows that the optical performance of the investigated trifocal diffractive MIOLs is highly wavelength-dependent, a characteristic often overlooked in clinical assessments utilizing near-infrared (NIR) light, as previously shown by Charman [52], Campbell [53] and Vega et al. [55,73]. Using the AT LISA tri 839MP as a model, studies revealed that NIR light leads to a substantial reduction in the intensity of near and intermediate foci, rendering trifocal lenses effectively monofocal (see Fig. 12 and 13)**.** This is attributed to the wavelength-dependent scaling of diffraction efficiency and add power, as studies by Fiala et al. [47] and Faklis et. al [48] and experimental results confirm [55]. A metric for the performance analysis of MIOLs is the energy efficiency η mentioned in Chapter 3.3.1., as it considers scattering, aberration, and out-of-focus images for each focus. Vega et al. [55]

analyzed the same diffractive trifocal IOL among others, employing the so called “light-in-the-bucket metric” to calculate energy efficiencies. In contrast, our method uses a Gaussian fitting function (see Fig. 7). Notably, the relationship between energy efficiency ratios derived from experimental and simulation data is consistent across both setups but the magnitudes differ (cf. Table 3 [Pub. III]). NIR-based vision assessment methods, including wavefront sensors and double-pass systems, exacerbate these inaccuracies due to the redistribution of light energy into the zeroth diffraction order. Consequently, clinical evaluations relying on NIR light risk misinterpreting the multifocal capabilities of diffractive MIOLs.

NIR using device	**Company**	**Wavelength in nm**	**Found publications**	**Citations**
Wavefront aberrometers				
iTrace	Tracey Technologies, USA	785	6 [74–79]	132
OPD Scan III	Nidek Inc., USA	780	3 [80–82]	131
HD Alcon LADARWave	Alcon Inc., USA	820	3 [76,83,84]	219
KR-1W/KR 1-W	Topcon Corporation, Japan	820 - 840	1 [85]	62
Osiris	CSO S.r.l., Italy	850	1 [86]	56
WASCA Analyzer	Carl Zeiss Meditec AG, Germany	850	0	0
ZyWave	Bausch & Lomb Inc., USA	780	0	0
Wavescan Aberrometer	Abbot Medical Optics Inc., USA	785	0	0
iDesign	Johnson & Johnson Vision Inc., USA	535 - 940	0	0
Double pass systems				
Optical Quality Analysis System	QQVision Ltd., China and Halma plc, UK	780	8 [87–94]	347
HD Analyzer	Halma plc, UK	780	1 [95]	11
Total sum			**23**	**958**

Table 2. Overview of commonly used commercial wavefront aberrometers and double pass systems that use NIR light. A Clarivate “Web of Science” search was used to obtain an estimated number of publications analyzing DMIOLs with devices using NIR light. For example, the search with the search parameters “iTrace AND diffractive IOL” yielded six results. The table comprises the device names, companies, used wavelengths and the number of citations found associated with studies on DMIOLs listed for each device. Please note that the references given do not claim to be complete (requested October 2025).

Table 2 gives an overview of NIR-based devices being used for studies on diffractive MIOLs underlining the need for an updated practice in the ophthalmologic community considering the high number of citations associated with this topic.

Visible light, preferably at least three design wavelength from the visible spectrum, is recommended for accurate assessments, despite the challenges of low retinal reflectance [50]. Furthermore, the results from [Pub. III] underline the necessity of using precise surface topography data for simulations to achieve reliable predictions of MIOL performance, since this data differs between different publications [56,96,97]. Developing advanced visible-light-based diagnostic tools to replace NIR-based systems would address current methodological flaws and provide more accurate evaluations of diffractive MIOLs. These tools should aim to balance low light intensity to reduce glare while ensuring adequate retinal reflectance for reliable measurements.

The new proprietary algorithm currently focuses on rotationally symmetric MIOLs to create RA-CSIs. Extending this approach to accommodate asymmetric lens designs, such as those with refractive-diffractive combinations, would broaden its applicability and enhance its utility in diverse clinical scenarios. While the new image-processing algorithm marks a significant advancement, future research should explore more efficient programming languages, parallel processing with graphics cards (CUDA, OpenCL), and alternative interpolation techniques to reduce processing time while maintaining accuracy. Another limitation of this optical bench setup is the delicate and time-consuming alignment of the model eye holding the IOL within the optical path. For the generation of rotationally averaged CSIs, the IOL must be precisely centered and aligned with the optical axis. Even minor tilt or decentration can lead to an uneven light distribution within the annular integration mask and, consequently, to a loss of information in the RA-CSI. Automating the alignment process of the IOL within the optical setup would significantly accelerate and stabilize the measurement procedure.

Even though optical benches have become the standard for preclinical testing, enabling the analysis of key metrics such as MTFs, PSFs and through-focus energy distributions to verify an IOLs' performance against manufacturers' claims, the lack of standardized definitions for metrics such as energy efficiency in optical bench measurements complicates comparisons across studies. Establishing a universal benchmark would ensure consistency and reliability in MIOL evaluations.

Moreover, the objective *in vitro* evaluation of IOLs using fluorescein baths or optical bench setups does not necessarily reflect patients' *in vivo* perception of light phenomena and dysphotopsias, owing to the complex nature of retinal image processing. However, as mentioned in the introduction, approaches such as clinical questionnaires and interactive simulators evaluating dysphotopsias are likewise constrained by the inherent subjectivity of human perception, while not being fully able to assess the IOLs optical properties.

Therefore, there is a need for an approach that enables the comparison of objective and subjective IOL performance within a unified, camera-based setup for assessing the degree of halos and glare, associated with different multifocal IOL designs, while accounting for the above mentioned metrics, to provide patients the best possible visual outcome.

6. Conclusion

The aim of this work was to address and explore challenges in the evaluation of intraocular lenses by employing an advanced optical bench setup and a novel image processing algorithm, and by comparing these to traditional techniques to identify methodological shortcomings in current evaluation techniques. In doing so, the work bridges the gap between experimental research and clinical application, offering a more comprehensive assessment of MIOLs.

In **[Pub. I]** an image-processing algorithm exploiting rotational symmetry of IOLs was introduced, significantly improving the quality of CSIs obtained from the 3D-PSFs of the investigated trifocal IOL. By achieving an increase in the SNR of approximately two orders of magnitude, the algorithm enabled a more detailed visualization of fine structural features in the rotationally averaged cross-sectional images.

[Pub. II] compared the traditional fluorescein-bath method with the algorithm derived RA-CSIs, showing an enhanced fine structure visibility, and accurate delineation of focus positions with the new method. These improvements provide deeper insights into the optical properties of rotationally symmetric IOLs, laying a foundation for more reliable analyses.

The findings in **[Pub. III]** underscore the limitations of near-infrared (NIR) light in evaluating diffractive MIOLs. NIR illumination distorts diffraction efficiencies, causing near and intermediate foci to lose intensity and rendering the investigated trifocal IOL functionally monofocal. This study emphasizes the necessity of using visible light, preferably at least three design wavelength from the visible spectrum, for accurate in vitro and in vivo evaluations of MIOLs, while also advocating for precise surface topography data to improve optical simulations. In this context, conclusions regarding the postoperative *in vivo* imaging performance of diffractive MIOLs reported in previously published studies cannot be regarded as reliable.

This research advocates for updated clinical practices and standards that align with the true optical properties of MIOLs. By refining these approaches, clinicians and researchers can better understand the optical performance and patient outcomes of these complex lenses.

7. Future Perspectives

With the help of simulated implantation techniques and a unified camera-based setup, going beyond the scale of optical benches, the ultimate goal is to bridge the gap between subjective and objective analysis of dsyphotopsias associated with IOLs. These photic phenomena, including halos and glare, significantly affect the visual comfort of MIOL users, in particular DMIOLs, especially under low-light conditions, e.g. while driving at night.

Using high dynamic range (HDR) image creation, spanning at least five orders of magnitude, future works focus directly on the comparison of the generated HDR intensity profiles in comparison to subjectively perceived halo sizes. A central question in comparing different light sources is how to adjust them to the same perceived intensity, considering their different characteristics in terms of intensity and spectrum. Since camera sensors detect light in a linear manner [98], whereas the human retina responds logarithmically [33] and exhibits local neuroadaptation effects, it remains, to this date, impossible to accurately infer human visual perception from objective camera-based data. The basic idea of the setup is to adjust the forward currents of two different light sources so that they appear of the same brightness for the human eye. In this context, the study examines the imaging properties of three different IOL designs: a monofocal IOL as control, a diffractive trifocal IOL, and a diffractive EDOF IOL under various light sources, focusing on how wavelength or spectral bandwidth might influence halo patterns and sizes. As part of future works, the aim is to develop and implement a novel method for halo analysis below the intensity threshold of 10^{-4} (ISO standard 11979-2:2024) based on the hypothesis that strong oscillations in the PSF, as observed in Fig. 10 and 11 in the off-axis image areas, lead to more intense and stronger perceived halo patterns. The new algorithm is supposed to identify the width of the PSF containing such oscillations.

An open question remains regarding how halos of diffractive IOLs depend on wavelength and spectral bandwidth, and how narrow-band light sources such as LEDs may generate more pronounced halo rings, influenced by the distribution of optical energy among diffraction orders and by interference effects at the lens phase steps. It also remains not fully understood how halo perception depends to neuroadaptational effects in the human retina rising the need for more detailed psychophysiological testing. Using simulated implantation devices like the VirtIOL (10 Lens S.L.U., Terrassa, Spain) or VisuEye system (Carl Zeiss Meditec AG, Berlin, Germany) and a camera-based setup for quantitative analysis, this work tries to compare objective halo measurements with subjective halo perceptions from 22 participants under different spectral conditions. This future research may have the potential to introduce a valid method to align subjective and objective halo perception and to close the gap between established questionnaires to describe halo perception and detailed camera based measurements.

8. References

1. World Health Organization. World report on vision [Internet]. Geneva: World Health Organization; 2019 [cited 2024 Jan 24]. 160 p. Available from: https://iris.who.int/handle/10665/328717

2. Chen SP, Woreta F, Chang DF. Cataracts: A Review. JAMA. 2025 June 17;333(23):2093–103.

3. Liu YC, Wilkins M, Kim T, Malyugin B, Mehta JS. Cataracts. Lancet. 2017 Aug 5;390(10094):600–12.

4. Apple DJ, Sims J. Harold Ridley and the invention of the intraocular lens. Surv Ophthalmol. 1996 Feb;40(4):279–92.

5. Hoffer KJ. Survey on the use of intraocular lenses. Ophthalmology. 1978 Apr;85(4):400–7.

6. Langston RH. Intraocular lens implantation: a review. Artif Organs. 1978 Feb;2(1):55–63.

7. Vacalebre M, Frison R, Corsaro C, Neri F, Santoro A, Conoci S, et al. Current State of the Art and Next Generation of Materials for a Customized IntraOcular Lens according to a Patient-Specific Eye Power. Polymers (Basel). 2023 Mar 22;15(6).

8. Doan KT, Olson RJ, Mamalis N. Survey of intraocular lens material and design. Curr Opin Ophthalmol. 2002 Feb;13(1):24–9.

9. Werner L. Intraocular Lenses: Overview of Designs, Materials, and Pathophysiologic Features. Ophthalmology. 2021 Nov;128(11):e74–93.

10. Pearce JL. Intraocular lenses. Curr Opin Ophthalmol. 1991 Feb;2(1):28–38.

11. Lichtinger A, Rootman DS. Intraocular lenses for presbyopia correction: past, present, and future. Curr Opin Ophthalmol. 2012 Jan;23(1):40–6.

12. Alió JL, Pikkel J, editors. Multifocal Intraocular Lenses: The Art and the Practice [Internet]. Cham: Springer International Publishing; 2019 [cited 2021 Jan 19]. (Essentials in Ophthalmology). Available from: http://link.springer.com/10.1007/978-3-030-21282-7

13. Simpson MJ, Gatinel D, Faria-Ribeiro M, Wei X, Yoon G, Liang J, et al. Design concepts for advanced-technology intraocular lenses [Invited]. Biomed Opt Express. 2025 Jan 1;16(1):334–61.

14. Davison JA, Simpson MJ. History and development of the apodized diffractive intraocular lens. Journal of Cataract and Refractive Surgery. 2006 May;32(5):849–58.

15. Auffarth GU, Rabsilber TM, Kohnen T, Holzer MP. Design und optische Prinzipien von Multifokallinsen. Ophthalmologe. 2008 June;105(6):522–6.

16. Salerno L, Tiveron M, Alió J. Multifocal intraocular lenses: Types, outcomes, complications and how to solve them. Taiwan J Ophthalmol. 2017;7(4):179.

17. Maurino V, Allan BD, Rubin GS, Bunce C, Xing W, Findl O. Quality of Vision after Bilateral Multifocal Intraocular Lens Implantation. Ophthalmology. 2015 Apr;122(4):700–10.

18. Rampat R, Gatinel D. Multifocal and Extended Depth-of-Focus Intraocular Lenses in 2020. Ophthalmology. 2021 Nov;128(11):e164–85.

19. Miller KM, Oetting TA, Tweeten JP, Carter K, Lee BS, Lin S, et al. Cataract in the Adult Eye Preferred Practice Pattern®. Ophthalmology. 2022;129(1):P1–126.

20. Cho JY, Won YK, Park J, Nam JH, Hong JY, Min S, et al. Visual Outcomes and Optical Quality of Accommodative, Multifocal, Extended Depth-of-Focus, and Monofocal Intraocular Lenses in Presbyopia-Correcting Cataract Surgery: A Systematic Review and Bayesian Network Meta-analysis. JAMA Ophthalmology. 2022 Nov 1;140(11):1045–53.

21. Karam M, Alkhowaiter N, Alkhabbaz A, Aldubaikhi A, Alsaif A, Shareef E, et al. Extended Depth of Focus Versus Trifocal for Intraocular Lens Implantation: An Updated Systematic Review and Meta-Analysis. Am J Ophthalmol. 2023 July;251:52–70.

22. Gatinel D, Loicq J. Clinically Relevant Optical Properties of Bifocal, Trifocal, and Extended Depth of Focus Intraocular Lenses. J Refract Surg. 2016 Apr;32(4):273–80.

23. Kohnen T, Suryakumar R. Extended depth-of-focus technology in intraocular lenses. J Cataract Refract Surg. 2020 Feb;46(2):298–304.

24. Wenzel M, Januschowski K, Schayan-Araghi K, Wirbelauer C, Bachmann W, Agostini H, et al. Ergebnisse der aktuellen Umfrage von BDOC, BVA, DGII und DOG und Daten des Statistischen Bundesamtes. 2022 Nov;

25. Wenzel M, Januschowski K, Schayan-Araghi K, Wirbelauer C, Bachmann W, Agostini HJ, et al. Ergebnisse der aktuellen Umfrage von BDOC, BVA, DGII und DOG und Daten des Statistischen Bundesamtes. 2023 Nov;

26. Kim EC, Na KS, Kim HS, Hwang HS. How does the world appear to patients with multifocal intraocular lenses?: a mobile model eye experiment. BMC Ophthalmol. 2020 Dec;20(1):180.

27. Kohnen T, Allen D, Boureau C, Dublineau P, Hartmann C, Mehdorn E, et al. European Multicenter Study of the AcrySof ReSTOR Apodized Diffractive Intraocular Lens. Ophthalmology. 2006 Apr;113(4):578-584.e1.

28. Meikies D, van der Mooren M, Terwee T, Guthoff RF, Stachs O. Rostock Glare Perimeter: a distinctive method for quantification of glare. Optom Vis Sci. 2013 Oct;90(10):1143–8.

29. Mencucci R, Morelli A, Cennamo M, Roszkowska AM, Favuzza E. Enhanced Monofocal Intraocular Lenses: A Retrospective, Comparative Study between Three Different Models. JCM. 2023 May 21;12(10):3588.

30. Shah S, Peris-Martinez C, Reinhard T, Vinciguerra P. Visual Outcomes After Cataract Surgery: Multifocal Versus Monofocal Intraocular Lenses. J Refract Surg. 2015 Oct;31(10):658–66.

31. Giers BC, Khoramnia R, Varadi D, Wallek H, Son HS, Attia MS, et al. Functional results and photic phenomena with new extended-depth-of-focus intraocular Lens. BMC Ophthalmol. 2019 Dec;19(1):197.

32. Kretz FTA, Breyer D, Klabe K, Hagen P, Kaymak H, Koss MJ, et al. Clinical Outcomes After Implantation of a Trifocal Toric Intraocular Lens. J Refract Surg. 2015 Aug 1;31(8):504–10.

33. Hecht S. INTENSITY AND THE PROCESS OF PHOTORECEPTION. Journal of General Physiology. 1920 Mar 20;2(4):337–47.

34. Peli E, Lang A. Appearance of images through a multifocal intraocular lens. J Opt Soc Am A. 2001 Feb 1;18(2):302.

35. Castignoles F, Flury M, Lepine T. Comparison of the efficiency, MTF and chromatic properties of four diffractive bifocal intraocular lens designs. Opt Express. 2010 Mar 1;18(5):5245.

36. Kawamorita T, Uozato H. Modulation transfer function and pupil size in multifocal and monofocal intraocular lenses in vitro. Journal of Cataract and Refractive Surgery. 2005 Dec;31(12):2379–85.

37. Hill W, Carson D, Hong X, Karakelle M. Optical bench performance of AcrySof® IQ ReSTOR®, AT LISA® tri, and FineVision® intraocular lenses. OPTH. 2014 Oct;2105.

38. Lee S, Choi M, Xu Z, Zhao Z, Alexander E, Liu Y. Optical bench performance of a novel trifocal intraocular lens compared with a multifocal intraocular lens. OPTH. 2016 June;1031.

39. Philippaki E, Gobin L, Mandoda J, Lamy S, Castignoles F. Optical evaluation of new-design multifocal IOLs with extended depth of focus. J Opt Soc Am A Opt Image Sci Vis. 2019 May 1;36(5):759–67.

40. Son HS, Labuz G, Khoramnia R, Merz P, Yildirim TM, Auffarth GU. Ray propagation imaging and optical quality evaluation of different intraocular lens models. :11.

41. Ginis HS, Tsoukalas S, Christaras D, Artal P. Visually relevant on-bench through-focus analysis of intraocular lenses. Biomed Opt Express. 2024 Dec 1;15(12):7056.

42. I. O. for Standardization. I. O. for Standardization, ISO 11979-2:2024. ISO. Available at: https://www.iso.org/standard/55682.html. Accessed April 16, 2025

43. Reiß S, Forbrig J, Guthoff R, Terwee T, Stolz H, Siewert S, et al. Optimierung der Visualisierungstechnik für Strahlenverläufe durch Intraokularlinsen zur Charakterisierung multifokaler Abbildungseigenschaften von Fresnel-Zonenplatten. Klin Monatsbl Augenheilkd. 2014 Dec 17;231(12):1183–6.

44. Eppig T, Rubly K, Rawer A, Langenbucher A. Visualization of Light Propagation with Multifocal Intraocular Lenses Using the Ouzo Effect. BioMed Research International. 2019 June 27;2019:1–10.

45. Petelczyc K, Kolodziejczyk A, Błocki N, Byszewska A, Jaroszewicz Z, Kakarenko K, et al. Model of the light sword intraocular lens: in-vitro comparative studies. Biomed Opt Express. 2020 Jan 1;11(1):40.

46. Hinze U, El-Tamer A, Doskolovich LL, Bezus EA, Reiß S, Stolz H, et al. Additive manufacturing of a trifocal diffractive-refractive lens. Optics Communications. 2016 Aug;372:235–40.

47. Fiala W, Pingitzer J. Analytical approach to diffractive multifocal lenses. Eur Phys J AP. 2000 Mar;9(3):227–34.

48. Faklis D, Morris GM. Spectral properties of multiorder diffractive lenses. Appl Opt. 1995 May 10;34(14):2462.

49. I. O. for Standardization. I. O. for Standardization, “ISO/CIE 23539:2023 | CIE TC 2-93 - Photometry - The CIE system of physical photometry,” (2023).

50. Van Norren D, Tiemeijer LF. Spectral reflectance of the human eye. Vision Research. 1986 Jan;26(2):313–20.

51. International Commission on Non-Ionizing Radiation Protection. Revision of guidelines on limits of exposure to laser radiation of wavelengths between 400 nm and 1.4 microm. In Health Physics; 2000.

52. Charman WN, Montes-Mico R, Radhakrishnan H, Papadopoulos R, Bachariou A. Can we measure wave aberration in patients with diffractive IOLs? :1.

53. Campbell CE. Wavefront Measurements of Diffractive and Refractive Multifocal Intraocular Lenses in an Artificial Eye. J Refract Surg. 2008 Jan;24(3):308–11.

54. Gatinel D. Double pass–technique limitations for evaluation of optical performance after diffractive IOL implantation. Journal of Cataract and Refractive Surgery. 2011 Mar;37(3):621–2.

55. Vega F, Faria-Ribeiro M, Armengol J, Millán MS. Pitfalls of Using NIR-Based Clinical Instruments to Test Eyes Implanted with Diffractive Intraocular Lenses. Diagnostics. 2023 Mar 27;13(7):1259.

56. Loicq J, Willet N, Gatinel D. Topography and longitudinal chromatic aberration characterizations of refractive–diffractive multifocal intraocular lenses. Journal of Cataract and Refractive Surgery. 2019 Nov;45(11):1650–9.

57. Holladay JT, Piers PA, Koranyi G, van der Mooren M, Norrby NES. A New Intraocular Lens Design to Reduce Spherical Aberration of Pseudophakic Eyes. J Refract Surg. 2002 Nov;18(6):683–91.

58. Rawer R, Stork W, Spraul CW, Lingenfelder C. Imaging quality of intraocular lenses. Journal of Cataract and Refractive Surgery. 2005 Aug;31(8):1618–31.

59. Alba-Bueno F, Vega F, Millán MS. Design of a Test Bench for Intraocular Lens Optical Characterization. J Phys: Conf Ser. 2011 Jan 1;274:012105.

60. Gerlach M, Guthoff R, Stachs O, Bohn S, Sperlich K. Präklinische Bewertung von Intraokularlinsen durch simulierte Implantation. Klin Monatsbl Augenheilkd. 2018 Dec;235(12):1332–41.

61. Sperlich K, Bohn S, Gerlach M, Schubert J, Stolz H, Guthoff R, et al. In Vivo Acquisition of Human Retinal Double-Pass Images during Simulated Intraocular Lens Implantation. Klin Monbl Augenheilkd. 2024 Dec;241(12):1302–8.

62. Wahl S, Song C, Ohlendorf A. Comparison of two devices to simulate vision with intraocular lenses. OPTH. 2019 Jan;Volume 13:123–30.

63. American National Standards Institute. American National Standard for Ophthalmics - Extended Depth of Focus Intraocular Lenses. ANSI Z80.35-2018, 2018.

64. Sperlich K, Stolz H. Quantum efficiency measurements of (EM)CCD cameras: high spectral resolution and temperature dependence. Meas Sci Technol. 2014 Jan 1;25(1):015502.

65. Gonzalez RC, Woods RE. Digital image processing. 2. ed., internat. ed. Upper Saddle River, NJ: Prentice-Hall; 2002. 793 p.

66. Cheezum MK, Walker WF, Guilford WH. Quantitative Comparison of Algorithms for Tracking Single Fluorescent Particles. Biophysical Journal. 2001 Oct;81(4):2378–88.

67. Shuang B, Chen J, Kisley L, Landes CF. Troika of single particle tracking programing: SNR enhancement, particle identification, and mapping. Phys Chem Chem Phys. 2014;16(2):624–34.

68. Watson AB. A formula for human retinal ganglion cell receptive field density as a function of visual field location. Journal of Vision. 2014 June 30;14(7):15.

69. Guillon M, Dumbleton K, Theodoratos P, Gobbe M, Wooley CB, Moody K. The Effects of Age, Refractive Status, and Luminance on Pupil Size. Optom Vis Sci. 2016 Sept;93(9):1093–100.

70. Pieh S. Halo size under distance and near conditions in refractive multifocal intraocular lenses. British Journal of Ophthalmology. 2001 July 1;85(7):816–21.

71. Vega F, Alba-Bueno F, Millán MS, Varón C, Gil MA, Buil JA. Halo and Through-Focus Performance of Four Diffractive Multifocal Intraocular Lenses. Invest Ophthalmol Vis Sci. 2015 June 19;56(6):3967.

72. Gatinel D, Pagnoulle C, Houbrechts Y, Gobin L. Design and qualification of a diffractive trifocal optical profile for intraocular lenses. Journal of Cataract and Refractive Surgery. 2011 Nov;37(11):2060–7.

73. Vega F, Millán MS, Vila-Terricabras N, Alba-Bueno F. Visible Versus Near-Infrared Optical Performance of Diffractive Multifocal Intraocular Lenses. Invest Ophthalmol Vis Sci. 2015 Nov 16;56(12):7345.

74. Jun I, Choi YJ, Kim EK, Seo KY, Kim T i. Internal spherical aberration by ray tracing-type aberrometry in multifocal pseudophakic eyes. Eye. 2012 Sept;26(9):1243–8.

75. Santhiago M, Netto M, Barreto J, Gomes B, Schaefer A, Kara-Junior N. Wavefront analysis and modulation transfer function of three multifocal intraocular lenses. Indian J Ophthalmol. 2010;58(2):109.

76. Haddad JS, Gouvea L, Ferreira JL, Ambrósio R, Waring GO, Rocha KM. Impact of a Chromatic Aberration-Correcting Intraocular Lens on Automated Refraction. J Refract Surg. 2020 May;36(5):334–9.

77. Ju RH, Wu ZM, Aier Eye Hospital, Jinan University, Guangzhou 510071, Guangdong Province, China, Chen Y, Aier Eye Hospital, Jinan University, Guangzhou 510071, Guangdong Province, China, Wu LN, et al. Comparison of visual performance with iTrace analyzer following femtosecond laser-assisted cataract surgery with bilateral implantation of two different trifocal intraocular lenses. Int J Ophthalmol. 2023 Nov 18;16(11):1773–81.

78. Pilger D, Homburg D, Brockmann T, Torun N, Bertelmann E, Von Sonnleithner C. Clinical outcome and higher order aberrations after bilateral implantation of an extended depth of focus intraocular lens. European Journal of Ophthalmology. 2018 July;28(4):425–32.

79. Li BW, Huang H, Huang MS, Guo SL, Gao L, Zeng YY, et al. Changes in visual performance after implantation of different intraocular lenses. Int J Ophthalmol. 2024;17(7):1273–82.

80. Mojzis P, Kukuckova L, Majerova K, Liehneova K, Piñero DP. Comparative Analysis of the Visual Performance After Cataract Surgery With Implantation of a Bifocal or Trifocal Diffractive IOL. J Refract Surg. 2014 Oct;30(10):666–72.

81. Velasco-Barona C, Corredor-Ortega C, Mendez-Leon A, Casillas-Chavarín NL, Valdepeña-López Velarde D, Cervantes-Coste G, et al. Influence of Angle κ and Higher-Order Aberrations on Visual Quality Employing Two Diffractive Trifocal IOLs. Journal of Ophthalmology. 2019 Nov 27;2019:1–8.

82. Garzón N, García-Montero M, López-Artero E, Poyales F, Albarrán-Diego C. Influence of trifocal intraocular lenses on standard autorefraction and aberrometer-based autorefraction. Journal of Cataract and Refractive Surgery. 2019 Sept;45(9):1265–74.

83. Souza CE, Muccioli C, Soriano ES, Chalita MR, Oliveira F, Freitas LL, et al. Visual performance of AcrySof ReSTOR apodized diffractive IOL: a prospective comparative trial. Am J Ophthalmol. 2006 May;141(5):827–32.

84. Zelichowska B, Rekas M, Stankiewicz A, Cerviño A, Montés-Micó R. Apodized diffractive versus refractive multifocal intraocular lenses: optical and visual evaluation. J Cataract Refract Surg. 2008 Dec;34(12):2036–42.

85. Carballo-Alvarez J, Vazquez-Molini JM, Sanz-Fernandez JC, Garcia-Bella J, Polo V, García-Feijoo J, et al. Visual outcomes after bilateral trifocal diffractive intraocular lens implantation. BMC Ophthalmol. 2015 Dec;15(1):26.

86. Alió JL, Plaza-Puche AB, Alió Del Barrio JL, Amat-Peral P, Ortuño V, Yébana P, et al. Clinical outcomes with a diffractive trifocal intraocular lens. European Journal of Ophthalmology. 2018 July;28(4):419–24.

87. Chen T, Yu F, Lin H, Zhao Y, Chang P, Lin L, et al. Objective and subjective visual quality after implantation of all optic zone diffractive multifocal intraocular lenses: a prospective, case-control observational study. Br J Ophthalmol. 2016 Nov;100(11):1530–5.

88. Hwang, Ho Sik, Shin, Hye Young, Joo, Choun-Ki. Double-Pass System (Optical Quality Analysis System) for Analysis of the Multifocal Function of a Diffractive Multifocal Intraocular Lens (Acrysof ReSTOR®) Compared to a Monofocal Intraocular Lens (Acrysof IQ®). Journal of the Optical Society of Korea. 2014 Apr 25;18(2):110–7.

89. Liao X, Lin J, Tian J, Wen B, Tan Q, Lan C. Evaluation of Optical Quality: Ocular Scattering and Aberrations in Eyes Implanted with Diffractive Multifocal or Monofocal Intraocular Lenses. Current Eye Research. 2018 June 3;43(6):696–701.

90. Moreno LJ, Piñero DP, Alió JL, Fimia A, Plaza AB. Double-pass system analysis of the visual outcomes and optical performance of an apodized diffractive multifocal intraocular lens. Journal of Cataract and Refractive Surgery. 2010 Dec;36(12):2048–55.

91. Castillo-Gómez A, Carmona-González D, Martínez-de-la-Casa JM, Palomino-Bautista C, García-Feijoo J. Evaluation of image quality after implantation of 2 diffractive multifocal intraocular lens models. Journal of Cataract and Refractive Surgery. 2009 July;35(7):1244–50.

92. Lee YW, Choi CY, Moon K, Jeong YJ, An SI, Lee JM, et al. Clinical outcomes of new multifocal intraocular lenses with hydroxyethyl methacrylate and comparative results of contrast sensitivity, objective scatter, and subjective photic phenomena. BMC Ophthalmol. 2022 Sept 21;22(1):379.

93. Pedrotti E, Bruni E, Bonacci E, Badalamenti R, Mastropasqua R, Marchini G. Comparative Analysis of the Clinical Outcomes With a Monofocal and an Extended Range of Vision Intraocular Lens. J Refract Surg. 2016 July 1;32(7):436–42.

94. Liu H, Li FF, Xia HJ, Zhou J. Visual quality after implantation of trifocal intraocular lenses in highly myopic eyes with different axial lengths. Int J Ophthalmol. 2021;14(3):371–7.

95. Fernández J, Burguera N, Rocha-de-Lossada C, Rachwani-Anil R, Rodríguez-Vallejo M. Influence of a multifocal intraocular lens centration and eye angles on light distortion and ocular scatter index. Graefes Arch Clin Exp Ophthalmol [Internet]. 2023 Mar 8 [cited 2023 May 12]; Available from: https://link.springer.com/10.1007/s00417-023-06028-x

96. Frey K, Hage H, Gerlach M, Brunner R. Topography Profiling: Measuring the topography of soft ophthalmological components immersed in water. Optik & Photonik. 2015 Dec;10(5):27–30.

97. Mendroch D, Altmeyer S, Oberheide U. Characterization of diffractive bifocal intraocular lenses. Sci Rep. 2023 Jan 17;13(1):908.

98. Hain R. Comparison of CCD, CMOS and intensified cameras. Exp Fluids. 2007;9.

Declaration of Independence

I hereby declare that I have written this dissertation entitled “Challenges in the Evaluation of Multifocal Intraocular Lenses” myself and have not used any aids or sources other than the references given.

Rostock, 25.10.2025

Ricardo Elsner

Acknowledgments

I would like to express my heartfelt gratitude to everyone who supported me in completing this dissertation.

First and foremost, I extend my deepest thanks to my doctoral advisor, Prof. Dr. rer. nat. Oliver Stachs, and my supervisor, Dr. rer. nat. Karsten Sperlich, for granting me the opportunity to work on such a fascinating dissertation topic. Their outstanding guidance and unwavering support were instrumental in the success of this work. The collaboration was always pleasant, and their shared enthusiasm for this project, coupled with constructive discussions, allowed this research to evolve into something truly exceptional.

I am particularly grateful to Dr. rer. nat. Sebastian Bohn and Jan Sievers, MSc, whose expertise and invaluable assistance played a crucial role in conducting the investigations and preparing the scientific publications. I also want to express my sincere thanks to Prof. Dr. rer. nat. Henije Stolz and Mario Gerlach, MSc, for their insightful advice and professional support in addressing complex questions.

My highest appreciation goes to the voluntary participants of the study, whose willingness to take part despite the challenges made this research possible. Conducting the clinical investigations with each of you was a unique and rewarding experience. I wish you all the very best and, above all, good health for the future!

A special note of gratitude goes to the *Landesgraduiertenförderung Mecklenburg-Vorpommern* for financially supporting this research through their scholarship and for placing their trust in this long-term project. Their support has been vital in enabling this work to come to fruition.

Lastly, I would like to thank my wife, family, and friends, who stood by me through every high and low, offering unwavering encouragement and support. Without you, none of this would have been possible. Thank you for everything!

Curriculum vitae

Education

10/2008 – 06/2016: **Gymnasium Dresden-Bühlau,** Dresden, Germany
Completed with Abitur (University Entrance Qualification)

10/2016 – 06/2024: **University of Rostock**; Rostock, Germany
Medical Studies and Medical License
Final Score: 1.83

09/2020 – 02/2021: **Universidad de Granada**; Granada, Spain
Medical Studies - Clinical Section for Second State Examination
International Fellowship: Erasmus+

02/2022 – 03/2022: **Universidad Autonoma de Coahuila**; Saltillo, Mexico
Medical Studies - Clinical Internship in General Surgery
IFMSA: SCOPE Exchange

11/2022 – 04/2023: **Brown University**; Providence, United States of America
Medical Studies in Internal Medicine - Part of Practical Year (PJ)
PROMOS Fellowship

09/2023 – 12/2023: **Charité - Universitätsmedizin Berlin**; Berlin, Germany
Medical Studies in Ophthalmology- Part of Practical Year (PJ)

01/2024 – 02/2024: **Hospital Italiano de Buenos Aires**; Buenos Aires, Argentina
Medical Studies in Neurosurgery- Part of Practical Year (PJ)

03/2024 – 04/2024: **Charité - Universitätsmedizin Berlin**; Berlin, Germany
Medical Studies in Vascular Surgery- Part of Practical Year (PJ)

Professional Experience

10/2024: United States Medical Licensing Examination – Step 1

01/2025 - Present: Resident Physician in Ophthalmology; Charité CVK, Berlin

Scholarships & Certificates

- *Deutsche Bildung Programm Agreement*, Frankfurt, Germany (2019 - 2024)
- *ERASMUS Exchange Scholarship*, Rostock, Germany (Aug 2020 - Mar 2021): Erasmus+ semester in Granada
- *SCOPE Exchange Scholarship* (IFMSA) in Saltillo, Mexico (Feb - Mar 2022)
- *Doctoral Scholarship*, State Graduate Funding Mecklenburg-Vorpommern (Oct 2021 - 2023): 1 of 4 scholarships promoting scientific talent in MV
- *Practical Year Scholarship (PROMOS Fellowship)*, Rostock, Germany (Nov 2022 - Apr 2023) at Brown University, Providence, RI, USA

List of publications

The following original works will be included in the cumulative dissertation:

[Pub. I]: Sievers J, **Elsner R**, Bohn S, Schünemann M, Stolz H, Guthoff RF, Stachs O, Sperlich K. *Method for the generation and visualization of cross-sectional images of three-dimensional point spread functions for rotationally symmetric intraocular lenses*. Biomed Opt Express. 2022 Feb 1;13(2):1087-1101. doi: 10.1364/BOE.446869. PMID: 35284182; PMCID: PMC8884235. **(IF = 3.2)**

[Pub. II]: Elsner R, Sievers J, Kunert M, Reiss S, Bohn S, Schünemann M, Stolz H, Guthoff R, Stachs O, Sperlich K. *The Rostock Method for Qualitative and Quantitative Evaluation of Intraocular Lenses*. Klin Monbl Augenheilkd. 2022 Dec;239(12):1440-1446. English, German. doi: 10.1055/a-1953-7302. Epub 2022 Dec 9. PMID: 36493765. **(IF = 0.8)**

[Pub. III]: Elsner R, Gerlach M, Bohn S, Sievers J, Stolz H, Guthoff RF, Stachs O, Sperlich K. *Assessment of Diffractive Intraocular Lenses Using Near-Infrared Light: A Critical Evaluation.* Transl Vis Sci Technol. 2025 Jun 2;14(6):36. doi: 10.1167/tvst.14.6.36. PMID: 40586669; PMCID: PMC12212444. **(IF = 3.28)**

Theses

1) Die Katarakt, eine Trübung der natürlichen Augenlinse, stellt eine der häufigsten Ursachen für eine Sehverschlechterung im höheren Lebensalter dar. Ihre einzige kausale Therapie besteht in der operativen Implantation einer künstlichen Intraokularlinse (IOL).

2) Monofokale IOLs erzeugen nur einen Brennpunkt und erfordern daher meist eine postoperative Korrektur durch eine Brille für Ferne oder Nähe. Multifokale IOLs (MIOLs) hingegen erzeugen mehrere Brennpunkte, z.B. für Ferne, Intermediärdistanz und Nähe, mit dem Ziel einer weitgehenden Brillenunabhängigkeit.

3) Aufgrund ihrer diffraktiven und refraktiven optischen Prinzipien sind MIOLs häufig mit photischen Phänomenen wie Halos, Streulicht oder Blendungseffekten assoziiert, was eine präzise präklinische und klinische Evaluation dieser Linsen notwendig macht.

4) Die Abbildungseigenschaften einer IOL lassen sich durch ihre Punktspreizfunktion (Point Spread Function, PSF) beschreiben. Auf Basis zahlreicher zweidimensionaler PSF-Aufnahmen kann eine dreidimensionale PSF generiert werden, welche eine detaillierte Analyse der IOL Performance ermöglicht.

5) Optische Bänke ermöglichen eine präklinische Charakterisierung von MIOLs, indem der Strahlenverlauf und die Fokuspunkte der MIOL mithilfe von Querschnittsbildern (Cross Sectional Images, CSI) visualisiert werden.

6) Herkömmliche Verfahren nutzen u.a. die Anregung und Lichtemission von Fluorescein oder Lichtstreuung an Ouzo oder Milch in einem Wasserbad zur Darstellung von Strahlenverläufen und Fokuspunkten der untersuchten IOLs. Diese Verfahren sind jedoch anfällig für Signalüberlagerungen und Kontrastverluste innerhalb der Querschnittsbilder.

7) In dieser Arbeit wurde der Einfluss der Lichtblattdicke auf die Qualität der Querschnittsbilder (CSI) untersucht. Eine zunehmende Lichtblattdicke führt zu einer Abnahme der Kontrastschärfe, da Hintergrundrauschen und Signale benachbarter Fokusebenen die Abbildungsqualität beeinträchtigen.

8) Zur Optimierung der Bildqualität wurde ein neuartiger Bildverarbeitungsalgorithmus entwickelt, der das rotationssymmetrische Design von IOLs nutzt, um rotationsgemittelte Querschnittsbilder (Rotationally Averaged Cross-Sectional Images, RA-CSI) zu erzeugen. Dieser Ansatz führt zu einer signifikanten Verbesserung des Signal-zu-Rausch-Verhältnis und der räumlichen Auflösung feiner Lichtverteilungen.

9) Durch die rotationsgemittelten Querschnittsbilder lassen sich Fokuspositionen und Lichtverläufe mit höherer Präzision darstellen, was insbesondere für diffraktive MIOLs mit komplexen Beugungsordnungen von Vorteil ist.

10) Auf Grundlage der RA-CSI-Daten können reproduzierbare Metriken wie Durchfokuskurven und Energieeffizienzen abgeleitet werden, die eine standardisierte und vergleichbare Bewertung der optischen Leistungsfähigkeit unterschiedlicher IOL-Designs ermöglichen.

11) Es konnte gezeigt werden, dass Nahinfrarot-basierte (NIR) Messverfahren, die häufig in der klinischen Evaluation von IOLs eingesetzt werden, bei diffraktiven MIOLs zu fehlerhaften Ergebnissen führen können.

12) IOLs werden im Allgemeinen für Licht im sichtbaren, v.a. grünen, Spektrum designt. Da refraktive als auch diffraktive IOL Designs wellenlängenabhängig wirken, verändert sich unter NIR-Beleuchtung die Lichtverteilung in den Fokuspunkten. Die untersuchte diffraktive, trifokale IOL verhält sich unter diesen Bedingungen nahezu monofokal, was auf die physikalischen Prinzipien der Lichtbeugung zurückzuführen ist.

13) Die Fokuspositionen und Energieverteilungen variieren in Abhängigkeit von der Wellenlänge. Dies muss bei präklinischen und klinischen Messungen berücksichtigt werden, um Fehlinterpretationen der optischen Leistung diffraktiver IOLs zu vermeiden.

14) Der entwickelte Algorithmus stellt eine präzise und reproduzierbare Methode zur optischen Charakterisierung von MIOLs dar, ist jedoch mit erhöhter Komplexität bei der IOL Justierung und mit langen Rechenzeiten verbunden.

15) Trotz der hohen Aussagekraft der Messergebnisse von optischen Bänken lassen sich wegen der komplexen, in erster Näherung logarithmischen Empfindlichkeit des Auges daraus keine direkten Rückschlüsse auf die subjektive Wahrnehmung von Dysphotopsien, wie Halos, Streulicht oder Blendungseffekten, ziehen.

16) Künftige Forschungsansätze sollten objektive optische Metriken mit subjektiven Wahrnehmungsanalysen in einem vereinheitlichten optischen Aufbau kombinieren, um die visuelle Qualität multifokaler IOLs umfassender beurteilen zu können und dadurch ein optimales Outcome für Patienten zu gewährleisten.

Appendix

The following publications constitute the cumulative part of this dissertation. They are reproduced here with the kind permission of the respective publishers. The version of record is presented.

Research Article | Vol. 13, No. 2 / 1 Feb 2022 / *Biomedical Optics Express* 1087

Biomedical Optics EXPRESS

Method for the generation and visualization of cross-sectional images of three-dimensional point spread functions for rotationally symmetric intraocular lenses

JAN SIEVERS,[1,2,3] RICARDO ELSNER,[1,2] SEBASTIAN BOHN,[1,2] MELANIE SCHÜNEMANN,[1,2] HEINRICH STOLZ,[2,4] RUDOLF F. GUTHOFF,[1,2] OLIVER STACHS,[1,2] AND KARSTEN SPERLICH[1,2,*]

[1] *Department of Ophthalmology, Rostock University Medical Center, 18057 Rostock, Germany*
[2] *Department Life, Light & Matter, University of Rostock, 18055 Rostock, Germany*
[3] *Institute of Physics, Martin–Luther–University Halle–Wittenberg, 06120 Halle (Saale), Germany*
[4] *Institute of Physics, University of Rostock, 18055 Rostock, Germany*
[*] *karsten.sperlich@uni-rostock.de*

Abstract: Cross-sectional images of three-dimensional point spread functions of intraocular lenses are used to study their image formation. To obtain those, light sheet-based methods are established. Due to the non-negligible thicknesses of the light sheets, the image quality of the cross-sectional images is constrained. To overcome this hurdle, we present a dedicated evaluation algorithm to increase image quality in the post-processing step. Additionally, we compare the developed- with the light sheet method based on our own investigations of a multifocal diffractive intraocular lens conducted in an in-house designed optical bench. The comparative study showed the clear superiority of the newly developed method in terms of image quality, fine structure visibility, and signal-to-noise ratio compared to the light sheet based method. However, since the algorithm assumes a rotationally symmetrical point spread function, it is only suitable for all rotationally symmetrical lenses.

© 2022 Optica Publishing Group under the terms of the Optica Open Access Publishing Agreement

1. Introduction

During cataract surgery, the natural eye lens is removed and replaced by an intraocular lens (IOL). The simplest IOL is a monofocal lens [1]. In this case, patients can only see sharp at one distance and need visual aids for other distances. Multifocal IOLs (MIOLs), among others, provide independence from visual aids. These have two or more focal points [2]. Multifocality of IOLs is realized by principles of refraction, diffraction, or a combination of both [3–5].

To verify the manufacturers' data and to compare the optical properties of IOLs with each other, experimental determination of these properties is essential. For this reason, it is an important part of preclinical IOL testing.

Simpson used the EROS solid state MTF equipment (formerly Ealing Electro-Optics, now Coherent, Santa Clara, USA) to capture the line spread functions and calculate the corresponding modulation transfer functions (MTFs) using the Fourier transform [6]. Carretero et al. as well as Bos et al. developed interferometric approaches based on an optical bench design to analyze optical properties of IOLs. [7,8]. Ravalico et al. presented one of the first in-house optical benches for capturing 2D-PSF images at the focal points of several IOLs and computed the energy efficiency [9]. All of these early stage optical benches had the similar characteristics of the nowadays used optical benches like a collimated beam of light source, IOL stored in a model eye, camera for data acquisition and computer for data processing, but each setup with different specifications and parameters and hence impeding direct comparisons of these early results.

#446869 https://doi.org/10.1364/BOE.446869
Journal © 2022 Received 25 Oct 2021; revised 21 Dec 2021; accepted 30 Dec 2021; published 1 Feb 2022

Biomedical Optics EXPRESS

To ensure comparability of the optical IOL properties, the ISO standard 11979-2:2000-07 [10] was established in the year 2000 recommending the use of an optical bench with special technical specifications as the experimental setup for IOL examinations. Since its establishment, most papers on the research of optical properties of IOLs focus on the determination of MTFs and through-focus MTFs using optical benches, e.g. [11–15].

Generally, such a setup allows recording the 3D light distribution caused through the investigated IOL by moving a microscope camera unit along the optical axis capturing images of the 2D point spread function (2D-PSF) of the IOL at different axial positions. By lining up all the images of a captured image stack to a 3D image, the light distribution inside the volume corresponds to the 3D point spread function (3D-PSF) of the investigated IOL. Using this technique, Millán et al. captured the 3D-PSFs of three MIOLs to study the through-focus energy efficiency and longitudinal chromatic aberration [16]. Another important IOL property which can be calculated from a captured 3D-PSF is the cross-sectional image (CSI). It is thus determined by cutting out a thin volume of the captured 3D-PSF along the optical axis and averaging the lateral intensity distribution line by line. To the best of our knowlede, Petelczyc et al. used this technique for the first time to calculate the CSIs of six selected MIOLs using data captured with an in-house optical bench [17].

Another approach to acquire CSIs of IOLs is the application of a fluorescein bath, which is described in detail in [18]. A thin light sheet illuminates an IOL placed in a fluorescein bath. The light distribution occurring behind the IOL becomes visible due to the fluorescence of the excited fluorescein. Light emitted laterally to the optical axis of the system, due to fluorescence and scattering, is captured by a camera mounted perpendicular to the resulting CSI. Due to the finite width of the light sheet, the fluorescein molecules are stimulated within a volume along the optical axis. Thus, the cross-sectional image captured by the camera equals the averaged intensity distribution of the illuminated volume. The use of scattering particles like Ouzo or milk powder is possible as well and offers an alternative to the fluorescein molecules [19,20].

The CSIs acquisition and analysis of IOLs is a well-established component of preclinical IOL examinations [21]. These profiles are used to study the experimental image formation created by the investigated IOL [22]. Further, important parameters such as through-focus curves, MTFs, lateral intensity distributions and add powers of MIOLs can be derived from CSIs [19,20,23,24].

Both methods are light sheet-based and the standard for the determination of cross-sectional images in this field of research but the thickness of the light sheet in the case of the fluorescein bath or the width of the extracted volume in the case of the optical bench always results in an image quality decrease of the investigated cross-sectional images.

Many IOLs have a rotationally symmetric design, a fact, that we exploit to increase the image quality and signal-to-noise ratio. In this work, we use an in-house designed optical bench for the automatic acquisition of 3D-PSFs at various pupil sizes for a trifocal diffractive AT LISA tri 839MP (Carl Zeiss Meditec AG, Jena, Germany). In addition, we present a proprietary algorithm for exploiting the rotational symmetry. The new algorithm was applied to the obtained 3D-PSFs to determine the CSIs and subsequently compared with the standard, light sheet-based methods in terms of their image qualities, signal-to-noise ratios, and fine feature visibilities.

2. Methods

2.1. Experimental setup

Our in-house designed optical bench is based on the ISO 11979-2:2014-12 standard [25] and the documented optical benches of other working groups investigating imaging properties of IOLs [17,26,27]. Figure 1 shows the schematic illustration of the experimental setup for obtaining the IOL light distribution. The green LED light with a central wavelength $\lambda = 530$ nm and a FWHM = 47 nm passes a pinhole (10 µm, Thorlabs, Newton, New Jersey, USA) and is collimated by an achromatic lens (f = 150 mm, AC254-150-A1, Thorlabs, Newton, New Jersey, USA). The

Biomedical Optics EXPRESS

diameter of the parallel beam can be changed by an aperture (SM1D12C, Thorlabs, Newton, New Jersey, USA). The model eye was originally designed for the VirtIOL (10Lens S.L.U., Terrassa, Spain) device, which is a see-through device for the simulated implantation of IOLs [28–30].

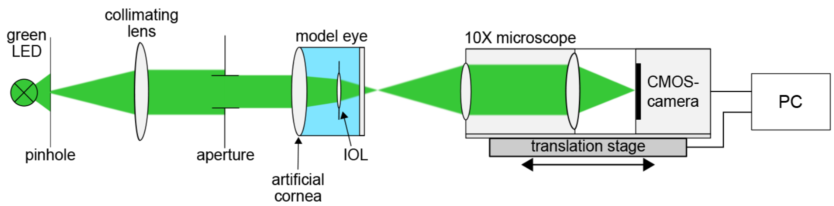

Fig. 1. Schematic illustration of the optical bench for the measurement of the 3D-PSF of the investigated IOL.

It consists of an achromatic lens (f = 40 mm) as an artificial cornea on the front side, a glass window on the backside, and an IOL holder in between. The medium inside the model eye is distilled water. Simulations with the ray-tracing software FRED Optical Engineering Software 18.61.2 (Photon Engineering, Tucson, Arizona, USA) showed a linear dependency between the aperture diameter d_{A} and the illuminated diameter of the IOL d_{IOL}:

$$d_{\mathrm{IOL}} = 0.978 \cdot d_{\mathrm{A}} \tag{1}$$

The scaling factor depends on the focal length and the distance between model cornea and IOL. This distance was in our case about ≈ 2.1 mm. Behind the model eye, a microscope objective (IC-10 MD-Plan, NA = 0.25, Olympus, Shinjuku, Japan) and a 12-Bit monochrome CMOS-camera (UE-3880CP-M-GL, IDS Imaging Development Systems GmbH, Obersulm, Germany) with an image resolution of 3088×2076 pixels and a pixel size of 2.4 µm are attached to a translation stage which can be moved along the optical axis. Further, the translation stage is motorized using a NSC200-Controller and a TRA25PPM actuator (both Newport Corporation, Irvine, California, USA). The camera and the translation stage are both controlled by a dedicated script in LabVIEW 2019 SP1 (National Instruments Corporation, Austin, Texas, USA). Accordingly, multiple images of the IOL light distribution can be captured automatically for different axial positions. For the presented experiments, the total travel distance of the translation stage $s = 1.91$ mm with an increment $\Delta s = 7.63$ µm is used. Hence, a stack of images includes 251 images. For each position, the light distribution and the background signal are captured multiple times.

2.2. Proprietary algorithm for cross-sectional image determination

A proprietary algorithm, written in Mathematica 12.0 (The Wolfram Centre, Oxfordshire, United Kingdom), was used for automated analysis of the captured 3D-PSF. Considering the fact, that the surface of the investigated diffractive MIOL is rotationally symmetric and consequently the 3D-PSF too, an annulus integration method can be applied. In short, the general procedure is as follows. Each camera image is divided into a small central disk surrounded by thin annuli with a specific width. Afterward, the intensity in each zone is summed up, the background is estimated by a linear fit and subtracted (cf. Fig. 2(a)). In the next step, this noise corrected intensity profile is divided by its area (cf. Fig. 2(b)), resulting in an array of intensity values from the center to the edge for each axial position. These arrays are then merged to form an image that, together with its mirror image on the optical axis, produces the averaged cross-sectional image of the 3D PSF. In the following, we will explain this procedure in more detail and how to circumvent the aforementioned decrease in image resolution.

For each axial position, the averaged 12-bit camera images and the corresponding averaged background images are imported and subtracted. Negative pixel values are replaced by their

Biomedical Optics EXPRESS

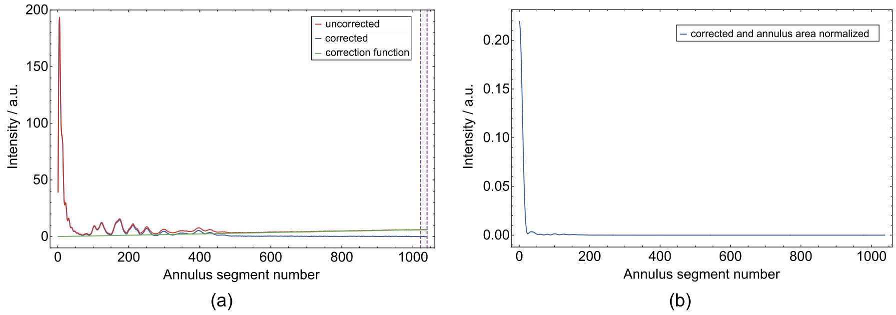

Fig. 2. (a) Exemplary explanation of the noise correction by a linear correction function. Due to the linear area growth of the annuli and high gray values of the focal point area comparing to the outer image regions. The peak of the shown intensity profile is not located in the origin. (b) The noise corrected and annulus segment area normalized intensity course as a function of the annulus segment number. The central peak is located in the origin.

absolute values. To ensure that the intensity distributions are not shifted with respect to the concentric rings, the light distribution of each image is centered on the center point of the image. The annulus integration method is realized using an annuli mask. This one is determined by dividing the image for the used image resolution into a central disk and surrounding concentric circular rings with a constant width of 4 px. The pixel positions of the disk and each annulus are classified and saved in the file of the annuli mask which has to be calculated only once since the image resolution remains the same during the experiments. However, due to the specific width of each circular ring, the final cross-sectional image resolution is decreased in one dimension. To circumvent the decrease, the corrected images are upsampled by a factor of four using cubic spline interpolation (Mathematica function `IMAGERESIZE` with the method "Cubic"). With the annuli mask, the pixel classified to one of the concentric rings can be extracted for each enlarged image of an image stack (Mathematica function `EXTRACT`). Further, the intensity of each concentric ring is calculated by adding up the intensities of the corresponding pixels. Thus, the intensity distribution of each image is represented as an intensity function depending on the concentric rings.

Due to the constant radius, the area of the concentric rings increases linearly from the center outward to the periphery of the image. The noise term of the intensity signal thus increases linearly from the center outwards. This noise signal, occurring in each of the new intensity distributions of the images, is canceled out by a linear correction function and shown exemplarily in Fig. 2(a). The uncorrected intensity curve, shown as –, and the corrected intensity curve, shown as –, are presented as a function of the annulus segment number. The slope of the noise correction function, illustrated as –, is determined by the intensity values of the 20 highest annulus segment numbers, illustrated as - -, and the fact that the correction function has to pass through the coordinate origin. Notice, the peak of the shown intensity as a function of the annulus segment number is not located at segment number = 0, due to the linear area growth of the annulus and high gray values of the focal point comparing to the outer image regions. The corrected intensity curves are normalized to the various annulus segment areas that shifts the peak position to the segment number = 0.

In the next step, the corrected and area-normalized 1D-intensity profiles of each image (see. Fig. 2(b)) are lined up, mirrored, and presented as an overview graphic in intensity-dependent gray values, which is the cross-sectional image of the investigated intraocular lens. A cross-sectional profiles calculated with the new annulus integration method is referred to as rotationally averaged cross-sectional image (RA-CSI) in the following.

The highly parallelized Mathematica algorithm needs still ≈ 40 min for the complete evaluation of an image stack with 251 images using a workstation equipped with an AMD Ryzen 9 3950X processor with 16 cores at 3.493 GHz (AMD, Santa Clara, USA) and 32 GB RAM.

Throughout the rest of the manuscript, this proprietary algorithm is referred to as new algorithm.

2.3. Signal-to-noise ratio

The signal-to-noise ratio (SNR) is generally defined as the ratio of the averaged signal amplitude divided by the noise variance. This metric is used to determine the quality of measured signals. The higher the SNR value the better the quality of the measured signal. Depending on the field of application, modifications of the general definition of SNR exist.

In this paper, the SNR is defined as:

$$\mathrm{SNR} = \frac{(A_\mathrm{S} - A_\mathrm{N})}{\sigma_\mathrm{N}}, \tag{2}$$

where A_S and A_N are the averaged amplitude pf the captured signal and noise, respectively, and σ_N denotes the variance of the noise [31,32]. The amplitude of the signal A_S is calculated by the 16 pixels around the center point of each 2D-PSF image. The variance σ_N and the amplitude A_N of the noise, respectively, are determined from four 2×2 pixels squares, one of which is located in each corner of the respective 2D-PSF image.

2.4. IOL and measurement specifications

The IOL under investigation is a diffractive trifocal AT LISA tri 839MP (Carl Zeiss Meditec AG, Jena, Germany) with a base optical power for the far focus of 22.5 dpt with +3.33 dpt and +1.66 dpt add powers for the near and the intermediate foci respectively.

Image stacks of the 3D-PSFs were measured for the value d_IOL from 2.5 mm to 6.0 mm in 0.5 mm steps. For each axial position of the image stacks, six single images were captured of the 2D-PSF and the background signal, respectively. The obtained 3D-PSFs were evaluated with the previously explained algorithm.

3. Results

3.1. Influence of the light sheet width on the cross-sectional image

An image stack with six images and six background images for each axial position in a 12-Bit format was captured using the presented optical bench for an aperture d_A of 3 mm. This pupil diameter is prescribed by ISO standard 11979-2 [25] for the investigation of IOLs and has its origin in the reduced pupil diameter according to the average age of cataract patients under photopic conditions [33,34]. By using the first part of the new algorithm, the different centered and background signal corrected 3D-PSFs were determined.

In analogy to the light sheet-based method, the cross-sectional image of the 3D-PSF was determined by extracting a narrow volume consisting of 15, 150, 1500 pixels, respectively, of the averaged and background corrected images of the image stack. Those specific pixel ranges were chosen for the following reasons, starting with the last one mentioned.

Peteclczyc et al. used an optical bench for recording 3D-PSFs of several MIOLs. Further, they reported that "··· Figure 4 shows Through-Focus PSFs (TF PSFs) composed of perpendicular projections of all 101 PSFs, obtained for successive defocus values in the linear light intensity scale. Each projection was created by calculating the cumulated intensities of every cross-section of the PSF along the horizontal axis. . . ." [17]. Accordingly, we present also a horizontal projection cross-sectional image (P-CSI) with a reduced width of 1500 pixels. In the case of using a fluorescein bath, the investigated IOL is illuminated by a light sheet. ReiB et al. used a light sheet with 0.35 mm [18] and Eppig et al. a light sheet with a width of 0.3 mm [20]. For

Biomedical Optics EXPRESS

the used optical components and the investigated trifocal MIOL, the latter width corresponds on average of the three widths of the focal points to a sensor width of 159 pixels and the first one to a sensor width of 136 pixels. Accordingly, those two widths of the light sheets match on medium to a sensor width of ≈ 150 pixels. Furthermore, the CSI is shown for a width of 15 pixels to investigate the intensity of the wave propagation in a thin volume along the optical axis. The selected light sheet widths on the sensor of 15, 150, and 1500 pixels correspond to a light sheet thicknesses t of 4.3, 43, and 430 µm, respectively.

Fig. 3 shows these cross-sectional images in intensity-dependent gray values with (left side) linearly and (right side) logarithmically scaled intensities due to the linearity of the camera sensor and the logarithmic visual perception of the human eye [35,36]. The lateral image areas of the shown CSI, perpendicular to the axial position, are trimmed and stretched linearly to three times the width of the original to improve the visibility of the separate light rays. Further, each of the CSIs is scaled to its maximum intensity value. The near focus is at an axial position of ≈ 0.3 mm, the intermediate focus at ≈ 0.9 mm and the far focus at ≈ 1.35 mm. First, we will take a closer look at the linear scaled CSIs. The CSI of 4.3 µm width shows the three focal points, which are clearly spatially separated from each other, as well as ray extensions at the outer focal areas along the optical axis. As the thickness of the investigated volume increases, it can be observed that the spatial separation between the focal points blurs, especially for the separation of intermediate and far focus and the ray extensions at the outer focus areas become more visible. In addition, more structures appear in the vicinity of the optical axis. These are especially present around the intermediate focus and can be attributed to halos which are generated at each focal point by the out-of-focus energy of other focal points [37] and lead generally to a reduction of visual acuity at the specific distance [38].

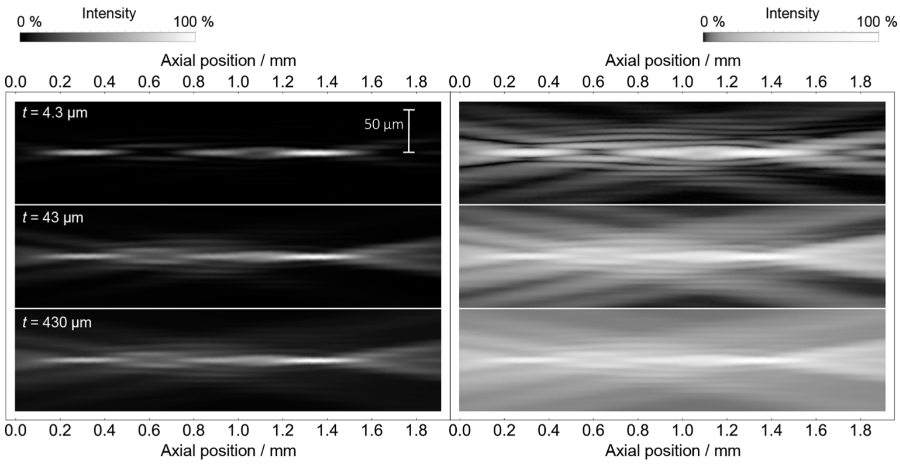

Fig. 3. Influence of the different light sheet width t on the cross-sectional image of the investigated trifocal IOL in intensity-dependent gray values with (left) linearly- and (right) logarithmically scaled intensities for an illuminated IOL-diameter $d_{\mathrm{IOL}} = 2.93$ mm. The near focus is at an axial position of ≈ 0.3 mm, the intermediate focus at ≈ 0.9 mm and the far focus at ≈ 1.35 mm.

Due to the logarithmic visual sensitivity of the eye [39] and the lack of possibilities to present high dynamic range content on low dynamic range media, the CSIs just presented are also shown in logarithmically scaled intensities on the right side of Fig. 3. The comparison of the linearly and logarithmically scaled CSIs averaged over 4.3 µm shows that the transition of the intermediate and far focus is fluent in the logarithmically scaled illustration but fine structures of low intensity

Biomedical Optics EXPRESS

appear over the whole image area. In addition to the three focal points, another focal point appears in this illustration at an axial distance of 1.9 mm. Assuming positive diffraction order numbers for the wanted diffraction orders, this focal point may be attributed to a negative diffraction order [40,41]. Starting from the optical axis, there are alternating bright and dark stripes in the lateral image areas, which are due to interference effects between the individual light beams from the different zones of the MIOL. Fine structure visibility terms hereafter the visibility and separation of ray extensions, halos, ray patterns, and additional focal points.

By applying the light sheet-based method the selected image area is accumulated line by line without considering the rotationally symmetric shape of the 3D-PSF of the investigated MIOL. Consequently, with increasing t the fine structures are overlapped by the accumulated intensity, further the background signal intensity from outer regions of the 3D-PSF increases, which all result in a lack of fine structure visibility.

To ensure comparability with documented CSIs acquired with fluorescein baths, the width $t = 43\,\mu m$ is used for calculating the CSIs of the light sheet-based method in the following. Moreover, the trimming and linear stretching of the lateral image area perpendicular to the axial position of the CSIs to three times of the original width is maintained.

3.2. Methods for image quality enhancement of 3D-PSF cross-sectional images

The optical bench allows the image recording of the 2D-PSFs and the corresponding background images for several axial positions, which each can be averaged over multiple exposures for an improved SNR. The influence of averaging and background signal correction was studied using the investigations of the aperture configuration $d_A = 3$ mm. An image stack with six images and six background images for each axial position was captured. For 4(a), only the first image per position was used. For 4(b), the first background image was subtracted. For 4(c), the six 2D-PSF images and six background images were each subtracted and averaged from each other. The corresponding cross-sectional images were calculated using the light sheet-based method. For 4(d), the averaged and subtracted images were evaluated with the new algorithm. The respective CSIs are shown in linearly scaled intensities in Fig. 4(a)-(d) and logarithmically scaled intensities in Fig. 4(e)-(h). In each CSI, the near focus is located at an axial position of ≈ 0.3 mm, the intermediate focus at ≈ 0.9 mm and the far focus at ≈ 1.35 mm. A clear separation of the near and intermediate focus can be seen. Further, low-intensity ray extensions are seen focusing and defocusing to various point positions along the optical axis. At the various focal points, especially at the intermediate focus, halos appear in the outer image areas.

The comparison of three CSIs presented in Fig. 4(a)-(c) shows no differences in shape, contrast, or intensity. Moreover, intensity is clearly visible in the defocus zone between the intermediate and far focus. Consequently, the exact separation of these two focal points is not possible. The influence of the background correction and the averaging is not visible in the linear illustration but becomes apparent in the logarithmically scaled intensities comparing Fig. 4(e)-(g). The background signal is emphasized by comparing Fig. 4(e) and Fig. 4(f) and looks like a gray shroud lying over the CSI. The influence of averaging is not as obvious as the background correction but becomes visible comparing the gray values in the outer image areas in the logarithmically scaled illustrations (see Fig. 4(f) and Fig. 4(g)). For the case of background correction and averaging, the rotationally averaged cross-sectional image (RA-CSI) was also calculated (see Fig. 4(d)). Fig. 4(d) shows clearly the three focal areas in the linear scaled RA-CSI of the new method are clearly separable (see Fig. 4(d)). Unlike the CSI of the light sheet-based method, there is no intensity in the defocus regions along the optical axis. The ray extensions at the outer focal areas can be seen in the linear illustration but are less prominent as in the light sheet-based method. In addition, some fine features can not be seen in the outer image areas like in Fig. 4(c) and 4(g) e.g. at 0.8 mm and near the lateral edges. Comparing the logarithmically scaled representations (see Fig. 4(e) - 4(h)), only the CSI of the new method reveals the three distinct focal points. Further,

Biomedical Optics EXPRESS

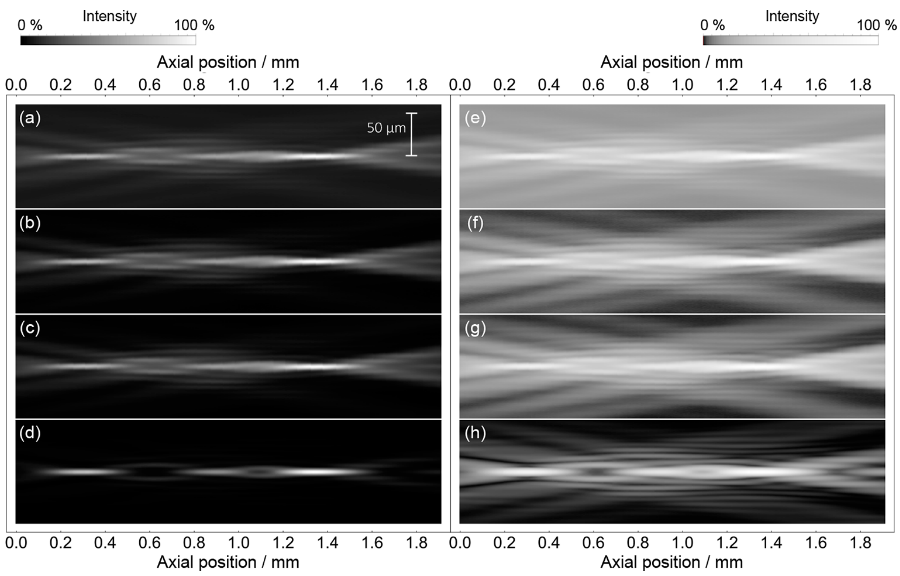

Fig. 4. CSIs determined from different image stacks captured with $d_{IOL} = 2.93$ mm: (a), (e) one captured picture for each axial position without background signal corrected and (b), (f) - with background signal corrected, (c), (g) six times averaged and background signal corrected, all calculated with the light sheet-based method with the width $t = 43$ µm, and (d), (h) averaged, and background signal corrected, and calculated using the new algorithm. The CSIs were each normalized to the maximum gray level of the four CSIs shown and are thus directly comparable. Further, these are shown in intensity-dependent gray values linearly and in logarithmically scaled intensities in the left and right column, respectively. The near focus is at the axial position of ≈ 0.3 mm, the intermediate focus at ≈ 0.9 mm and the far focus at ≈ 1.35 mm.

the individual ray pattern and halos are most evident in Fig. 4(g). It is worth noting that Fig. 4(g) reveals another focal point at an axial position of 1.9 mm. However, this has no relevance from the patient's point of view since this position lies behind the retina. The qualitative comparison of these illustrations shows that CSIs of the new method demonstrates a better fine feature visibility.

The signal-to-noise ratio (SNR) is an important and widely used quantity to study the influence of the different steps on the image quality improvement and is therefore also an important measurement to compare the quality of the captured signals. The axial positions of the focal points and the corresponding 2D-PSF images were determined by analyzing the intensity response along the optical axis and the respective 2D-PSF images of the different focal points extracted from the different image stacks and investigation methods (light sheet-based and new). The SNR values were calculated for the focal point images using the Eq. 2. For each of the four CSIs shown in Fig. 4, the respective SNR was calculated using Eq. 2 and the previously calculated largest values for A_S, σ_N, and A_N of the 2D-PSF images associated with a CSI.

Table 1 presents the calculated SNR values. The comparison reveals, that the background correction increases the SNR values of the single images of focal points by ≈ 26 % and of the CSI by ≈ 33 %. The image averaging increases the SNR of the single pictures on average by a factor ≈ 2.30 and for the CSI by a factor ≈ 2.49. With the new algorithm, the SNRs of the RA-CSIs and the images of the focal points are increased by roughly two orders of magnitude. Both Fig. 4 and the SNR-values show the impact of the new algorithm on the improvement of the image quality and the fine feature visibility. The newly developed method may give a deeper insight into the

Biomedical Optics EXPRESS

experimental image formation. To study this in more detail, we use the light sheet-based and the newly developed method to calculate CSIs and RA-CSIs of image stacks captured with different pupil sizes hereinafter.

Table 1. The calculated SNR values of the CSIs shown in Fig. 4 by using Eq. (2). Further, the SNR of the image of the near, intermediate, and far focus, respectively, were calculated for the different combinations of the methods (light sheet-based and new annulus integration), averaging (AV), and background correction (BG).

Specification			SNR			
Method	BG	AV	Near	Intermediate	Far	CSI
Light sheet-based	-	-	616	349	917	867
Light sheet-based	+	-	796	435	1144	1130
Light sheet-based	+	+	1906	811	3013	2810
Annulus integration	+	+	214 000	99 600	318 000	222 000

3.3. Cross-sectional images depending on the illuminated intraocular lens diameter

The previous chapter showed that the new method for determining the cross-sectional images results in improved image quality. To obtain a deeper understanding of the image formation of the investigated MIOL and to compare the two methods for determining the CSIs in more detail, we study the CSIs depending on the illuminated IOL-diameter d_{IOL} ranging from 2.44 mm to 5.87 mm in 0.49 mm steps, according to 2.5 mm to 6.0 mm using Eq. (1). The proprietary algorithm was used for data processing and for determining the CSIs.

Fig. 5 shows the cross-sectional images calculated with the light sheet-based (left column) and the newly developed method (right column) for several illuminated IOL-diameters d_{IOL} in logarithmically scaled intensities. The CSIs of each column were normalized to the maximum gray level. The position of the near focus is at an axial position of ≈ 0.3 - 0.4 mm, of the intermediate focus at ≈ 0.9 mm and of the far focus between ≈ 1.35 - 1.55 mm. In each of the CSIs of both methods, the near focus is clearly separated in contrast to intermediate and far focus. For d_{IOL} of 2.44 mm, the intermediate and far focus overlap. As the d_{IOL} increases, the intermediate and far focus become increasingly separated.

For $d_{\text{IOL}} \geq 4.4$ mm, the defocus zone of intermediate and far focus (axial position = 1.0 – 1.2 mm) shows the appearance of an additional focal point with very weak intensity, which becomes clearly visible with increasing d_{IOL}. In addition for $d_{\text{IOL}} \geq 4.89$ mm, a smearing of the three main focal points towards higher values of axial distances is observed. Other details that become visible only in the RA-CSI at d_{IOL} 5.38 mm and 5.87 mm are occurring interference effects along the individual ray extensions and halos in the outer image areas starting from the optical axis.

The comparison with the CSIs of the light sheet-based method (see the left column in Fig. 5) shows that all the observed extra focal points along the optical axis in the RA-CSIs of the new method are not detectable in these CSIs. The smearing of the focal points and the separation of the halos, however, is noticeable to some extent. In the RA-CSIs of the new method (see the right column in Fig. 5.) an additional focal point is visible at 1.9 mm for d_{IOL} from 2.93 mm to 3.91 mm. For larger pupil diameters, this one may shift to axial positions outside the image area shown. The observed additional focal points may be traced back to higher diffraction orders because of the diffractive character of the investigated IOL [14,40]. Due to their low intensity, these are overlaid by off-axis intensities due to the thickness of the virtual light sheet in the light sheet-based method.

To investigate the distribution of intensity along the optical axis in more detail, the through-focus curves were determined for the illuminated diameters 2.93 mm, 4.40 mm, and 5.87 mm by

Biomedical Optics EXPRESS

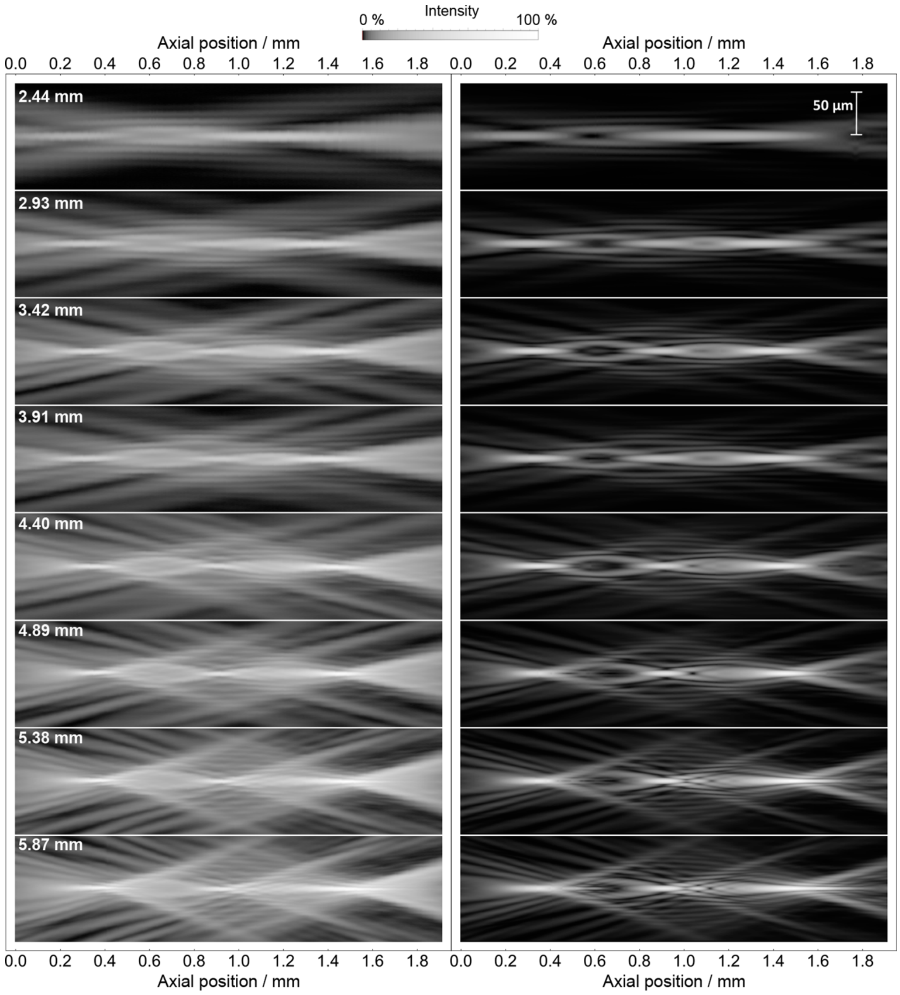

Fig. 5. Cross-sectional images calculated (left) with the light sheet-based and (right) the newly developed method depending on the illuminated IOL-diameter d_{IOL} (denoted in the upper left corner of each row) in logarithmically scaled intensity-depended gray values. The near focus is at the axial position of ≈ 0.3 mm - 0.4 mm, the intermediate focus at ≈ 0.9 mm and the far focus at ≈ 1.35 - 1.45 mm.

calculating the mean intensity of an 11×11 pixel centered to the optical axis for each captured image.

Fig. 6 shows the through-focus curve of $d_{IOL} = 2.93$ mm illustrated as –●–, $d_{IOL} = 4.40$ mm as –▲–, and $d_{IOL} = 5.87$ mm as –■–. The near focus is located in the axial position range between 0.3 mm and 0.4 mm, the intermediate focus at ≈ 0.9 mm, and the far focus between 1.35 mm and 1.55 mm. With increasing pupil size, the intensity in the focal points increases, and the additional peaks, as seen in Fig. 5, between the axial distance of 1.0 - 1.2 mm become visible. Interestingly, for $d_{IOL} = 5.87$ mm, a shoulder appears on the right side of the near- and far focus, which is most likely due to underlying peaks from a higher diffraction order. Additionally, the position of the near and the far focus shift to higher axial positions with increasing pupil sizes.

Biomedical Optics EXPRESS

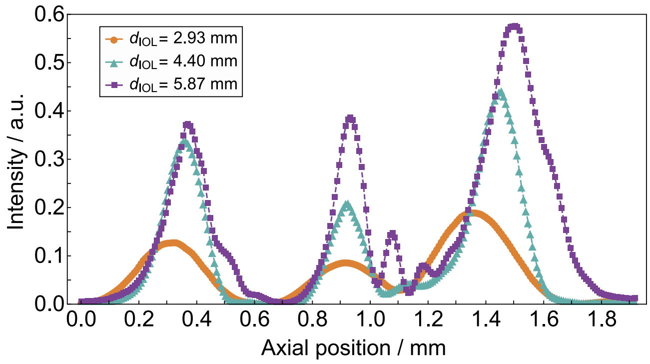

Fig. 6. Through-focus response as a function of the axial position for the illuminated IOL-diameters d_{IOL} 2.93 mm, 4.40 mm, and 5.87 mm.

4. Discussion

Our study has shown that the implementation of the new proprietary algorithm exploiting the rotational symmetry of IOLs has the advantage of image quality improvement of the corresponding cross-sectional images compared to the light sheet-based method. With regard to the light sheet-based method, we found that the smaller the thickness of the virtual light sheet the better image quality and fine feature visibility of the illustration of the cross-sectional images is.

Petelczyc et al. [17] reported a projection cross-sectional image of the AT LISA tri 839MP (Carl Zeiss Meditec AG, Jena, Germany) for a pupil size $d_A = 3$ mm, which is consistent with our findings and shows similarities in the distance between the focal points, higher gray values in the defocus zone between intermediate and far focus. Due to its different aspect ratio, halos and ray extensions are not as obvious as in the CSIs presented in Fig. 3. The greater SNR-values of the newly developed method are an indicator for image quality improvement.

The comparison of the CSIs quality and the SNR-values of the light sheet-based and the newly developed method clearly shows that an improvement of the CSI image quality and the fine feature visibility is achieved fulfilled by the newly developed algorithm. Furthermore, the individual fine structures like high diffraction orders, which have to be present in the case of a diffractive IOL, are clearly visible in a CSI for the first time. Accordingly, the extra focal points occurring between the intermediate and the far focus for $d_{IOL} \geq 4.4$ mm raise two questions that could be the subject of future experimental investigations and clinical trials. Do these focal points improve the visual acuity in the intermediate and far distance? Accordingly, does the investigated IOL have an EDOF-character (Extended Depth of Focus [42]) in the range of the intermediate to the distant focus for $d_{IOL} \geq 4.4$ mm?

We observed an overlap between the intermediate and far focus in the CSIs and the RA-CSIs for $d_A = 2.5$ mm. Consistent with our findings Vega et al. [43] reported that, based on the depth of field of a gaussian beam, the smaller the entrance pupil the longer the extension of the focus spot along the optical axis is, which lead to overlap between different focal point areas of MIOLs. In general, the calculation of the modulation transfer function (MTF) is often preferred, which is the quantity is the squared magnitude of the PSF, and easily and quickly accessible due to the fast Fourier transform [26]. Ruiz-Alcocer et al. investigated pupil size dependent through-focus modulation transfer function of the same IOL under investigation [44]. In accordance with our results, they observed only a peak for the near and far focus without an intermediate peak for $d_A < 3.0$ mm. Consequently, the overlapping of the intermediate- and far focus is due to the properties of the studied IOL.

Biomedical Optics EXPRESS

In contrast to the newly developed method, the beam profiles of the light sheet-based methods show a very intense ray pattern even apart from the optical axis [17,19–21]. However, comparing to the newly developed method, which does not exhibit all of these off-axis light features, it evidently shows that methods based on light sheets of certain width give potentially misleading or even wrong results. Further, with our method we find an additional focal point behind the far focus, which may be attributed to a diffraction order of opposite sign compared to the diffraction orders of intermediate and near focus.

In the case of applying a fluorescein bath or an optical bench for the light sheet-based method, three critical thoughts should be mentioned. Firstly, the wider the light sheet, the more intensity is included from the image regions laterally distant from the optical axis, resulting in deviating cross-sectional images. Based on the fact that in the case of the fluorescein bath the beam profile is recorded by a side-mounted camera that captures an image averaged over the illuminated light sheet width, increasing the width of the illuminated light sheet would not result in any improvement in image quality. Secondly, it must be taken into account that fluorescence is based on a preceding absorption and hence the intensity along the optical axis may decrease. Stating this, it is not possible to guarantee, that a through-focus curve obtained from this method describes the intensity distribution along the optical axis correctly. This fact has not been studied till now. Thirdly, the image quality is usually reduced due to image artifacts resulting from the scattering dust of the used particles [19,20]. These critical problems are avoided by the approach of an optical bench in combination with the new algorithm.

Furthermore, axial smearing of the focal points was observed for the RA-CSIs in Fig. 5. The investigated MIOL has a spherical aberration (SA) of -0.18 µm for a 6.0 mm eye pupil to partially compensate a part of the natural positive SA of the human eye [45]. The observed smearing along the optical axis towards larger values of the axial position implies that the interaction between the SA of the model cornea and the MIOL creates a negative SA.

The through-focus curves show like the previous RA-CSIs higher diffraction orders and further an obvious drifting of the near and far focus to larger values of the axial position. Thus, the smearing may also be caused by superpositions of the main focus with a peak of a higher diffraction order, which is important especially for large pupils. This should be investigated in further research projects. The proprietary algorithm was developed for rotationally symmetric IOLs like monofocal and most multifocal diffractive IOLs. In addition to these IOLs, other MIOL design approaches exist that are based e.g. on the light sword method [17] or the combination of different refractive elements [46]. Due to their consequently asymmetric 3D-PSF, the application of the new algorithm will produce inaccurate CSIs leading to misinterpretations and wrong conclusions about the investigated IOLs. Recent IOL-designs compensating the aberrations induced by imaging at the kappa angle [47] are not rotationally asymmetric, however, their 3D-PSF should be symmetric, if the model eye is appropriately rotated around the nodal point. Hence, such IOLs could be evaluated using the newly developed method.

A drawback of the new algorithm is the long calculation time of the algorithm $t_C \approx 40$ min. The time consuming part of the algorithm originated from the fourfold increased edge length of the images using cubic-spline interpolation (38 % of t_C) and the annulus integration method (48 % of t_C). Accordingly, each image is increased from 3088×2076 pixels to 12352×8304 pixels. The application of another software such as Python, e.g. using SciPy [48], Matlab (The MathWorks Inc., Massachusetts, USA), or more efficient image processing algorithms of Mathematica (The Wolfram Centre, Oxfordshire, United Kingdom) may reduce the high calculation time. Other approaches may also include the parallel evaluation of graphic cards using CUDA [49] or OpenCL [50].

However, CSIs are widely used to understand the functional principles of different IOLs. The combination of an optical bench and the newly developed evaluation method allows a precise determination of the cross-sectional images of rotationally symmetric IOLs.

5. Conclusion

This work compares different post-processing approaches for improving the quality of CSIs of IOLs, which are tested exemplifying on own captured 3D-PSFs of the AT LISA tri 839MP (Carl Zeiss Meditec AG, Jena, Germany). Further CSIs of the investigated IOL are presented for eight different pupil diameters by using two different visualization methods, the light sheet-based and the newly developed method, which for the first time specifically exploits the rotational symmetry of most IOLs like the AT LISA tri 839MP (Carl Zeiss Meditec AG, Jena, Germany).

The comparative study showed the clear superiority of the newly developed method in terms of image quality and signal-to-noise ratios compared to the light sheet based method. In addition, fine structures of the investigated MIOL like higher diffraction orders become visible in the CSIs of the newly developed method. Moreover, the off-axis intensities, e.g. halos, are now distinguishable with higher contrast and therefore easy to identify compared to other methods. The new algorithm will allow a better understanding of the character of the real experimental image formation induced by IOLs, which was previously limited using the light-sheet based method due to technical restrictions.

It is subject to future research, to extend the newly developed method to the determination of important optical properties of IOLs such as energy efficiency, modulation transfer function, or longitudinal chromatic aberration.

Funding. Deutsche Forschungsgemeinschaft (STA 543/9-1).

Acknowledgments. The authors thank Carl Zeiss Meditec AG for their support as part of a cooperation agreement and Mario Gerlach and Friedrich Kirchner (both Carl Zeiss Meditec AG) for scientific discussions.

Disclosures. The authors declare no conflicts of interest.

Data availability. Data underlying the results presented in this paper are not publicly available at this time but may be obtained from the authors upon reasonable request.

References

1. S. Modi, R. Lehmann, A. Maxwell, K. Solomon, R. Cionni, V. Thompson, J. Horn, M. Caplan, B. Fisher, J. G. Hu, and E. Yeu, "Visual and patient-reported outcomes of a diffractive trifocal intraocular lens compared with those of a monofocal intraocular lens," Ophthalmology **128**(2), 197–207 (2021).
2. J. A. Davison and M. J. Simpson, "History and development of the apodized diffractive intraocular lens," J. Cataract Refractive Surg. **32**(5), 849–858 (2006).
3. G. Auffarth, T. Rabsilber, T. Kohnen, and M. Holzer, "Design and optical principles of multifocal lenses," Ophthalmologe **105**(6), 522–526 (2008).
4. L. C. Salerno, M. C. Tiveron, and J. L. Alió, "Multifocal intraocular lenses: types, outcomes, complications and how to solve them," Taiwan J. Ophthalmol. **7**(4), 179 (2017).
5. V. Maurino, B. D. Allan, G. S. Rubin, C. Bunce, W. Xing, and O. Findl, "Quality of vision after bilateral multifocal intraocular lens implantation," Ophthalmology **122**(4), 700–710 (2015).
6. M. J. Simpson, "Diffractive multifocal intraocular lens image quality," Appl. Opt. **31**(19), 3621 (1992).
7. L. Carretero, C. González, A. Fimia, and I. Pascual, "Application of the ronchi test to intraocular lenses: A comparison of theoretical and measured results," Appl. Opt. **32**(22), 4132 (1993).
8. G. Bos, J.-M. Vanzo, J. Maufoy, and J. L. Gutzwiller, "New interferometric method to assess intraocular lens characteristics," Proc. SPIE **2127**, 56 (1994).
9. G. Ravalico, F. Parentin, P. Sirotti, and F. Baccara, "Analysis of light energy distribution by multifocal intraocular lenses through an experimental optical model," J. Cataract Refractive Surg. **24**(5), 647–652 (1998).
10. I. O. for Standardization, "ISO11979-2:2000-07 ophthalmic implants – intraocular lenses – part 2: optical properties and test methods," (2000).
11. E. Peli and A. Lang, "Appearance of images through a multifocal intraocular lens," J. Opt. Soc. Am. A **18**(2), 302 (2001).
12. F. Castignoles, M. Flury, and T. Lepine, "Comparison of the efficiency, MTF and chromatic properties of four diffractive bifocal intraocular lens designs," Opt. Express **18**(5), 5245 (2010).
13. T. Kawamorita and H. Uozato, "Modulation transfer function and pupil size in multifocal and monofocal intraocular lenses in vitro," J. Cataract Refractive Surg. **31**(12), 2379–2385 (2005).
14. W. Hill, D. Carson, X. Hong, and M. Karakelle, "Optical bench performance of AcrySof IQ ReSTOR, AT LISA tri, and FineVision intraocular lenses," Clin. Ophthalmol. **8**, 2105–2113 (2014).
15. S. Lee, M. Choi, Z. Xu, Z. Zhao, E. Alexander, and Y. Liu, "Optical bench performance of a novel trifocal intraocular lens compared with a multifocal intraocular lens," Clin. Ophthalmol. **10**, 1031–1038 (2016).

16. M. S. Millán and F. Vega, "Through-focus energy efficiency and longitudinal chromatic aberration of three presbyopia-correcting intraocular lenses," Trans. Vis. Sci. Tech. **9**(12), 13 (2020).
17. K. Petelczyc, A. Kolodziejczyk, N. Błocki, A. Byszewska, Z. Jaroszewicz, K. Kakarenko, K. Kołacz, M. Miler, A. Mira-Agudelo, W. Torres-Sepúlveda, and M. Rkekas, "Model of the light sword intraocular lens: in-vitro comparative studies," Biomed. Opt. Express **11**(1), 40 (2020).
18. S. Reiß, J. Forbrig, R. Guthoff, T. Terwee, H. Stolz, S. Siewert, A. El-Tamer, U. Hinze, B. Chichkov, and O. Stachs, "Optimisation of the visualisation technique for optical paths through intraocular lenses for characterisation of multifocal imaging properties of fresnel-zone plates," Klin. Monatsbl. Augenheilkd. **231**, 1183–1186 (2014).
19. H. Weeber, T. Terwee, M. van der Mooren, and P. Piers, "Visualization of the retinal image in an eye model with spherical and aspheric, diffractive, and refractive multifocal intraocular lenses," J. Cataract Refractive Surg. **24**(3), 223–232 (2008).
20. T. Eppig, K. Rubly, A. Rawer, and A. Langenbucher, "Visualization of light propagation with multifocal intraocular lenses using the ouzo effect," BioMed Res. Int. **2019**, 1–10 (2019).
21. H.-S. Son, G. Łabuz, R. Khoramnia, T. M. Yildirim, C. Y. Choi, M. C. Knorz, and G. U. Auffarth, "Visualization of forward light scatter in opacified intraocular lenses and straylight assessment," Diagnostics **11**(8), 1512 (2021).
22. U. Hinze, A. El-Tamer, L. L. Doskolovich, E. A. Bezus, S. Reiß, H. Stolz, R. F. Guthoff, O. Stachs, and B. Chichkov, "Additive manufacturing of a trifocal diffractive-refractive lens," Opt. Commun. **372**, 235–240 (2016).
23. H. S. Son, G. Labuz, R. Khoramnia, P. Merz, T. M. Yildirim, and G. U. Auffarth, "Ray propagation imaging and optical quality evaluation of different intraocular lens models," PLoS One **15**(5), e0233829 (2020).
24. H.-S. Son, G. Łabuz, R. Khoramnia, T. M. Yildirim, and G. U. Auffarth, "Laboratory analysis and ray visualization of diffractive optics with enhanced intermediate vision," BMC Ophthalmol. **21**(1), 197 (2021).
25. I. O. for Standardization, "ISO11979-2:2014-2 ophthalmic implants – intraocular lenses – part 2: Optical properties and test methods," (2014).
26. R. Rawer, W. Stork, C. W. Spraul, and C. Lingenfelder, "Imaging quality of intraocular lenses," J. Cataract Refractive Surg. **31**(8), 1618–1631 (2005).
27. F. Alba-Bueno, F. Vega, and M. S. Millán, "Design of a test bench for intraocular lens optical characterization," J. Phys.: Conf. Ser. **274**(1), 012105 (2011).
28. S. Wahl, C. Song, and A. Ohlendorf, "Comparison of two devices to simulate vision with intraocular lenses," Clin. Ophthalmol. **13**, 123–130 (2019).
29. M. Gerlach, R. Guthoff, O. Stachs, S. Bohn, and K. Sperlich, "Pre-clinical evaluation of intraocular lenses through simulated implantation," Klin Monatsbl Augenheilkd **235**, 1332–1341 (2018).
30. J. Pujol, M. Aldaba, A. Giner, J. Arasa, and S. O. Luque, "Visual performance evaluation of a new multifocal intraocular lens design before surgery," Invest Ophthalmol Vis Sci. **55**, 3752 (2014).
31. M. K. Cheezum, W. F. Walker, and W. H. Guilford, "Quantitative comparison of algorithms for tracking single fluorescent particles," Biophys. J. **81**(4), 2378–2388 (2001).
32. B. Shuang, J. Chen, L. Kisley, and C. F. Landes, "Troika of single particle tracking programing: SNR enhancement, particle identification, and mapping," Phys. Chem. Chem. Phys. **16**(2), 624–634 (2014).
33. A. B. Watson and J. I. Yellott, "A unified formula for light-adapted pupil size," J. Vis. **12**(10), 12 (2012).
34. K. Dumbleton, M. Guillon, P. Theodoratos, C. Wooley, and K. Moody, "The effect of age and refractive error on pupil size," Invest. Ophthalmol. Vis. Sci. **56**, 585 (2015).
35. I. S. IDS Imagaging Development Systems GmbH, "Emva1288-ui-3880cp-m-gl-r2-default-settings," (2017).
36. S. Hecht, "Intensity and the process of photoreception," J. Gen. Physiol. **2**(4), 337–347 (1920).
37. S. Pieh, B. Lackner, G. Hanselmayer, R. Zöhrer, M. Sticker, H. Weghaupt, A. Fercher, and C. Skorpik, "Halo size under distance and near conditions in refractive multifocal intraocular lenses," Br. J. Ophthalmol. **85**(7), 816–821 (2001).
38. F. Vega, F. Alba-Bueno, M. S. Millán, C. Varón, M. A. Gil, and J. A. Buil, "Halo and through-focus performance of four diffractive multifocal intraocular lenses," Invest. Ophthalmol. Visual Sci. **56**(6), 3967–3975 (2015).
39. M. Ramamurthy and V. Lakshminarayanan, "Human vision and perception," in *Handbook of Advanced Lighting Technology*, R. Karlicek, C.-C. Sun, G. Zissis, and R. Ma, eds. (Springer International Publishing, 2015).
40. D. Gatinel, C. Pagnoulle, Y. Houbrechts, and L. Gobin, "Design and qualification of a diffractive trifocal optical profile for intraocular lenses," J. Cataract Refractive Surg. **37**(11), 2060–2067 (2011).
41. J. A. Futhey, "Diffractive bifocal intraocular lens," Proc. SPIE **1052**, 142–149 (1989).
42. J. F. Zapata-Díaz, M. A. Rodríguez-Izquierdo, N. Ould-Amer, J. Lajara-Blesa, and N. López-Gil, "Total depth of focus of five premium multifocal intraocular lenses," J. Cataract Refractive Surg. **36**(9), 578–584 (2020).
43. F. Vega, F. Alba-Bueno, and M. S. Millán, "Energy efficiency of a new trifocal intraocular lens," J. Eur. Opt. Soc. Rapid Publ. **9**, 14002 (2014).
44. J. Ruiz-Alcocer, D. Madrid-Costa, S. García-Lázaro, T. Ferrer-Blasco, and R. Montés-Micó, "Optical performance of two new trifocal intraocular lenses: through-focus modulation transfer function and influence of pupil size," Clin. & Exp. Ophthalmol. **42**(3), 271–276 (2014).
45. J. F. Montin, "Achieving spectacle independence with the AT LISA tri 839mp," Cataract. & Refract. Surg. Today Eur. **3**, 1 (2012).

Biomedical Optics EXPRESS

46. J. L. Alio, A. B. Plaza-Puche, J. Javaloy, M. J. Ayala, L. J. Moreno, and D. P. Piñero, "Comparison of a new refractive multifocal intraocular lens with an inferior segmental near add and a diffractive multifocal intraocular lens," Ophthalmology **119**(3), 555–563 (2012).
47. B. Chassagne and L. Canioni, "Analytical solution of a personalized intraocular lens design for the correction of spherical aberration and coma of a pseudophakic eye," Biomed. Opt. Express **11**(2), 850 (2020).
48. P. Virtanen, R. Gommers, T. E. Oliphant, M. Haberland, T. Reddy, D. Cournapeau, E. Burovski, P. Peterson, W. Weckesser, J. Bright, S. J. van der Walt, M. Brett, J. Wilson, K. J. Millman, N. Mayorov, A. R. J. Nelson, E. Jones, R. Kern, E. Larson, C. J. Carey, İ. Polat, Y. Feng, E. W. Moore, J. VanderPlas, D. Laxalde, J. Perktold, R. Cimrman, I. Henriksen, E. A. Quintero, C. R. Harris, A. M. Archibald, A. H. Ribeiro, F. Pedregosa, and P. van Mulbregt, "SciPy 1.0: fundamental algorithms for scientific computing in Python," Nat. Methods **17**(3), 261–272 (2020).
49. NVIDIA, P. Vingelmann and F. H. Fitzek, "Cuda, release: 10.2.89," (2020).
50. G. Bradski, "The OpenCV Library," Dr. Dobb's J. Softw. Tools (2000).

92.76.202.137 {ts '2022-04-06 09:02:29'}

The Rostock Method for Qualitative and Quantitative Evaluation of Intraocular Lenses

Die Rostocker Methode zur qualitativen und quantitativen Bewertung von Intraokularlinsen

Authors

Ricardo Elsner[1,2], Jan Sievers[3], Martin Kunert[4], Stefan Reiss[5], Sebastian Bohn[1,2], Melanie Schünemann[1,2], Heinrich Stolz[6], Rudolf Guthoff[1,2], Oliver Stachs[1,2], Karsten Sperlich[1,2]

Affiliations

1 Klinik und Poliklinik für Augenheilkunde, Universitätsmedizin Rostock, Deutschland
2 Interdisziplinäre Fakultät Leben, Licht & Materie, Universität Rostock, Deutschland
3 Institut für Physik, Martin-Luther-Universität Halle-Wittenberg, Halle, Deutschland
4 Klinik für Augenheilkunde, Dietrich-Bonhoeffer-Klinikum Neubrandenburg, Deutschland
5 Labor für Sehhilfen – Bereich Optik und Technik der Brille, Berliner Hochschule für Technik, Berlin, Deutschland
6 Institut für Physik, Universität Rostock, Deutschland

Key words

IOL, optic bench, fluorescein, image processing algorithm, cross-sectional images, 3-D point spread function

Schlüsselwörter

IOL, optische Bank, Fluorescein, Bildverarbeitungsalgorithmus, Querschnittsbilder, 3-D-Punktspreizfunktion

received 1.6.2022
accepted 29.9.2022

Bibliography

Klin Monatsbl Augenheilkd 2022; 239: 1440–1446
DOI 10.1055/a-1953-7302
ISSN 0023-2165
© 2022. Thieme. All rights reserved.
Georg Thieme Verlag KG, Rüdigerstraße 14, 70469 Stuttgart, Germany

Correspondence

Ricardo Elsner
Klinik und Poliklinik für Augenheilkunde, Universitätsmedizin Rostock
Doberaner Str. 140, 18057 Rostock, Deutschland
Phone: + 49 (0) 38 14 94 85 01, Fax: + 49 (0) 38 14 94 85 02
elsner.ricardo@googlemail.com

ABSTRACT

Background For quantitative and qualitative evaluation of the imaging properties of IOLs, axial cross-sectional images can be obtained from the 3-dimensional light distribution by means of an optical bench, as is known from light sheet recordings in fluorescein baths. This paper presents a new image-processing algorithm to enhance the quality of generated axial cross-sectional images, and the two methods are then compared.

Material and Methods The 3-dimensional point spread function of a diffractive trifocal IOL (AT LISA tri 839MP, Carl Zeiss Meditec AG, Jena, Germany) was recorded on an optical bench developed in Rostock for different pupil diameters. A specially adapted image processing algorithm was then applied to the measurements, allowing through-focus curves to be generated. In addition, cross-sectional images of the IOLs studied were acquired using the light sheet method in a fluorescein bath.

Results The study clearly shows the superiority of the newly developed method over the light sheet method in terms of image quality. In addition to the individual focal points, fine focal structures as well as halos can be made visible in the cross-sectional images obtained using the new method. In the generated through-focus curves, 3 intensity peaks can be identified, which represent the near, intermediate and far focus of the tested MIOL and cannot be represented by light sheet methods.

Conclusion The interaction of the optical bench with the developed image processing algorithm allows a more detailed understanding of the image formation and false light phenomena of IOLs, which was restricted by the technical limitations of the existing light sheet method. In addition, other quantities such as the through-focus curve can be derived quantitatively.

ZUSAMMENFASSUNG

Hintergrund Zur quantitativen und qualitativen Bewertung der Abbildungseigenschaften von IOLs können mittels einer optischen Bank axiale Querschnittsbilder aus der 3-dimensio-

Heruntergeladen von: Ricardo Elsner, Universität Rostock. Urheberrechtlich geschützt.

nalen Lichtverteilung erstellt werden, wie sie von Lichtblattaufnahmen in Fluoresceinbädern bekannt sind. In dieser Arbeit wird ein neuer Bildverarbeitungsalgorithmus zur Verbesserung der Qualität solcher generierten axialen Querschnittsbilder vorgestellt und beide Methoden werden miteinander verglichen.

Material und Methoden Die 3-dimensionale Punktspreizfunktion einer diffraktiven trifokalen IOL (AT LISA tri 839MP, Carl Zeiss Meditec AG, Jena, Deutschland) wurde an einer in Rostock entwickelten optischen Bank für unterschiedliche Pupillendurchmesser aufgenommen. Anschließend wurde ein speziell angepasster Bildverarbeitungsalgorithmus auf die Messungen angewandt, der die Generierung von Durchfokuskurven erlaubt. Zusätzlich wurden Querschnittsbilder der untersuchten IOL unter Verwendung der Lichtblattmethode in einem Fluoresceinbad aufgenommen.

Ergebnisse Die Studie zeigt deutlich die Überlegenheit der neu entwickelten Methode in Bezug auf die Bildqualität gegenüber der Lichtblattmethode. Neben den einzelnen Fokuspunkten können in den Querschnittsbildern der neuen Methode sowohl feine Fokusstrukturen als auch Halos sichtbar gemacht werden. In den generierten Durchfokuskurven lassen sich 3 Intensitätsspitzen erkennen, die den Nah-, Intermediär- und Fernfokus der getesteten MIOL darstellen und mittels Lichtblattmethoden nicht darstellbar sind.

Schlussfolgerung Das Zusammenspiel der optischen Bank mit dem entwickelten Bildverarbeitungsalgorithmus ermöglicht ein detaillierteres Verständnis der Bildentstehung und Falschlichterscheinungen von IOLs, was mit der bisherigen Lichtblattmethode aufgrund technischer Beschränkungen nur begrenzt möglich war. Darüber hinaus lassen sich weitere Größen wie z. B. die Durchfokuskurve quantitativ ableiten.

Introduction

During cataract surgery, the native lens of the eye is removed and replaced with an intraocular lens (IOL). While patients with simple monofocal lenses [1] can only see sharply at a single distance, multifocal IOLs (MIOLs) with 2 or more focal points [2] potentially offer the possibility of being spectacle-free. The multifocality of IOLs can be realized through the principles of refraction, diffraction, or a combination of both [3, 4]. In order to verify imaging quality as well as to compare the performance of IOLs, it is essential to determine their properties experimentally. For this reason, this should be an essential part of the IOL development pipeline.

There are a number of ways to study the imaging properties of IOLs on so-called optical benches. Since the 1990s, a wide variety of approaches have been taken [5 – 8]. They have several distinctive components, such as a collimated light beam, an IOL mounted in a water-filled model eye, a camera for data acquisition, and a computer for data processing. However, many details of the respective setups differed, which often prevented a quantitative comparison of the results. The ISO 11979-2 : 2000-07 standard was introduced in 2000 to address this problem. It recommends the use of an optical bench with special technical requirements as an experimental setup for IOL examinations. On this basis, different research groups have studied MIOLs in terms of energy distribution [9], longitudinal chromatic aberration [10], and with a focus on cross-sectional imaging [11, 12].

In addition to the visualization of e.g. test images or visual signs, the point spread function (PSF) can also be recorded. In this process, a point light source is imaged onto a camera. In many cases, this image contains small distortions due to aberrations, which is why the PSF is a measure of imaging quality. Subsequently, the modulation transfer function (MTF), also a measure of imaging quality, can be calculated from the PSF, but it is more likely to provide information about detail contrast and contains less information.

Strictly speaking, however, this PSF is not just a 2-dimensional (2-D) image at the focal point perpendicular to the optical axis, but a 3-dimensional (3-D) distribution of light around the area of the focal point. While often only 2-D PSFs are recorded and evaluated, it is also possible to record these 3-D PSFs by taking multiple camera shots in the area of the focal point. From these data, sectional images along the optical axis can be calculated, which in principle correspond to the known images of the light sheet method [11, 13] and represent the beam path.

Using the light sheet method, several research groups have already determined the scattered light effects of MIOLs [14] or their optical performance for visualizing nearby objects [15]. Through-focus curves can also be calculated on the basis of fluorescein bath cross-sectional images, as Eppig et al. showed [11], but these are not capable of reproducing the intensity distribution realistically.

There is therefore a need to develop a novel approach for recording and analyzing 3-D light distributions following the introduction of an IOL. This paper presents a dedicated optical bench that allows spatial intensity distributions to be recorded after IOL placement and can be used to calculate cross-sectional images and through-focus curves using a novel image processing algorithm for rotationally symmetric IOLs. The results of the axial light distribution are compared with the light sheet method.

Materials and Methods

IOL and model corneas used

The MIOL studied was a diffractive trifocal IOL (AT LISA tri 839MP, Carl Zeiss Meditec AG, Jena, Germany) with a basic refraction for the far focus of 22.5 dpt and an addition of + 3.33 dpt for the near and + 1.66 dpt for the intermediate focus. The corneas used for the respective methods are based on the optical properties of the human cornea (refractive power and spherical aberration).

Light sheet method

In this method, a thin sheet of light illuminates the IOL, placed in a fluorescein bath, through a model cornea. The fluorescence excitation reveals the light distribution of the illuminated IOL (cf. ▶ **Fig. 1 b**). A camera positioned laterally at right angles and cen-

Heruntergeladen von: Ricardo Elsner, Universität Rostock. Urheberrechtlich geschützt.

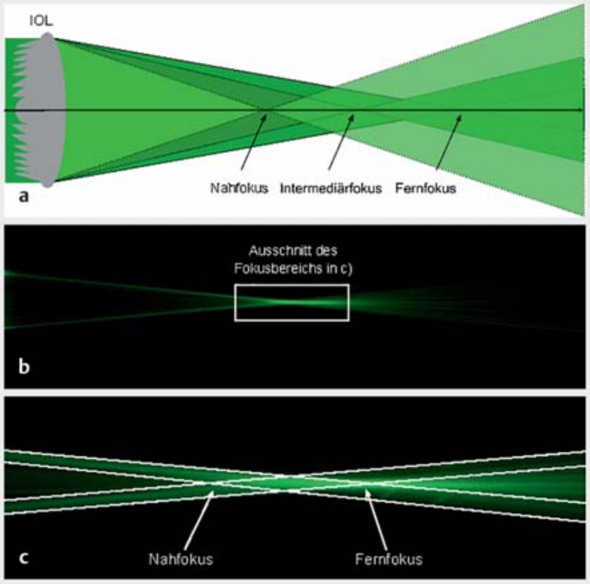

▶ **Fig. 1** Cross-sectional images of the IOL under investigation. **a** Schematic representation of the light distribution of the near, intermediate, and far focus. **b** Light distribution in a fluorescein bath recorded with a laterally positioned camera. The focal area is marked with a white rectangle, but the different foci cannot be distinguished. c Shows the magnification of the cutout area from **b**, the beam is narrowed such that the near and far focus can be differentiated, but the intermediate focus is not visible separately.

tered on the light sheet can be used to capture the light emitted by scattering and fluorescence. The intensity distribution of the cross-sectional images depends on both the thickness of the light sheet and the decentering/tilting of the IOL.

The setup used here employs a laser diode with a wavelength of 532 nm. The design of the model cornea is based on studies by Holladay and colleagues [16]. The round beam profile with a diameter of 3.5 mm was reduced 10-fold and focused with a converging lens onto a downstream Powell lens, which is used to convert from a Gaussian to a flat-top intensity line profile and ultimately generate a light sheet of thickness 0.35 mm. To collimate the divergent beam path, a cylindrical lens was placed at the end of the Powell lens. The subsequent iris diaphragm makes it possible to adjust the length of the laser line – here to 5 mm. The collimated light sheet entered the model cornea through a water bath containing fluorescein. ▶ **Fig. 1 a** shows the schematic formation of the focal points in a MIOL. The foci are located in the highlighted section of the fluorescein bath cross-sectional image in ▶ **Fig. 1 b**. The enlarged section of ▶ **Fig. 1 b** shown in ▶ **Fig. 1 c** allows the near and far focus to be visualized by tracing the course of the beam, as shown schematically in ▶ **Fig. 1 a**).

Optical bench

The optical bench developed in-house is based in principle on the concepts of other working groups and the ISO standard mentioned above. ▶ **Fig. 2** shows the schematic measurement setup. By means of an achromatic lens, green LED light (with a central wavelength of 530 nm) is collimated as it passes through a pinhole. A pupil aperture can be used to change the diameter of the parallel beam. The model eye originally developed for the VirtIOL (10Lens S. L. U., Terrassa, Spain) – a through-the-lens device for simulated implantation of IOLs [17, 18] – is integrated into the optical setup. The water-filled model eye essentially consists of 3 components. On the front side there is an artificial cornea (model cornea), on the back side a glass window and in between there is an IOL holder with the IOL to be examined. The model cornea used here is an in-house design made of PMMA, and has a refractive power of D = 43 dpt with a spherical aberration of SA = + 0.28 µm. The real image generated by the model eye is magnified by a combination of microscope objective and tube lens onto a monochrome 12-bit CMOS camera. The objective lens, tube lens and camera are mounted on a motorized sliding stage. This can be moved along the optical axis, allowing automated acquisition of multiple images of the IOL light distribution at different axial positions along the optical axis. For the analyses presented here, the total range of travel of the displacement stage is $s_G = 1.75$ mm with an increment $s_I = 7.63$ µm.

The following refers to the axial position in relation to the range of travel.

Image processing algorithm for rotationally symmetric IOLs

A proprietary algorithm written in Mathematica 12.0 (The Wolfram Centre, Oxfordshire, UK) was developed for automatic analysis of the recorded 3-D PSF. In doing so, the algorithm exploits the rotational symmetry of the 2-D PSF, which is due to the rotation-

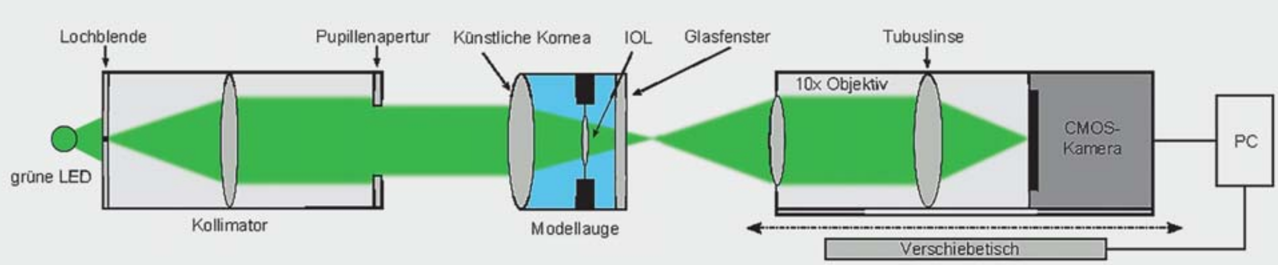

▶ **Fig. 2** Schematic structure of the optical bench for measuring the 3-dimensional point spread function of intraocular lenses. The model eye is filled with water (shown in blue).

Heruntergeladen von: Ricardo Elsner, Universität Rostock. Urheberrechtlich geschützt.

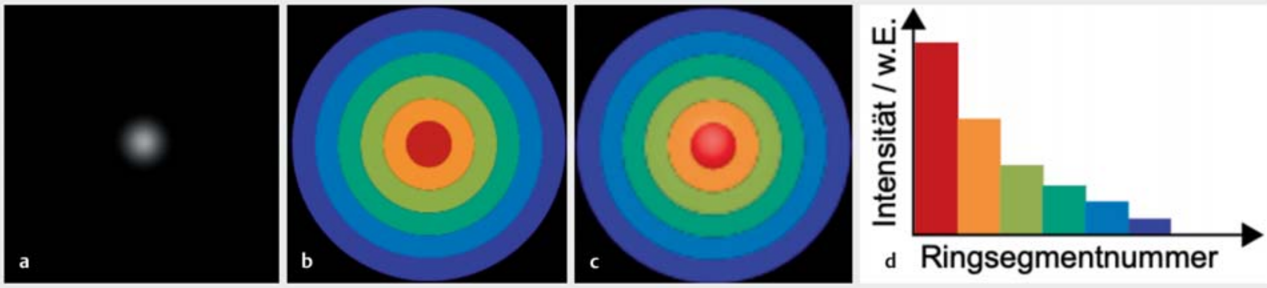

▶ **Fig. 3** Schematic overview of the determination of intensity distributions using a dedicated image processing algorithm. Over a travel distance of about 2 mm, approximately 300 single images (2-D PSFs) are acquired along the optical axis using a CMOS camera (**a**). A ring integral mask with circular rings of constant width subdivides the 2-D PSF image and determines the pixels lying in a circular ring (**b, c**). Subsequently, the intensities of the pixels for each circular ring are summed up, normalized to the respective circular ring area, and the integral over the found 2-D Gaussian function is defined as the energy in the focus (**d**).

Heruntergeladen von: Ricardo Elsner, Universität Rostock. Urheberrechtlich geschützt.

ally symmetric structure of the diffractive MIOL being studied. The basic idea of the algorithm is as follows: Each camera image is divided into many concentric circular rings having a constant width, with midpoints on the optical axis. The intensity in each ring segment is then added up and standardized by dividing it by the area of the respective segment. This creates an array of intensity values from the center to the edge for each axial position. These arrays are then combined to form an image which, due to axial symmetry, together with its mirror image on the optical axis, gives the averaged beam profile of the 3-D PSF. ▶ **Fig. 3** shows the schematic procedure for calculating the intensity distribution. Further intermediate steps are not explained here, but are published in detail in [19]. It takes about half an hour on a powerful desktop computer for the highly parallelized Mathematica algorithm to perform a complete evaluation of an image stack with 230 axial frames.

The signal-to-noise ratio (SNR), which generally indicates the ratio of the average signal power to the average noise power, is a measure of the quality of the acquired signals. The higher the value, the better the quality. Here, the SNR is the difference between the mean amplitudes of the signal and the noise divided by the variance of the noise [19].

Results

The cross-sectional images presented in ▶ **Fig. 4** show the observed light distributions of the investigated MIOL with the light sheet method (▶ **Fig. 4 a**) and the optical bench with application of the new image processing algorithm (▶ **Fig. 4 b**) at a pupil diameter (d_{IOL}) of approximately 5 mm. The cross-sectional images are presented in linearly scaled intensities. The comparison of the images in ▶ **Fig. 4** shows that the ray trajectories are recognizable with the light sheet method, but the individual foci are limited or not distinguishable. Note the scaling of this detail magnification in the µm range, which shows the limits of our light sheet setup, but should not be considered a general limitation of this methodology. In contrast, the new method (▶ **Fig. 4 b**) allows the localization of the focal points.

▶ **Fig. 5** shows 4 cross-sectional images derived from optical bench measurements for different pupil sizes in logarithmically scaled intensities. In each cross-sectional image, the near focus is at an axial position of approximately 0.4 mm, the intermediate focus is at approximately 0.9 mm, and the far focus is at approximately 1.5 mm. Furthermore, in addition to the focal points just mentioned, ray extensions with lower intensity are clearly visible in both axial and lateral image directions. At the various focal points, especially in the intermediate focus, halos appear in the outer image areas, which only appear with the new algorithm, with SNR improved by about 2 orders of magnitude. We have published detailed studies on this subject [19]. On closer inspection, as pupil size increases, the focal points shift to smaller axial position values.

To investigate the distribution of intensity along the optical axis in detail, the through-focus curves were calculated as a function of d_{IOL} pupil size. ▶ **Fig. 6** shows the through-focus curves of d_{IOL} = 2.93 mm in purple, d_{IOL} = 3.91 mm in turquoise, d_{IOL} = 4.89 mm in yellow, and d_{IOL} = 5.87 mm in orange. The near focus is in the axial position range between 0.4 and 0.6 mm, the intermediate focus between 0.9 and 1.2 mm and the far focus between 1.5 and 1.6 mm. With increasing pupil size, the intensity in the focal points increases. In each case, a clear increase in intensity can be seen between approximately 3 and 4 mm and 4 and 5 mm pupil diameter. The highest intensity is at the far focus, followed by the near focus and intermediate focus. In addition, as can already be seen on closer inspection in ▶ **Fig. 5**, the position of the near, intermediate, and far focus shifts to smaller values of axial position with increasing pupil size. During the transition from 5 to 6 mm, the maximum intensity of the foci hardly changes, which suggests that for the most part the additional irradiated energy remains far from the optical axis.

Discussion

Based on the 3-D PSF measurements with an optical bench on a diffractive trifocal IOL, our study presents a new image processing algorithm that specifically exploits the rotational symmetry of

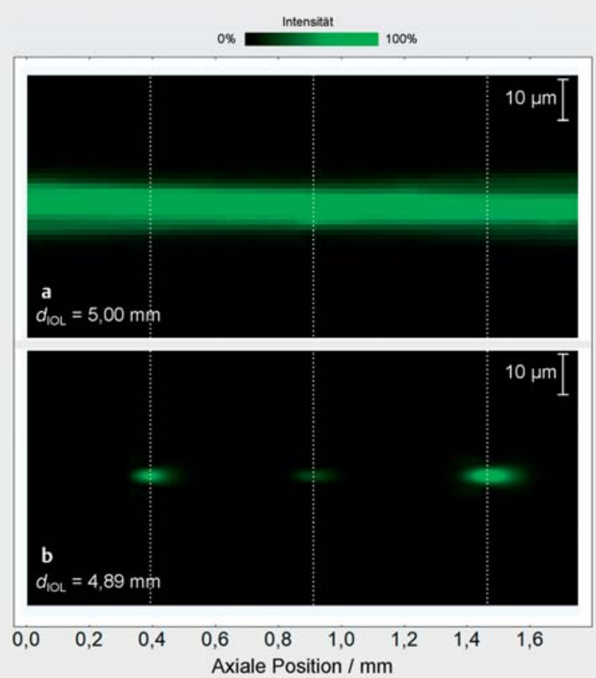

▶ **Fig. 4** Comparison of cross-sectional images of the IOL under investigation taken using (**a**) fluorescein bath and (**b**) optical bench (pupil diameter $d_{IOL} \approx 5.00$ mm) in a linear intensity scaling. **a** Shows the light distribution in a fluorescein bath illuminated by a laser taken with a laterally placed camera. The individual focal points cannot be delineated. **b** Shows the light distribution of the same IOL calculated from the 3-dimensional optical bench measurements illuminated by a green LED. Here, all focus points are clearly distinguished from each other.

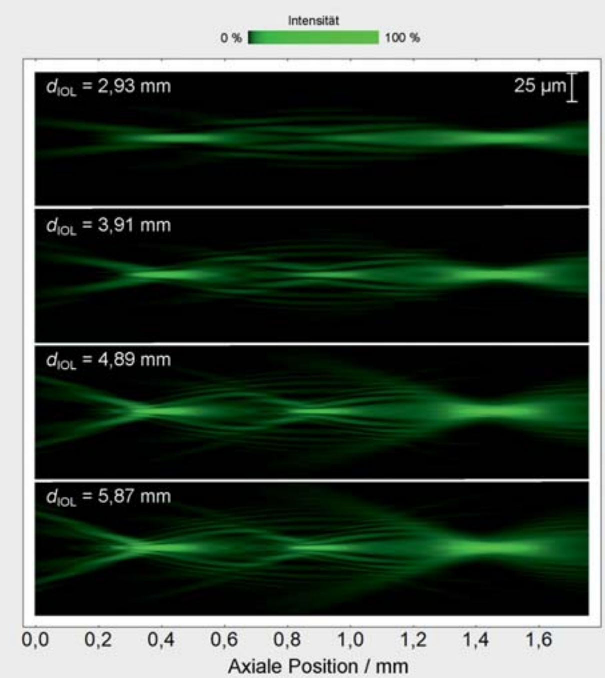

▶ **Fig. 5** The cross-sectional images for different pupil diameters (d_{IOL}) of a trifocal IOL in logarithmic representation using a green LED. The images were taken with a monochrome camera and colored green. The near focus is at an axial position of ≈ 0.4 mm, the intermediate focus is at ≈ 0,9 mm, and the far focus is at ≈ 1,5 mm. Off the optical axis, clear halos appear.

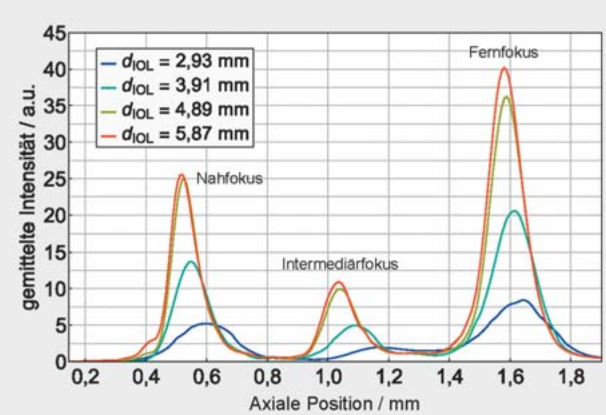

▶ **Fig. 6** The through-focus curves of the IOL used for 4 different pupil diameters (d_{IOL}) using the green LED. The distribution of the intensity along the optical axis is shown as a function of the axial position in mm.

IOLs. This approach significantly improves the image quality of the corresponding cross-sectional images compared to previous methods.

At this point, it should be emphasized once again that the generation of cross-sectional images using the light sheet method is a well-established method for visualizing IOL focal areas, the application of which meets the requirements in many cases. The seminal works of the groups around Eppig [11], Terwee [20], and Son [14, 21] may be cited as examples. 3-D PSF measurements with an optical bench require a considerably higher experimental, temporal as well as computational effort. Both experimental approaches, the light sheet method and methods with optical benches, represent the "state of the art" for the determination of optical IOL properties. Each method has its limitations, in the case of the fluorescein bath approach by the dependence of the image quality on the required light sheet thickness and in the case of the optical bench by the width of the extracted volume from the 3-D PSF. Both lead to a reduction in the image quality of the cross-sectional images and ultimately to limitations in quantitative analysis.

The higher optical resolution of the optical bench method compared to the light sheet method was demonstrated with ▶ **Fig. 4**. This higher resolution is clearly supported with the better SNR values [19]. In this way, fine structures such as halos, which the light sheet method cannot visualize, can be resolved (cf. ▶ **Fig. 5**). Specifically, in the IOL example shown, we observe an overlap between the intermediate and far focus for pupil diame-

Heruntergeladen von: Ricardo Elsner, Universität Rostock. Urheberrechtlich geschützt.

ters at ≈ 3.0 mm in the cross-sectional images of the new method. Consistently, Vega et al [9] reported that smaller pupil apertures increase the extension of the focal point along the optical axis, which consequently can lead to overlap between different focal regions of MIOLs. The cross-sectional images further show a shift of the focal points along the optical axis to smaller values of the axial position with increasing pupil size, indicating a positive spherical aberration of the cornea and IOL system. This relationship is also reflected in the through-focus curves in that foci shift to smaller values of axial position as pupil size increases. This property is not derivable from individual 2-D PSFs and is also difficult to reproduce based on through-focus curves generated with fluorescein cross-sectional images [11]. In the same way, chromatic aberrations could be visualized by taking images at different wavelengths and comparing them. For example, Millán and colleagues studied the effect of focus shift and intensity distribution for 3 different MIOLs in terms of wavelength dependence, as the influence of chromatic aberration could have a negative impact on visual perception in the human eye [10]. The 3D PSF can be used to determine not only the influence of chromatic aberration, but also the effects of spherical aberration (SA). Thereby, considering the off-axis rays, focal point shifts towards the lens speak for a positive SA and focal point shifts away from the lens speak for a negative SA [22]. For large pupil diameters, the SA of 3-D PSF becomes increasingly evident [23].

In general, the light sheet method also makes it possible to infer chromatic properties [11], but since fluorescein cannot be excited with red light, another dye or a scattering medium would have to be used in the case of red light. In addition, measurements on optical benches can provide accurate information about decentering and tilt of the IOL and its intensity distribution as a function of pupil diameter, as shown by Borkenstein and colleagues [24]. Both the light sheet method and the optical bench measurement methods present the scientific standard for the determination of cross-sectional images in this research area, however, there may always be a reduction in the image quality of the cross-sectional images; in the case of the fluorescein bath this is due to the dependence of the light sheet thickness, and in the case of the optical bench this is due to the width of the extracted volume from the 3-D PSF.

The light sheet method is clearly advantageous because it is easy to implement and the results can be obtained quickly without any computational effort. This has been clearly shown in numerous publications. Against this is the immense influence of the light sheet thickness, which is, however, also a substantial limitation in our setup. In addition, the optical resolution would need to be significantly improved in our setup. In addition, fluorescence is based on the absorption of light by the fluorescein molecules, which implies that the intensity of the light distribution decreases along the optical axis. Thus, the axial energy distribution cannot be precisely quantified. In addition, impurities can lead to image artifacts that complicate or even prevent automated evaluations or distort the inferred results.

The new image processing algorithm was developed for rotationally symmetric IOLs, such as monofocal IOLs and also most multifocal diffractive IOLs. In addition to these IOLs, other MIOL design approaches exist based, for example, on combining different refractive elements [25]. Due to their consequently asymmetric 3-D PSF, the application of the new algorithm results in inaccurate beam profiles, which may lead to misinterpretation and erroneous conclusions about the IOLs under investigation. However, rotationally symmetric refractive MIOLs do not pose a problem with this method. A further disadvantage of the new algorithm is the long calculation time of approx. 30–40 min. However, porting the algorithm to a higher-performance programming language or consequent further parallelization on a graphics card could reduce this high computation time. In addition to this aspect, future research should extend the newly developed method to include the determination of other important optical parameters of IOLs, such as energy efficiency, modulation transfer function, or longitudinal chromatic aberration.

Abstract

Cross-sectional images and through-focus curves are used to understand IOL functional principles as well as halo formation and can also be used to analyze the performance of IOLs. The presented combination of an optical bench and the newly developed algorithm of 3-D data sets enables precise calculation of cross-sectional images of rotationally symmetric IOLs. In terms of image quality and signal-to-noise ratio, our investigations of the newly developed method show higher quality results compared to our investigations of the light sheet method. Intensities in the periphery of the optical axis, e.g. halos, are now detectable with higher contrast in the cross-sectional images with logarithmic intensity scaling and therefore easier to identify compared to other methods. The potential of the novel image processing algorithm in combination with a suitable optical bench allows both quantitative and qualitative analysis of rotationally symmetric IOLs.

Acknowledgements

The authors would like to thank Carl Zeiss Meditec AG for their support.

Conflict of Interest

The authors declare that they have no conflict of interest.

References

[1] Modi S, Lehmann R, Maxwell A et al. Visual and Patient-Reported Outcomes of a Diffractive Trifocal Intraocular Lens Compared with Those of a Monofocal Intraocular Lens. Ophthalmology 2021; 128: 197–207. doi:10.1016/j.ophtha.2020.07.015

[2] Davison JA, Simpson MJ. History and development of the apodized diffractive intraocular lens. J Cataract Refract Surg 2006; 32: 849–858. doi:10.1016/j.jcrs.2006.02.006

[3] Salerno L, Tiveron M, Alió J. Multifocal intraocular lenses: Types, outcomes, complications and how to solve them. Taiwan J Ophthalmol 2017; 7: 179. doi:10.4103/tjo.tjo_19_17

[4] Maurino V, Allan BD, Rubin GS et al. Quality of Vision after Bilateral Multifocal Intraocular Lens Implantation. Ophthalmology 2015; 122: 700–710. doi:10.1016/j.ophtha.2014.10.002

[5] Simpson MJ. Diffractive multifocal intraocular lens image quality. Appl Opt 1992; 31: 3621. doi:10.1364/AO.31.003621

Heruntergeladen von: Ricardo Elsner, Universität Rostock. Urheberrechtlich geschützt.

[6] Carretero L, González C, Fimia A et al. Application of the Ronchi test to intraocular lenses: A comparison of theoretical and measured results. Appl Opt 1993; 32: 4132. doi:10.1364/AO.32.004132

[7] Bos G, Vanzo J-M, Maufoy J, Gutzwiller JL. New interferometric Method to assess intraocular Lens Characteristics. In: Silberman DM, ed. Ophthalmic Lens Design and Fabrication II. Los Angeles, CA: SPIE Proceedings; 1994: 56

[8] Ravalico G, Parentin F, Sirotti P et al. Analysis of light energy distribution by multifocal intraocular lenses through an experimental optical model. J Cataract Refract Surg 1998; 24: 647–652. doi:10.1016/s0886-3350(98)80259-9

[9] Vega F, Alba-Bueno F, Millan MS. Energy efficiency of a new trifocal intraocular lens. JEOS: RP 2014; 9: 14002. doi:10.2971/jeos.2014.14002

[10] Millán MS, Vega F. Through-Focus Energy Efficiency and Longitudinal Chromatic Aberration of Three Presbyopia-Correcting Intraocular Lenses. Transl Vis Sci Technol 2020; 9: 13. doi:10.1167/tvst.9.12.13

[11] Eppig T, Rubly K, Rawer A et al. Visualization of Light Propagation with Multifocal Intraocular Lenses Using the Ouzo Effect. Biomed Res Int 2019; 2019: 6425040. doi:10.1155/2019/6425040

[12] Petelczyc K, Kolodziejczyk A, Błocki N et al. Model of the light sword intraocular lens: in-vitro comparative studies. Biomed Opt Express 2020; 11: 40. doi:10.1364/BOE.11.000040

[13] Reiß S, Forbrig J, Guthoff R et al. Optimierung der Visualisierungstechnik für Strahlenverläufe durch Intraokularlinsen zur Charakterisierung multifokaler Abbildungseigenschaften von Fresnel-Zonenplatten. Klin Monbl Augenheilkd 2014; 231: 1183–1186. doi:10.1055/s-0034-1383300

[14] Son HS, Łabuz G, Khoramnia R et al. Visualization of Forward Light Scatter in Opacified Intraocular Lenses and Straylight Assessment. Diagnostics (Basel) 2021; 11: 1512. doi:10.3390/diagnostics11081512

[15] Hinze U, El-Tamer A, Doskolovich LL et al. Additive manufacturing of a trifocal diffractive-refractive lens. Opt Commun 2016; 372: 235–240. doi:10.1016/j.optcom.2016.04.029

[16] Holladay JT, Piers PA, Koranyi G et al. A New Intraocular Lens Design to Reduce Spherical Aberration of Pseudophakic Eyes. J Refract Surg 2002; 18: 683–691. doi:10.3928/1081-597X-20021101-04

[17] Wahl S, Song C, Ohlendorf A. Comparison of two devices to simulate vision with intraocular lenses. Clin Ophthalmol 2019; 13: 123–130. doi:10.2147/OPTH.S188890

[18] Gerlach M, Guthoff R, Stachs O et al. Präklinische Bewertung von Intraokularlinsen durch simulierte Implantation. Klin Monbl Augenheilkd 2018; 235: 1332–1341. doi:10.1055/a-0764-5079

[19] Sievers J, Elsner R, Bohn S et al. Method for the generation and visualization of cross-sectional images of three-dimensional point spread functions for rotationally symmetric intraocular lenses. Biomed Opt Express 2022; 13: 1087. doi:10.1364/BOE.446869

[20] Terwee T, Weeber H, van der Mooren M et al. Visualization of the retinal image in an eye model with spherical and aspheric, diffractive, and refractive multifocal intraocular lenses. J Refract Surg 2008; 24: 223–232. doi:10.3928/1081597X-20080301-03

[21] Son HS, Labuz G, Khoramnia R et al. Ray propagation imaging and optical quality evaluation of different intraocular lens models. PLoS One 2020; 15: e0228342. doi:10.1371/journal.pone.0228342

[22] Holladay JT. Spherical Aberration: The Next Frontier. Only by understanding the math can ophthalmologists target ideal correction for their patients. Cataract & Refractive Surgery Today. Nov. 2006. Accessed November 8, 2022 at: https://crstoday.com/articles/2006-nov/crst1106_18-php/

[23] Amigó A, Bonaque-González S. Q Factor Presbylasik. Fundamentals and therapeutic approach. J Emmetropia 2012; 3: 167–171

[24] Borkenstein AF, Borkenstein EM, Luedtke H et al. Impact of decentration and tilt on spherical, aberration correcting and specific aspherical intraocular lenses; an optical bench analysis. Ophthalmic Res 2022; 65: 425–436. doi:10.1159/000522510

[25] Alio JL, Plaza-Puche AB, Javaloy J et al. Comparison of a New Refractive Multifocal Intraocular Lens with an Inferior Segmental Near Add and a Diffractive Multifocal Intraocular Lens. Ophthalmology 2012; 119: 555–563. doi:10.1016/j.ophtha.2011.08.036

Heruntergeladen von: Ricardo Elsner, Universität Rostock. Urheberrechtlich geschützt.

tvst

Lens

Assessment of Diffractive Intraocular Lenses Using Near-Infrared Light: A Critical Evaluation

Ricardo Elsner[1,2], Mario Gerlach[3], Sebastian Bohn[1,2], Jan Sievers[4], Heinrich Stolz[5], Rudolf F. Guthoff[1,2], Oliver Stachs[1,2], and Karsten Sperlich[1,2]

[1] Department of Ophthalmology, Rostock University Medical Center, Rostock, Germany
[2] Department Life, Light & Matter, University of Rostock, Rostock, Germany
[3] Carl Zeiss Meditec AG, ZEISS Group, Berlin, Germany
[4] Institute of Physics, Martin–Luther–University Halle–Wittenberg, Halle (Saale), Germany
[5] Institute of Physics, University of Rostock, Rostock, Germany

Correspondence: Ricardo Elsner, Department of Ophthalmology, Rostock University Medical Center, Doberaner Str. 140, Rostock 18057, Germany. e-mail: elsner.ricardo@gmail.com or ricardo.elsner@charite.de

Received: December 13, 2024
Accepted: May 15, 2025
Published: June 30, 2025

Keywords: NIR light; diffractive IOL; MIOL; optical bench; wavefront aberrometer

Citation: Elsner R, Gerlach M, Bohn S, Sievers J, Stolz H, Guthoff RF, Stachs O, Sperlich K. Assessment of diffractive intraocular lenses using near-infrared light: A critical evaluation. Transl Vis Sci Technol. 2025;14(6):36, https://doi.org/10.1167/tvst.14.6.36

Purpose: After cataract surgery, near-infrared (NIR) light–based optical devices are commonly used for in vivo vision quality assessment, using wavefront sensors and double-pass techniques. This study investigates the diffraction efficiencies and orders of the AT LISA tri 839MP (Carl Zeiss Meditec AG, Berlin, Germany) under visible and NIR illumination, highlighting challenges in using NIR-based devices to evaluate diffractive intraocular lenses (IOLs).

Methods: This study uses an optical bench system to generate in vitro through focus intensity data and compares the results to an optics simulation using the manufacturer's theoretically designed diffractive surface topography of the investigated trifocal IOL instead of possibly error-prone measured topography data.

Results: For visible light, through-focus curve intensities and energy efficiencies behaved as expected. However, under NIR light, near and intermediate foci showed significantly reduced intensities compared to the far focus. Energy efficiency measurements indicate suboptimal performance of the near and intermediate foci with NIR light. Under these conditions, the investigated trifocal IOL became almost monofocal.

Conclusions: The study demonstrates the wavelength-dependent behavior of the diffractive IOL, emphasizing the risks of inaccurate assessments when using NIR-based devices. It highlights the need for visible-light-based techniques for accurate evaluation and the importance of using precise surface topography data in simulations.

Translational Relevance: This research bridges the gap between basic research and clinical care by showing that vision assessments performed with NIR-light inaccurately evaluate diffractive IOLs, guiding clinicians toward visible-light techniques for accurate vision assessment.

Introduction

The implantation of multifocal intraocular lenses (MIOLs) during cataract surgery or presbyopic lens exchange is a commonly used approach to offer patients spectacle independence. The development of advanced lens designs is very complex, involving a wide range of boundary conditions. Within the group of MIOLs, diffractive multifocal IOLs (DMIOLs) use a more intricate approach than refractive MIOLs. They usually consist of a refractive base shape, serving for the far focus, with a topographical diffractive ring pattern applied on the lens surface that creates the additional focal points, as defined by their specific add power. In summary, these DMIOLs achieve their multifocality based on refraction and interference effects.[1,2] Because the human eye has its greatest sensitivity around 550 nm, as shown by the CIE photopic luminous efficiency function $V(\lambda)$,[3] DMIOLs are

Copyright 2025 The Authors

This work is licensed under a Creative Commons Attribution-NonCommercial-NoDerivatives 4.0 International License.

Downloaded from tvst.arvojournals.org on 10/17/2025

translational vision science & technology

translational vision science & technology

generally designed for green wavelengths. This design wavelength is set at 546 nm ±10 nm in accordance with the ISO standard 11979-2:2024.[4]

For the objective analysis of the imaging properties of IOLs, optical benches, wavefront aberrometers, and double-pass systems are used. In that context, optical bench systems analyze the Airy disk, modulation transfer function (MTF), and the point spread function (PSF) of IOLs. The Airy disk is a characteristic diffraction-limited pattern of light that defines the smallest possible size to which a point light source can be imaged. The PSF describes how an imaging system would depict an ideal, punctiform object and is the corresponding intensity plot of the Airy disk but also accounts for additional aberrations in a non-diffraction limited scenario, as with the investigated DMIOL. An optical bench, as introduced in Sievers et al.,[5] uses green light, whereas others use white light (e.g., Petelczyc et al.[6]) or NIR light (e.g., Vega et al.[7,8]).

Ginis et al. developed a model eye equipped with a camera acting as the retina, where the lenses in front of the model eye enable the automated recording of a defocus curve with a series of optotypes to examine the lenses' performance requirements in visual tasks such as reading in different distances—among others for the IOL investigated here.[9]

However, when assessing the visual outcomes and imaging properties of implanted DMIOLs in a clinical context, wavefront aberrometers[10–21] and double-pass–based systems[22–28] have been used by several authors. These devices generally use light in the NIR spectral band (780–1000 nm) to determine the postoperative visual outcome and the patient's pseudophakia. The use of NIR light for in vivo assessment of vision quality has some important advantages and is based on the increasing reflectivity of the retina with increasing wavelength.[29] Furthermore, glare decreases, and the maximum permissible exposure increases,[30] are especially important for double-pass systems.

A Clarivate "Web of Science" search was used to obtain an estimated number of publications analyzing DMIOLs with devices using NIR light. This search was conducted for several commercial NIR light-using devices, which are composed in a Table (see Supplementary Table S1), yielding 12 results for wavefront aberrometers and seven for double-pass systems. For example, the search with the search parameters "iTrace AND diffractive IOL" yielded six results. However, we do not claim the reference list to be complete. A total of 396 citations related to DMIOLs and NIR light were found.

Nevertheless, DMIOLs are not optimized for NIR light, consequently leading to different visual outcomes when analyzed under these conditions. This specifically means that the results of wavefront refractive values like sphere and cylinder (lower-order aberrations), but also coma, spherical aberration and trefoil (higher-order aberrations) may be erroneous. Several recent studies are overlooking the risks of wrong assumptions when analyzing DMIOLs with NIR light, even though previous studies by Charman et al.,[31] Campbell,[32] and Vega et al.[7,8] have already shown that optical performance testing of this type of lenses is problematic.

Charman et al.[31] emphasize that wavefront aberrometers give erroneous results when analyzing pseudophakic eyes with diffractive IOLs. Gatinel[33] points out that the analysis of diffractive IOLs with double-pass systems such as the OQAS using wavelengths of 780 nm leads to an altered light distribution in the foci of the DMIOL. Thus most of the light energy is directed into the zeroth diffractive order, while much less energy ends up in the first or higher orders (i.e., in the near or intermediate focus), which are essential for the multifocality of the lens. Furthermore, Vega et al.[8] recently showed that the distribution of light energy to the focal points of a DMIOL is strongly wavelength dependent and that measurements with NIR light, instead of the design wavelength, lead to different optical performances.

Previous theoretical works about additive power and diffraction efficiency have two important implications. First, longer wavelengths like NIR light

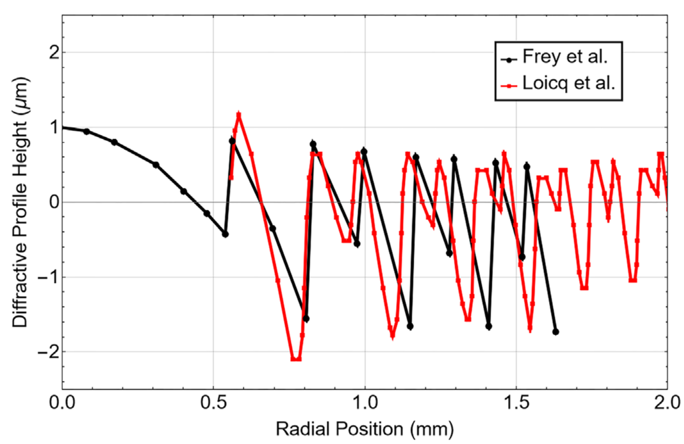

Figure 1. Comparison of two experimentally measured diffractive surface profiles of the AT LISA tri 839MP. Frey et al.[37] used a confocal microscope (MarSurf CWM 100) for the topography analysis, whereas Loicq et al.[38] used an optical profilometer (Bruker Contour GTI). Both published diffractive profiles served as a basis for further optics simulations of the investigated IOL raising the question which of the profiles is most accurate. The profiles were extracted using g3data (https://github.com/pn2200/g3data, an open-source program available under the GNU General Public License).

Downloaded from tvst.arvojournals.org on 10/17/2025

increase the additive power of the near and intermediate focus since diffractive power is proportionally dependent on wavelength.[34] Second, the wavefront intensity will be weaker for the near focus with respect to the far focus because diffractive efficiency decreases with longer wavelengths and more light is directed into the zeroth diffractive order.[35] As a result, the postoperative vision quality assessment of pseudophakic eyes with DMIOLs is in considerable doubt.

Recent studies derived simulation data from experimentally obtained surface topography data—for monofocal IOLs[36] and DMIOLs.[8] However, in the case of DMIOLs, discrepancies in the accuracy of these surface profiles suggest limitations in such approaches as shown in Figure 1. This study seeks to address this gap by demonstrating the wavelength and pupil size–dependent effects on through-focus curves and diffraction efficiencies of the AT LISA tri 839MP. Unlike previous research that relied on experimentally derived topography data,[37–39] we used the manufacturer's theoretically designed surface topography to achieve a more accurate optical simulation. Our results complement previous findings and further underline the need for future visible-light techniques to evaluate DMIOLs.

Methods

The experimental setup is composed of an optical bench incorporating the IOL under examination in a model eye with water immersion. The optical bench (see Fig. 2) was already published in detail by Sievers et al.[5] and is briefly explained in the following. In contrast to Sievers et al.[5], where only a green LED (λ_c = 530 nm, λ_{FWHM} = 47 nm) was used, the optical bench was equipped with three additional LEDs: a blue LED (λ_c = 463 nm, λ_{FWHM} = 23 nm), a red LED (λ_c = 628 nm, λ_{FWHM} = 15 nm) and a NIR LED (λ_c = 789 nm, λ_{FWHM} = 32 nm). The LED spectra were measured with a fiber optic spectrometer (AVASPEC-ULS4096CL-EVO; Avantes, Apeldoorn, The Netherlands).

The monochromatic LED light passes a pinhole (15 µm; Thorlabs, Newton, NJ, USA) and is collimated by an achromatic lens (f = 150 mm; AC254-150-A1, Thorlabs, Newton, New Jersey, USA). The diameter of the collimated beam is adjustable by an aperture (SM1D12C; Thorlabs). For the sake of simplicity, the model eye of the VirtIOL was used in our measurements.[40] The model eye consists of a model cornea, an off-the-shelf achromatic lens with an effective focal

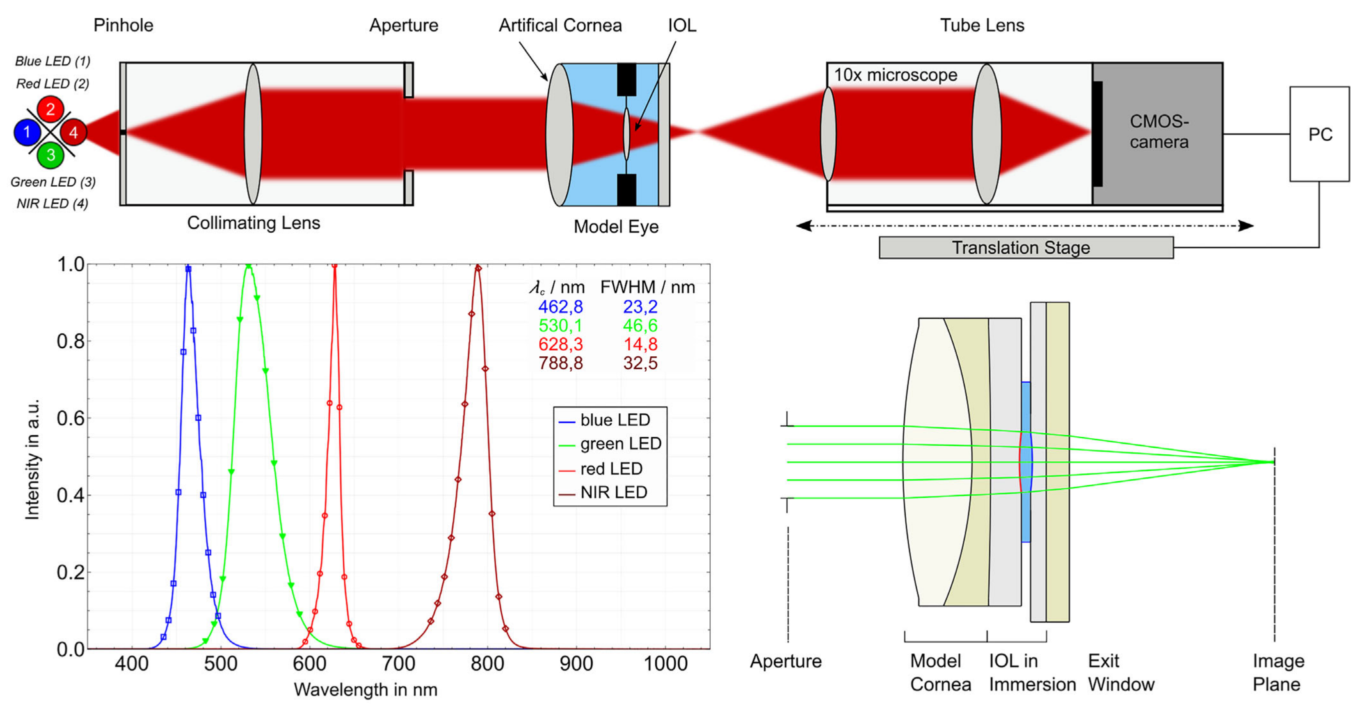

Figure 2. Schematic optical bench setup for the acquisition of three-dimensional focal light distributions. A blue (*1*), red (*2*), green (*3*), and NIR (*4*) LED were integrated into the setup. The associated spectral bands are shown at the bottom left, specified by central wavelength λ_c and FWHM (full-width half-maximum). The IOL is immersed in water within a model eye with an artificial cornea. The illuminated diameter on the IOL is adjusted with the aperture. A camera-based microscope is translated along the optical axis. The optical layout of the simulation environment is shown at the bottom right. The red IOL surface indicates a true topographical surface modeling of the diffractive IOL.

Downloaded from tvst.arvojournals.org on 10/17/2025

length of 40 mm and neutral spherical aberration, an IOL holder with the IOL under testing in water immersion, and a window at the back. Because the achromatic lens is in contact with water at one surface, it is no longer achromatic and free of spherical aberration and, hence, does not comply with ANSI Z80.35:2018 and ISO 11979-2:2024[4] specifications for a model eye, which should come as close as possible to the spherical and chromatic aberration of the eye. However, this study does not address the effects of polychromatic light on diffractive lenses but rather the effects of monochromatic light on diffraction efficiency and thus on the diffraction orders. The exact amount of chromatic aberration of each focus is irrelevant to the conclusions drawn in this article.

A diffractive trifocal IOL (AT LISA tri 839MP; Carl Zeiss Meditec AG, Berlin, Germany) with an optical base power of 25.00 dpt, an add power of 3.33 D for the near and 1.66 D for the intermediate focus was investigated. The illuminated area on the model cornea is adjusted using the iris diaphragm (aperture) positioned in front of the model eye. The illuminated IOL diameter d_{IOL} was determined for a set of diameters d_{A} of the iris diaphragm using Ansys Zemax OpticStudio (ANSYS Inc. Headquarters, Canonsburg, PA, USA). An almost linear relationship exists between the two diameters. Table 1 presents the various pupil diameters that were set during the measurement series.

Table 1. Relation Between the Aperture d_{A} and the Illuminated IOL Diameter d_{IOL}

d_{A} in mm	2.5	3.0	3.5	4.0	4.5	5.0	5.5	6.0
d_{IOL} in mm	2.12	2.54	2.96	3.38	3.80	4.22	4.65	5.07

A CMOS-camera-based microscope (microscope objective IC10 MD-Plan, NA = 0.25 [Olympus, Shinjuku, Japan] and a 150 mm achromatic tube lens) is automatically translated with an increment of s_{I} = 7.63 µm along the optical axis and records the two-dimensional (2D)-light distribution in the form of sequential images. The three-dimensional (3D)-light distribution of the image stack corresponds to the 3D-PSF of the IOL. The CMOS camera used in this study is a monochrome model (UI-3880CP-M-GL Rev.2; IDS Imaging Development Systems GmbH, Obersulm, Germany). According to the EMVA test report for this camera (IDS, UI-3880CP-M-GL R2, 4103099007, April 27, 2017), the linearity error in the default setting is 0.26%; hence, no linearity correction was applied. The spectral quantum efficiency of the sensor was not taken into account, as well as the intensity of the respective LEDs. This is valid because we only present normalized or relative data, except for Figure 3. Accounting for spectral quantum efficiency and optical power of the LEDs would only

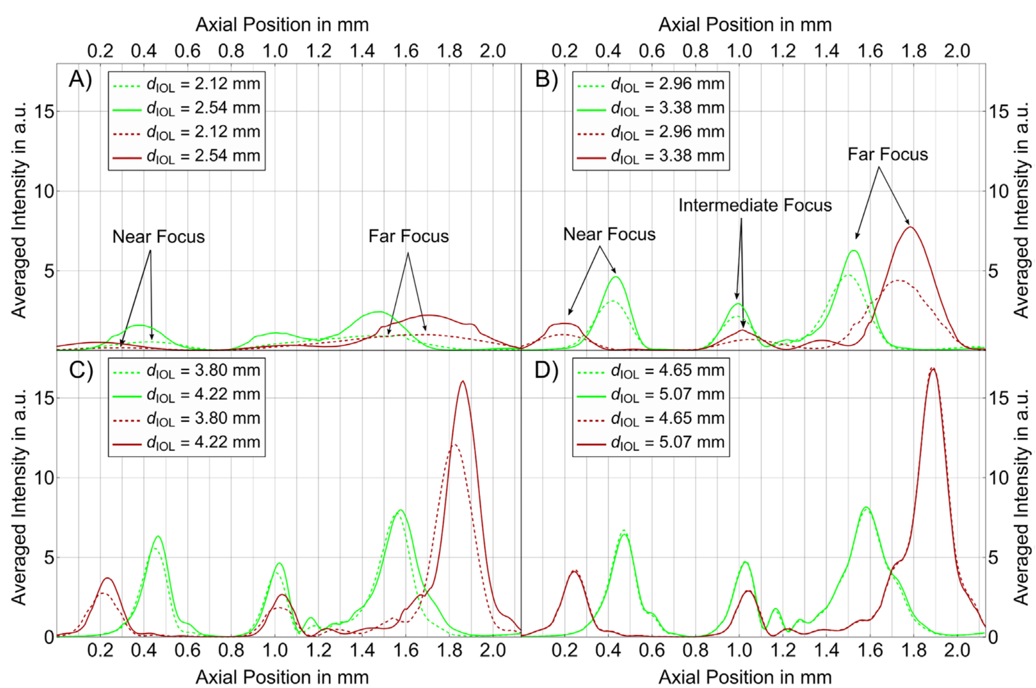

Figure 3. Overview of through-focus curves. Through-focus curves for eight different pupil diameters using a diffractive trifocal IOL (AT LISA tri 839MP; Zeiss Meditec AG) in the model eye at 530 nm illumination (green light, *green lines*) and at 789 nm Illumination (NIR light, *dark red lines*). For both wavelengths, (**A**) shows the through-focus curves for 2.12 and 2.54 mm, (**B**) for 2.96 and 3.38 mm, (**C**) for 3.80 and 4.22 mm, and (**D**) for 4.65 and 5.07 mm pupil diameters. With increasing pupil size, the intensity increases. For 2.12 mm pupil size, the IOL shows a bifocal character for green and NIR light. See text for further explanation.

translational vision science & technology

Downloaded from tvst.arvojournals.org on 10/17/2025

translational vision science & technology

lead to a scaling, but not to a deformation of the through-focus curves. In Figure 3, we present absolute values to keep the information of the pupil size dependent intensity change. However, conclusion on the spectral transmittance of the IOL must not be deduced.

Through-Focus Curve and Energy Efficiency Calculation

The captured 3D-PSF was analyzed based on a proprietary algorithm introduced by Sievers et al.[5], written in Mathematica 12.0 (Wolfram Research Europe Ltd, The Wolfram Centre, Long Hanborough, UK), to determine the through-focus curves, as well as the radial intensity distribution of rotational symmetric IOLs. We used different exposure times for the different pupil sizes and divided the intensity by the respective exposure time. This way, all curves were normalized to 1 ms and the required dynamic range of the camera for appropriately imaging in-focus and out-of-focus PSFs was reduced.

Through-focus curves show the intensity change along the optical axis. The optical axis is in the center of the images captured by the optical bench. The intensity value of each image is calculated by averaging over an area of 11 × 11 central pixels. This area was chosen to maximize the signal-to-noise ratio while maintaining the shape of the through-focus curve. Care was taken to ensure that the size of the square was small enough to avoid artifacts in the through-focus curve. Large averaging areas would smoothen the curves. The square shape was chosen over the more appropriate disc shape for easier implementation.

According to simulations, the Airy disk has a diameter of 73 µm and 60 µm for 3.5 mm and 4.5 mm aperture, respectively. This is equivalent to about 30 pixels and 25 pixels. Table 2 shows the detailed values. For a pixel size of 2.4 µm the angular size of 11 × 11 pixels corresponds to a full angle of approx. 0.5 arcmin in front of the model eye, which is half of the minimum angle of resolution. The ratio of Airy disc diameter to pinhole diameter on the camera is in the order of 3 for the apertures shown here, and thus considered as point light source.

Table 2. Relation Between Pinhole, Aperture, and Simulated Airy Disk

Aperture (mm)	Pinhole on Camera (µm)	Airy Disk on Camera (µm)
3,5	19.2	73
4,5	18.5	60

All specified values are diameters.

Before defining the fixed 11 × 11 pixel square, the entire image stack undergoes a preprocessing step to ensure the best possible alignment with the optical axis. A detailed description of the pre- and post-processing pipeline including background noise correction and centroiding is published in Sievers et al.[5]

Here, for each image another background image was recorded with the same imaging parameter, but with the beam blocked between the pinhole and the collimating lens. These background images were subtracted from the PSF images. Hence, dark current and ambient stray light were neglected.

The algorithm for determining the radial intensity distribution is based on the rotational symmetric design of IOLs, in which 3D-PSFs are rotational symmetric as well. A lateral cross-section of the 3D-PSF can consequently be transferred from a 2D to a one-dimensional (1D) light distribution, which is the radial light distribution.

Within this work, we use two efficiency terms that seem to be similar. The scalar diffraction efficiency, as common in scalar diffraction theory, treats light as a scalar wave and is described, e.g., in the theoretical work of Faklis and Morris.[35] Here, it is specified in arbitrary units and essentially corresponds to the through-focus intensity curve, representing the distribution of on axis energy. In contrast, energy efficiency η refers to the ratio of intensity within a specific focal point to the total incident intensity as described in Equation 1. Hence, contrary to the first term, the latter term also gives information on the amount of light being in the halo pattern. The energy efficiency η is theoretically defined as the ratio of light located in the focal point I_f to the total value of incident light I_L. The total intensity of an image I_{Total} is the value of I_L plus the total value of noise of the camera sensor I_{Noise} (defocused light is not considered as noise). This results in the following correlation for the energy efficiency determined with the optical bench:

$$\eta = \frac{I_f}{I_L + I_{Noise}} = \frac{I_{Airy}}{I_{Total}} \tag{1}$$

Although the in-focus 2D-PSF is known as the Airy disk and may be described by a Bessel function of the first kind, the 2D-PSF of, for example, a trifocal IOL or an out-of-focus image is not necessarily a Bessel function of the first kind. Therefore we first approximate the cross-section of the 2D-PSF by fitting a 1D-Gaussian function to the first elements of the radial intensity distribution. Next, we integrate the fitted function over 2 π to account for the total inten-

Downloaded from tvst.arvojournals.org on 10/17/2025

sity across the entire area, effectively simulating the rotational symmetry of the 1D-Gaussian.

Optics Simulation

An optical simulation procedure was used to verify the experimental results. It was conducted using Ansys Zemax OpticStudio 2023 R2.00 in conjunction with a user-defined surface model to accommodate true diffractive surface topographies and enhanced mathematical analysis methods to calculate the diffraction efficiencies.[34]

The simulation model comprises an in-silico representation of the artificial model eye used in the laboratory experiments. It consists of the same model cornea (achromatic doublet with an effective focal length of 40.0 mm), immersion medium (pure water), the IOL model prescription (AT LISA tri 839MP), and a glass (B270) exit window (see Fig. 2). All optical materials are modeled using dispersion formulas (Schott) covering the entire polychromatic spectral range.

The simulation was conducted using the same four polychromatic spectral bands as described in the experimental setup. The spectral intensity distribution of each spectral band was resampled into 12 weighted wavelength data points used for polychromatic simulation.

The system aperture is placed in front of the artificial model and was set to diameters of 3.5 mm and 4.5 mm (corresponds to $d_{\mathrm{IOL}} = 2.96$ mm and $d_{\mathrm{IOL}} = 3.80$ mm on the IOL surface) to mimic the effect of photopic and scotopic pupils on the imaging properties of the IOL, respectively. A through-focus diffraction efficiency analysis was conducted by variation of the detector distance with respect to the exit window. In the simulation, an absolute x-axis is defined, where 0 mm is at the back of the window of the model eye. The measurement data only has a relative x-axis. In order to present both data side by side, the relative x-axis was shifted so that the far focus overlaps in green at $d_{\mathrm{IOL}} = 2.96$ mm (Fig. 4).

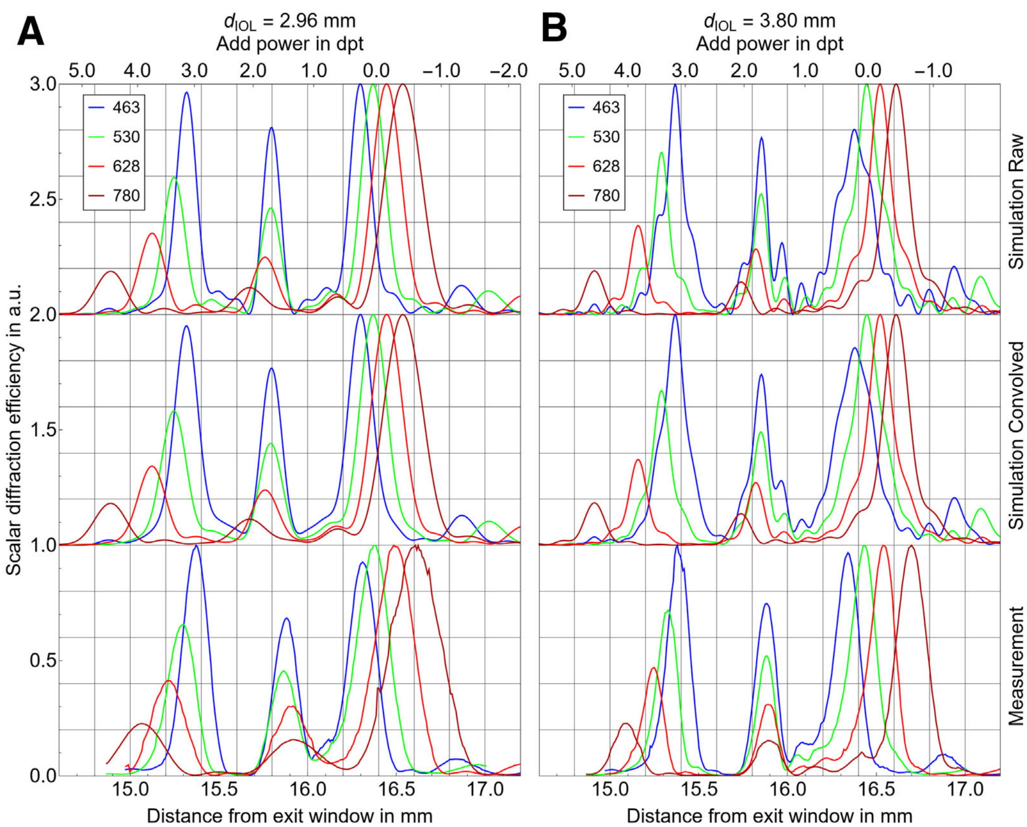

Figure 4. Focal wavelength dependency. Overview of through-focus curves using a diffractive trifocal IOL (AT LISA tri 839MP; Zeiss Meditec AG) and two different pupil diameters: (**A**) 2.96 mm and (**B**) 3.80 mm. All curves were normalized. For the sake of clarity, the through-focus curves of the simulation were shifted by +2 a.u. (*top*). For a better agreement with the measurement data (*bottom*), the simulation curves were convolved with a Gaussian filter width of 84 µm (for A) and 50 µm (for B) and shifted by +1.0 a.u. (*middle*). The bottom axis is presented in mm. A secondary axis in the top is presented in diopters (dpt). The position of 0 dpt was defined by the theoretical far focus position at 546 nm wavelength.

translational vision science & technology

Downloaded from tvst.arvojournals.org on 10/17/2025

Results

The through-focus curves for the investigated IOL under green light (shown in green) and NIR light (shown in dark red) for various pupil sizes ranging from 2.12 mm to 5.07 mm are shown in Figure 3. In each diagram, two pupil sizes are compared (dashed lines represent the smaller and solid lines the larger d_{IOL}). Using green light, the through-focus intensity for $d_{\mathrm{IOL}} \approx 2.1$ mm (top left diagram, dashed green line) reveals two axially extended intensity distributions. Hence, the IOL appears to be bifocal with EDOF characteristics (see Fig. 3A and Supplementary Table S2). By increasing d_{IOL} to about 2.5 mm (solid line), the through-focus curve already shows trifocal behavior. Under NIR light, both through-focus curves are strongly smeared out, resulting in an undefined mixture of bifocal and EDOF IOL. On the top right, in Figure 3B, three distinct foci of similar intensity are visible at both wavelengths. Increasing d_{IOL} further, as depicted in Figures 3C and 3D, the near and far foci shift to greater axial positions. In contrast, the intermediate foci are almost pupil size-independent (cf. Fig. 3 and Supplementary Table S2).

With increasing pupil size, the greatest shift in axial position is exhibited by the far focus under NIR light illumination ($\Delta = 0.18$ mm), followed by the far focus under green light ($\Delta = 0.12$ mm) illumination. Looking at the distance D between the near and far focus ($D_{\mathrm{NEAR\text{-}FAR}}$), there is no remarkable change for green light over the pupil size ($D_{\mathrm{NEAR\text{-}FAR}} \approx 1.10$ mm), whereas under NIR light an increase of $\Delta D_{\mathrm{NEAR\text{-}FAR}} = 0.12$mm could be seen between $d_{\mathrm{IOL}} \approx 2.9$ mm ($D_{\mathrm{NEAR\text{-}FAR}} \approx 1.52$ mm) and $d_{\mathrm{IOL}} \approx 5.9$ mm ($D_{\mathrm{NEAR\text{-}FAR}} \approx 1.64$ mm). This implies that the pupil size dependence for green light is rather small but greater for NIR light. Switching from green to NIR light, the distance between near and far focus increases from $D_{\mathrm{NEAR\text{-}FAR}} \approx 1.10$ mm to $D_{\mathrm{NEAR\text{-}FAR}} \approx 1.64$ mm. At the same time, the near focus shifts to smaller axial positions for NIR light compared to green light.

Briefly, with increasing pupil size, near and far foci shift to greater axial positions - except for 2.12 mm pupil size, where the IOL shows an overlap of a smeared near and intermediate focus leading to a bifocal character for green and NIR light, which then turns into a trifocal character with a shift of the near focus to smaller axial positions.

The optics simulation could confirm the results obtained for green and NIR light. Figure 4 compares these simulation results with the experimental data. The top row shows the simulation data, whereas the bottom row presents the measurement data. Results for the smaller pupil size (3.5 mm $\approx d_{\mathrm{IOL}}$ of 2.96 mm) are shown on the left, and for the larger one (4.5 mm $\approx d_{\mathrm{IOL}}$ of 3.80 mm) on the right. Note that in this representation, all curves are intensity normalized. Since the optical simulation could not yet provide complete agreement with the measurement data and the microscope's depth of field also has to be taken into account, the simulation curves shown here were convolved with a Gaussian filter width of 84 µm (Fig. 4A) and 50 µm (Fig. 4B) to account for the respective depth-of-fields due to the effective numerical apertures (NA). The objective lens and its nominal NA do not primarily determine the depth of field, but rather the light cone emerging from the model eye. This cone effectively reduces the used NA of the objective, because the back aperture is not fully illuminated. Consequently, the objective's full NA is not exploited because of the narrower illumination cone from the model eye.

The measurement data and the convolved simulation are in quite good agreement, considering, for example, the small number of averaged pixels. With larger pupil sizes, the IOL is trifocal for all tested wavelengths. Here, with increasing wavelength, the distance between the near and far focus ($D_{\mathrm{NEAR\text{-}FAR}}$) grows, too, resulting in greater axial shifts to smaller positions for the near and greater positions for the far focus.

However, the intensities of near (I_{near}), intermediate (I_{int}), and far focus (I_{far}), as their intensity ratios, change with wavelength. In contrast to visible light, the intensity ratio of the near or intermediate focus to the far focus decreases for NIR light. The intensity ratio of the peaks decreases with increasing wavelengths since more light falls into the far focus (see Fig. 3). The simulation data shows that with increasing wavelength, the intensity of the near and intermediate focus decreases relative to the far focus. Supplementary Table S3 shows the intensity ratios of the near to far focus ($I_{\mathrm{near}}/I_{\mathrm{far}}$) and intermediate to far focus ($I_{\mathrm{int}}/I_{\mathrm{far}}$) for all four wavelengths, comparing simulated data (S) and measurement data (M). There is a decreasing tendency in the intensity ratio values for near and intermediate focus with increasing wavelength, i.e., the far focus is more dominant than the other foci. This tendency is also depicted in Figure 5. From blue to NIR light, the ratio falls to approximately one-quarter.

This behavior is even more striking when looking at energy efficiencies. As defined above, energy efficiency measures the amount of light contributing to the individual foci. Figure 6 presents a comparable overview of each focus's pupil size-dependent energy efficiency η using green (left) and NIR light (right) to

translational vision science & technology

Downloaded from tvst.arvojournals.org on 10/17/2025

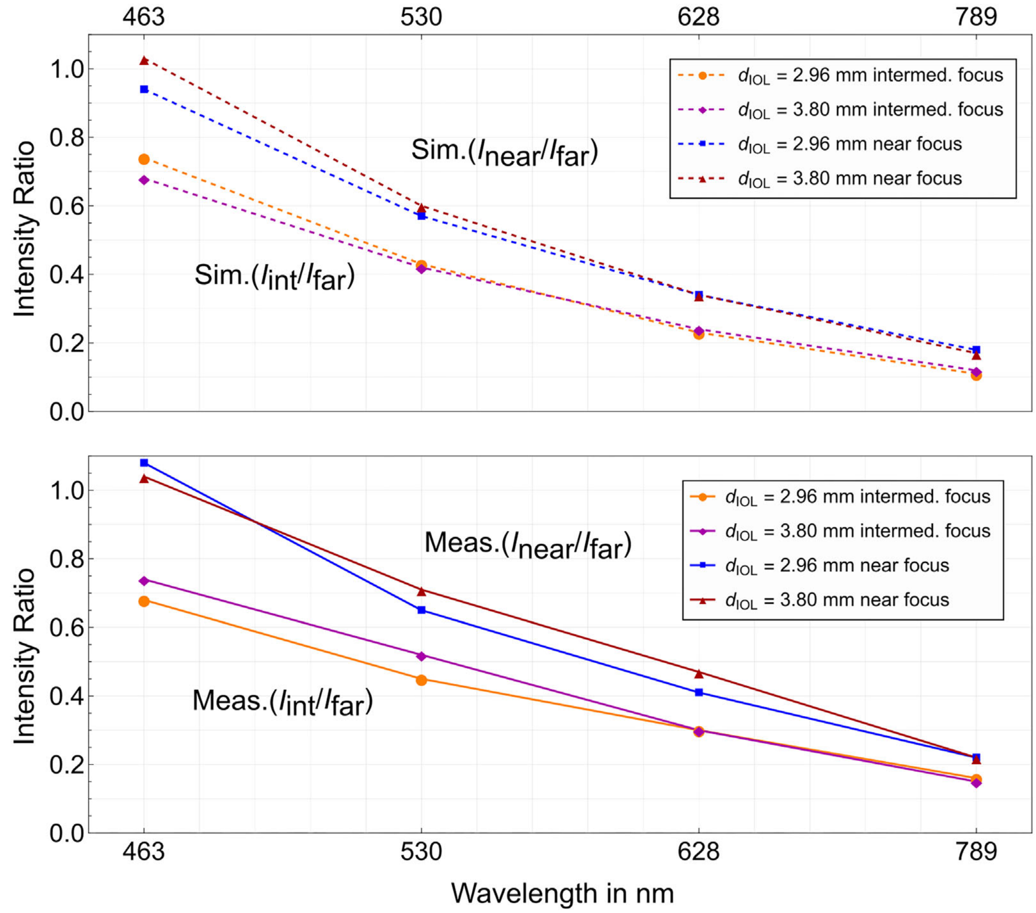

Figure 5. Wavelength dependence of intensity ratios. The figure shows the intensity ratios for the near and far focus (I_{near}/I_{far}) as for the intermediate and far focus (I_{int}/I_{far}) for all four wavelengths, comparing simulated data (*top*: Sim., *dashed lines*) and measurement data (*bottom*: Meas., *solid lines*). A decreasing tendency in the intensity ratio values for near and intermediate focus is found with increasing wavelength.

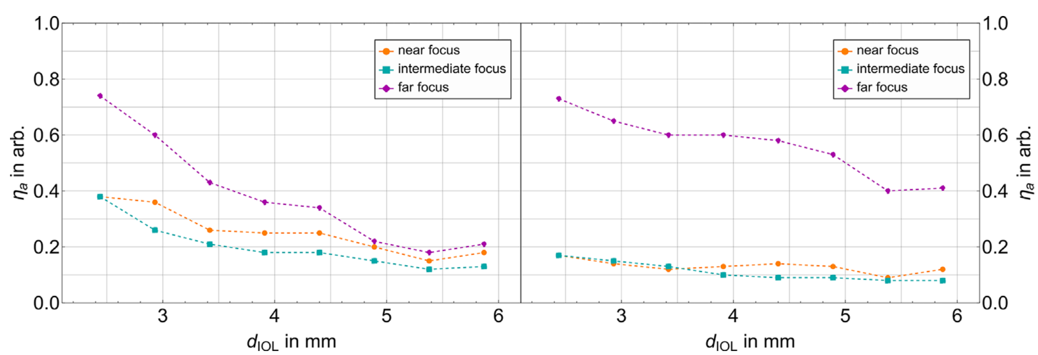

Figure 6. Calculated energy efficiencies from measurement data. Overview of the pupil size-dependent energy efficiencies of a diffractive trifocal IOL (AT LISA tri 839MP; Zeiss Meditec AG) for the near (*yellow circle*), intermediate (*light blue square*), and far focus (*purple diamond*). *Left*: 530 nm illumination (green light). *Right*: 789 nm illumination (NIR light). Using NIR light, much more energy is diffracted into the far focus and less light into the near and intermediate focus compared to green light, resulting in a monofocal behavior of the trifocal IOL under NIR light.

highlight the difference between design wavelength and NIR-based analysis. For both wavelengths, the energy efficiency of each focus decreases with increasing pupil size because of a loss of light in halos and higher-order aberrations.

Although the far focus efficiency for green light and small pupil sizes is almost twice as high compared to the other foci, it approaches the other foci's energy efficiencies at large pupil sizes. However, using NIR light, the far focus is more than four times as efficient

Downloaded from tvst.arvojournals.org on 10/17/2025

as the other foci and remains at approximately four times higher efficiencies for larger pupil sizes. While comparing both wavelengths, the near and intermediate foci energy efficiencies decrease from about 25% (near) and 18% (intermediate) for green light to about 14% (near) and 9% (intermediate) for NIR light at 4.5 pupil diameter. These measurement findings are consistent with our simulation findings. Hence, in using NIR light, much more energy is diffracted into the far focus and less into the near and intermediate focus compared to green light. This implies that although this specific diffractive IOL is trifocal for visible light, it becomes almost monofocal for NIR light.

Discussion

Regardless of the numerous publications addressing the challenge of evaluating the optical performance of DMIOLs under NIR light, a significant amount of recent research (see Supplementary Table S1) still neglects the findings presented in these studies. To get a subjective impression of the imaging properties of a DMIOL before implantation, optical see-through devices like, for example, the VirtIOL (10Lens S. L. U., Terrassa, Spain), which imprint the optical properties of the IOL onto the patient's retina, were developed and can be used for in vivo studies. Newer systems used for IOL vision simulation are, for example, the ACMIT IOL simulator (Austrian Center for Medical Innovation and Technology, Vienna, Austria)[41] and the RALV system (Real Artificial Lens Vision, FirstQ, Mannheim, Germany). Other systems like the VAO simulator (VOPTICA, Murcia, Spain) or SimVis Gekko (2EyesVision, Madrid, Spain) are based on adaptive optics technology, which dynamically modify optical wavefronts to simulate different optical corrections, including IOLs, spectacles, and contact lenses. Letter uses a tunable lens system to replicate different lens designs without requiring physical lens replacement.

However, to objectively assess the optical performance of DMIOLs and confirm optical simulations, in vitro studies are performed on optical benches. These are either commercially available or specifically designed optical benches. The general characteristics of currently used benches are a collimated light beam, an IOL installed in a model eye, a camera for recording the 2D-PSF, and hardware for image data processing. To ensure the comparability of optical IOL properties, the updated ISO standard 11979-2:2024[4] was introduced in 2024, which defines specific technical conditions for experimental IOL analysis on optical benches.

A commercial optical bench is the OptiSpheric IOL PRO2 (Trioptics GmbH, Wedel, Germany), which was used, for example, by Borkenstein et al., for MTF analysis of several IOL designs.[42] Ravalico et al. were among the first to use a specifically designed optical bench to calculate energy efficiencies of IOLs from 2D-PSF images.[43] Several authors currently use optical benches for MTF or through-focus intensity analysis of different IOLs.[44–48]

The ANSI Z80.35:2018 (Unpublished data, 2014) and ISO 11979-2:2024[4] define specifications for a model eye. Based on these specifications, a polychromatic analysis of the IOL is then carried out to generate a polychromatic MTF, which in turn is used to predict visual acuity. However, absolute longitudinal chromatic aberrations, as they might be influenced by an inappropriate model cornea, are not relevant here as we do not predict the polychromatic visual acuity. Generally, a phase profile of the diffraction surface of the IOL is sufficient to describe these influences discussed here.

Monofocal IOLs use the principle of refraction to correct vision for a single distance. Refractive multifocal IOLs incorporate different zones of varying optical power to create multiple foci. For refractive IOLs, these NIR-light-using systems presumably do not pose a problem in determining optical properties since the PSF and, thus the Airy disk of refractive lenses scale with wavelength. Hence, this allows the optical properties at wavelengths in the NIR spectrum to be recalculated for green light, for which IOLs are generally designed. At great distances and using small-angle approximation, the angle θ between non-diffracted light and the first intensity minimum of the diffracted light is given by:

$$\theta \approx 1.22\frac{\lambda}{d} \tag{2}$$

Here, λ is the wavelength, and d is the aperture diameter. This approach is valid for refractive lenses but not DMIOLs. They usually consist of a refractive base shape, serving for the far focus, with a topographical diffractive ring pattern applied on the lens surface that creates additional focal points. These additional foci are based on constructive interference due to the specific step heights of the ring pattern, inducing appropriate phase shifts. Often, the step heights are calculated for green light.

In this context, longitudinal chromatic aberration (LCA) manifests in two different ways. First, in a nonlinear wavelength dependence of the focal length based on the refractive nature of the far focus, and second, in the case of DMIOLs, in a linear wavelength dependence of near and intermediate foci due to the diffractive nature of these foci. Because

translational vision science & technology

Downloaded from tvst.arvojournals.org on 10/17/2025

near and intermediate focus are based on the nonlinearly wavelength dependent refractive base power and linearly wavelength dependent diffractive add power, the total refractive power arises from the linearly and nonlinearly wavelength dependent effects.

The pupil-dependent foci presumably shift due to spherical aberration and the illumination of different optical zones of the IOL. Wavelength-dependent shifts of the far focus result from the lens material's inherent chromatic properties and the amount of chromatic aberration induced by the model cornea. The same holds true for the near and intermediate foci with an additional axial shift due to the superposition with the diffractive chromatic aberration of the respective add powers. For the intermediate focus we observed almost no pupil size dependent shift when comparing both pupil sizes in Figure 4 or the shift over eight pupil sizes in in Figure 3 and only a minimal wavelength dependent shift of approximately 0.1 mm in Figure 4. It seems that the intermediate focus shift is only minimally influenced by the wavelength for the measurement data since the diffractive proportion of the LCA and the refractive proportion of the LCA are apparently similar and cancel each other out. The near focus experiences an axial shift to smaller values because of the diffractive LCA of the respective add powers.

The imaging performance of DMIOLs depends on the wavelength in multiple ways. Fiala et al.[34] and Faklis et al.[35] provide a detailed analytical description of the diffractive working principles. The key concepts of these theoretical studies are explained in the following. First, the add-power increases linearly with wavelength. The zeroth diffraction order is used for distance vision and is not affected by diffractive chromatic dispersion effects. This applies for the investigated DMIOL with its far focus produced by the refractive base lens and the zeroth orders of the two diffractive profiles. The analysis demonstrates that the add-power(s) of diffractive multifocal lenses is linearly dependent on the ratio of λ_F/λ_0, where λ_F is the analysis wavelength and λ_0 the design wavelength of the IOL. Any measurement of add powers and associated defocus curves must consider the wavelength-dependent scaling of the diffractive add-power. Erroneous measurement may result if this is done improperly. Because the near and intermediate focus of the investigated DMIOL are produced by the 1st order of the 2nd diffraction profile and the first order of the 1st diffraction profile,[38] respectively. The longer the wavelength, the greater the distance between the additional and the far focus due to the add-power dependent focus shift (see Figs. 3 and 4). Furthermore, the wavelength-dependent focal shift scales with the add power. This is observed by the stronger dependence of the near focus compared to the intermediate focus. However, the exact position of the single foci itself is irrelevant here and may be influenced by the model cornea.

A second important aspect is the wavelength dependence of diffraction efficiency. It defines the proportion of incoming light at a given wavelength is distributed in a particular diffraction order and its associated add-power. Measurement data and simulation of the used DMIOL show that with increasing wavelength, more light is distributed into the far focus (see Figs. 4 and 5). Multifocal IOL designs use at least two significantly effective diffraction orders to create bifocal optics or three significantly effective diffraction orders to create trifocal IOLs. Four or more diffraction orders can be used to create quadrifocal or even higher-focal optical designs. The AcrySof IQ PanOptix IOL (Alcon, Geneva, Switzerland), for example, uses a quadrifocal approach.[49] The used diffraction orders for vision are typically, but not necessarily, neighboring diffraction orders. As stated before, the design of DMIOLs is generally conducted at a design wavelength λ_0.

A metric for the performance analysis of DMIOLs is the energy efficiency mentioned above, as it considers scattering, aberration, and out-of-focus images for each focus. In 2023, Vega et al.[8] analyzed the same diffractive trifocal IOL among others, employing the so called "light-in-the-bucket metric" to calculate energy efficiencies. In contrast, our method uses a Gaussian fitting function and additionally presents through-focus curves. Notably, the relationship between energy efficiencies ratios derived from experimental and simulation data is consistent across both setups but the magnitudes differ. Table 3 comprises the findings of Vega et al.[8] and our study on the AT LISA tri 839MP and compares the measured and simulated energy efficiencies of near, intermediate, and far focus, as well as the ratios of the near-to-far and intermediate-to-far focus energy efficiency. For instance, our approach assigns more energy to the near focus than the far focus compared to the measurements of Vega et al.,[8] likely because of the differing methods used to determine energy efficiencies. Notably, the sum of the foci's energy efficiencies never reaches 100% because of a loss of energy caused by halos, aberrations, and light scattering. The definition of energy efficiency is not standardized, and several approaches exist to define it. The energy efficiency values vary between our measurement and simulation. Although the experimental values were determined by the above-described Gaussian method, the simulated efficiency is the squared total of the electric field amplitudes in the respective image distance after calculating the

Downloaded from tvst.arvojournals.org on 10/17/2025

Table 3. Energy Efficiencies of AT LISA tri 839 MP for Each Focus at IOL Pupil 4.5 Mm Compared Between Vega et al.[8] and Our Results

	Near Focus		Intermediate Focus		Far Focus	
	Visible	NIR	Visible	NIR	Visible	NIR
Measurement						
Vega et al.[8]	0.27	0.16	0.18	0.08	0.47	0.75
Ratio	57%	21%	38%	10%		
This paper	0.25	0.14	0.18	0.09	0.34	0.58
Ratio	73%	24%	52%	15%		
Simulation						
Vega et al.[8]	0.25	0.11	0.15	0.07	0.43	0.61
Ratio	58%	18%	34%	11%		
This paper	0.15	0.1	0.11	0.07	0.21	0.52
Ratio	71%	19%	52%	14%		

The ratios are defined as near-to-far focus and intermediate-to-far focus energy efficiency for each wavelength. Visible corresponds to $\lambda_c = 530$ nm, NIR corresponds to $\lambda_c = 780$ nm.

diffraction integral according to Fiala et al.[34] However, because optical power or photometric quantities are not included in the simulation, the absolute values are arbitrarily scaled. Therefore we compare the experimentally determined efficiency ratios of the different foci with the simulated ones finding a good agreement. Whereas Vega et al.[8] used topographical data of the IOL surface measured with confocal microscopy to simulate the IOL performance[8], we use the manufacturer's genuinely designed diffractive surface topographies for the optics simulation and the formulas from Fiala et al.[34]

Furthermore, our study reports different near focus add powers compared to the findings in Vega et al.,[8] who used the same wavelengths and pupil sizes in their study. We observed 5.03 dpt for NIR light and 3.4 dpt for green light, compared to 4.8 dpt and 3.3 dpt, respectively. This discrepancy may be attributed to the difference in base power of the investigated trifocal IOL, the deviation of the illuminated IOL diameter (consequently variable illuminated optical zones) and different diffractive surface profiles.

To estimate the wavelength-dependent focal positions 546 nm, as defined by the ISO standard 11979-2:2024, we used a cubic function to fit the axial focus positions to the wavelength. Especially for small wavelength ranges, we found an almost linear dependence. Exemplary for pupil of 4.5 mm ($d_{IOL} = 3.80$ mm), the far, near and intermediate foci were shifted by 14 µm, −3 µm and −19 µm, respectively. Our measurement data shows a broadening of the near, intermediate, and far focus for each pupil size with increasing wavelength. The simulation data does not show that behavior. Further, the intermediate focus, which shifts to smaller axial positions in the simulation, shifts to greater positions in the experiment (see Fig. 4). This may have different mutually complementary reasons (e.g., decentration or imprecise determined distances of the model eye). Although the far focus appears similar for all wavelengths at the small pupil size, the far focus with blue light is wider in the simulation compared to the experiment with the larger pupil size. Nevertheless, the wavelength dependence of the diffraction efficiency and diffractive orders of the investigated DMIOL is observable for both—simulation and measurement.

Our demonstration that a diffractive trifocal IOL can become almost monofocal using NIR light highlights the potential source of error and risk when using such wavelengths as integrated in devices designed to determine the vision quality. Hence, caution is required to conclude visual assessment obtained by NIR-based methods—the results of lower- and higher-order aberrations are likely to be wrong. Our findings agree with previously established theoretical works on diffractive power and diffraction efficiency and show that the diffraction orders of a diffractive IOL are particularly shifted under NIR light.[34,35] Therefore an optical performance assessment with NIR light will lead to erroneous assumptions of the DMIOLs near or intermediate-focus performance and may lead to misleading recommendations for the implantation of DMIOLs. Hence, visible light, preferably green light (around 520-570 nm), must be used. Low-intensity levels within this spectrum are recommended to minimizing glare and discomfort. However,

translational vision science & technology

Downloaded from tvst.arvojournals.org on 10/17/2025

the low retinal reflectance may be challenging for the light detection.

To the best of our knowledge, measuring diffractive optics with wavefront sensors poses a general challenge. This is because multiple wavefronts, including those from higher diffraction orders, converge on the microlenses of the wavefront sensor, generating numerous points. Consequently, it becomes difficult to unambiguously associate these points with the correct focal point.

The key distinction of our study compared to previous research using experimentally obtained topography data for their simulation is that we used the manufacturer's theoretically designed surface topography data of the AT LISA tri 839MP. This allowed us to achieve the most accurate optical simulation data for this commonly implanted DMIOL and to provide further evidence of focal wavelength dependence by analyzing four different wavelengths. Please note that the exact change in energy efficiency depends on the exact lens design. Hence, not all statements can be generalized for every diffractive IOL. Keep in mind that diffractive IOLs may only be examined with visible light, for which they were developed. In particular, postoperative assessment of the quality of vision of DMIOLs under NIR light must inevitably produce incorrect results. In this case, conclusions on the in vivo imaging performance of DMIOLs in publications that have already been published cannot be considered reliable.

Acknowledgments

Supported by DFG grant number 469107515.

Presented at the Deutsche Ophthalmologische Gesellschaft (DOG) conference, Berlin, Germany, September 29 to October 2, 2022.

Disclosure: **R. Elsner**, None; **M. Gerlach**, Carl Zeiss Meditec AG (E); **S. Bohn**, None; **J. Sievers**, None; **H. Stolz**, None; **R.F. Guthoff**, None; **O. Stachs**, None; **K. Sperlich**, None

References

1. Davison JA, Simpson MJ. History and development of the apodized diffractive intraocular lens. *J Cataract Refract Surg*. 2006;32:849–858.
2. Alió JL, Pikkel J, eds. *Multifocal Intraocular Lenses: The Art and the Practice*. Berlin: Springer International Publishing; 2019.
3. I. O. for Standardization. ISO/CIE 23539:2023 | CIE TC 2-93 - Photometry—The CIE system of physical photometry. Available at: https://www.iso.org/obp/ui/#iso:std:iso-cie:23539:ed-1:v1:en:ref:4:~:text=This%20document%20was%20prepared%20by,CIE%20170%2D2:2015. Accessed April 16, 2025.
4. I. O. for Standardization. I. O. for Standardization, ISO 11979-2:2024. *ISO*. Available at: https://www.iso.org/standard/55682.html. Accessed April 16, 2025.
5. Sievers J, Elsner R, Bohn S, et al. Method for the generation and visualization of cross-sectional images of three-dimensional point spread functions for rotationally symmetric intraocular lenses. *Biomed Opt Express*. 2022;13:1087–1101.
6. Petelczyc K, Kolodziejczyk A, Błocki N, et al. Model of the light sword intraocular lens: in-vitro comparative studies. *Biomed Opt Express*. 2020;11:40–54.
7. Vega F, Millán MS, Vila-Terricabras N, Alba-Bueno F. Visible versus near-infrared optical performance of diffractive multifocal intraocular lenses. *Invest Ophthalmol Vis Sci*. 2015;56:7345–7351.
8. Vega F, Faria-Ribeiro M, Armengol J, Millán MS. Pitfalls of using NIR-based clinical instruments to test eyes implanted with diffractive intraocular lenses. *Diagnostics*. 2023;13:1259.
9. Ginis HS, Tsoukalas S, Christaras D, Artal P. Visually relevant on-bench through-focus analysis of intraocular lenses. *Biomed Opt Express*. 2024;15:7056.
10. Jun I, Choi YJ, Kim EK, Seo KY, Kim T. Internal spherical aberration by ray tracing-type aberrometry in multifocal pseudophakic eyes. *Eye*. 2012;26:1243–1248.
11. Santhiago M, Netto M, Barreto J, Gomes B, Schaefer A, Kara-Junior N. Wavefront analysis and modulation transfer function of three multifocal intraocular lenses. *Indian J Ophthalmol*. 2010;58:109–113.
12. Pilger D, Homburg D, Brockmann T, Torun N, Bertelmann E, Von Sonnleithner C. Clinical outcome and higher order aberrations after bilateral implantation of an extended depth of focus intraocular lens. *Eur J Ophthalmol*. 2018;28:425–432.
13. Seo JG, Choi MJ, Seo KY, Kim EK, Kim TI. Clinical outcomes of patients fitted with bifocal and trifocal diffractive intraocular Lenses. *J Korean Ophthalmol Soc*. 2018;59:325–331.
14. Haddad JS, Gouvea L, Ferreira JL, Ambrósio R, Waring GO, Rocha KM. Impact of a chromatic

translational vision science & technology

Downloaded from tvst.arvojournals.org on 10/17/2025

aberration-correcting intraocular lens on automated refraction. *J Refract Surg*. 2020;36:334–339.
15. Ju RH, Wu ZM, Aier Eye Hospital, Jinan University, Guangzhou 510071, Guangdong Province, China, *et al.* Comparison of visual performance with iTrace analyzer following femtosecond laser-assisted cataract surgery with bilateral implantation of two different trifocal intraocular lenses. *Int J Ophthalmol*. 2023;16:1773–1781.
16. Mojzis P, Kukuckova L, Majerova K, Liehneova K, Piñero DP. Comparative analysis of the visual performance after cataract surgery with implantation of a bifocal or trifocal diffractive IOL. *J Refract Surg*. 2014;30:666–672.
17. Velasco-Barona C, Corredor-Ortega C, Mendez-Leon A, et al. Influence of angle κ and higher-order aberrations on visual quality employing two diffractive trifocal IOLs. *J Ophthalmol*. 2019;2019(1):7018937.
18. Garzón N, García-Montero M, López-Artero E, Poyales F, Albarrán-Diego C. Influence of trifocal intraocular lenses on standard autorefraction and aberrometer-based autorefraction. *J Cataract Refract Surg*. 2019;45:1265–1274.
19. García-Bella J, Ventura-Abreu N, Morales-Fernández L, et al. Visual outcomes after progressive apodized diffractive intraocular lens implantation. *Eur J Ophthalmol*. 2018;28:282–286.
20. Carballo-Alvarez J, Vazquez-Molini JM, Sanz-Fernandez JC, et al. Visual outcomes after bilateral trifocal diffractive intraocular lens implantation. *BMC Ophthalmol*. 2015;15:26.
21. Alió JL, Plaza-Puche AB, Alió Del Barrio JL, et al. Clinical outcomes with a diffractive trifocal intraocular lens. *Eur J Ophthalmol*. 2018;28:419–424.
22. Moreno LJ, Piñero DP, Alió JL, Fimia A, Plaza AB. Double-pass system analysis of the visual outcomes and optical performance of an apodized diffractive multifocal intraocular lens. *J Cataract Refract Surg*. 2010;36:2048–2055.
23. Lee YW, Choi CY, Moon K, et al. Clinical outcomes of new multifocal intraocular lenses with hydroxyethyl methacrylate and comparative results of contrast sensitivity, objective scatter, and subjective photic phenomena. *BMC Ophthalmol*. 2022;22:379.
24. Liao X, Lin J, Tian J, Wen B, Tan Q, Lan C. Evaluation of optical quality: ocular scattering and aberrations in eyes implanted with diffractive multifocal or monofocal intraocular lenses. *Curr Eye Res*. 2018;43:696–701.
25. Chen T, Yu F, Lin H, et al. Objective and subjective visual quality after implantation of all optic zone diffractive multifocal intraocular lenses: a prospective, case-control observational study. *Br J Ophthalmol*. 2016;100:1530–1535.
26. Hwang H, Shin HY, Joo C-K. Double-pass system (Optical Quality Analysis System) for analysis of the multifocal function of a diffractive multifocal intraocular lens (Acrysof ReSTOR) compared to a monofocal intraocular lens (Acrysof IQ). *J Opt Soc Korea*. 2014;18:110–117.
27. Castillo-Gómez A, Carmona-González D, Martínez-de-la-Casa JM, Palomino-Bautista C, García-Feijoo J. Evaluation of image quality after implantation of 2 diffractive multifocal intraocular lens models. *J Cataract Refract Surg*. 2009;35:1244–1250.
28. Fernández J, Burguera N, Rocha-de-Lossada C, Rachwani-Anil R, Rodríguez-Vallejo M. Influence of a multifocal intraocular lens centration and eye angles on light distortion and ocular scatter index. *Graefes Arch Clin Exp Ophthalmol*. 2023;261:2291–2299.
29. Van Norren D, Tiemeijer LF. Spectral reflectance of the human eye. *Vis Res*. 1986;26:313–320.
30. International Commission on Non-Ionizing Radiation Protection. Revision of guidelines on limits of exposure to laser radiation of wavelengths between 400 nm and 1.4 microm. *Health Phys*. 2000;79:431–440.
31. Charman WN, Montes-Mico R, Radhakrishnan H, Papadopoulos R, Bachariou A. Can we measure wave aberration in patients with diffractive IOLs? *J Cataract Refract Surg*. 2007;33:1997.
32. Campbell CE. Wavefront measurements of diffractive and refractive multifocal intraocular lenses in an artificial eye. *J Refract Surg*. 2008;24:308–311.
33. Gatinel D. Double pass–technique limitations for evaluation of optical performance after diffractive IOL implantation. *J Cataract Refract Surg*. 2011;37:621–622.
34. Fiala W, Pingitzer J. Analytical approach to diffractive multifocal lenses. *Eur Phys J Appl Phys*. 2000;9:227–234.
35. Faklis D, Morris GM. Spectral properties of multiorder diffractive lenses. *Appl Opt*. 1995;34:2462.
36. Barbero S, Marcos S, Montejo J, Dorronsoro C. Design of isoplanatic aspheric monofocal intraocular lenses. *Opt Express*. 2011;19:6215.
37. Frey K, Hage H, Gerlach M, Brunner R. Topography Profiling: Measuring the topography of soft ophthalmological components immersed in water. *Opt Photon*. 2015;10(5):27–30.
38. Loicq J, Willet N, Gatinel D. Topography and longitudinal chromatic aberration characterizations of refractive–diffractive multifocal intraocu-

translational vision science & technology

Downloaded from tvst.arvojournals.org on 10/17/2025

lar lenses. *J Cataract Refract Surg*. 2019;45:1650–1659.

39. Mendroch D, Altmeyer S, Oberheide U. Characterization of diffractive bifocal intraocular lenses. *Sci Rep*. 2023;13:908.
40. Gerlach M, Guthoff R, Stachs O, Bohn S, Sperlich K. Präklinische Bewertung von Intraokularlinsen durch simulierte Implantation. *Klin Monatsbl Augenheilkd*. 2018;235:1332–1341.
41. Brezna W, Lux K, Dragostinoff N, et al. Psychophysical vision simulation of diffractive bifocal and trifocal intraocular lenses. *Trans Vis Sci Tech*. 2016;5(5):13.
42. Borkenstein AF, Borkenstein EM, Luedtke H, Schmid R. Impact of decentration and tilt on spherical, aberration correcting and specific aspherical intraocular lenses; an optical bench analysis. *Ophthalmic Res*. 2022;65:425–436.
43. Ravalico G, Parentin F, Sirotti P, Baccara F. Analysis of light energy distribution by multifocal intraocular lenses through an experimental optical model. *J Cataract Refract Surg*. 1998;24:647–652.
44. Peli E, Lang A. Appearance of images through a multifocal intraocular lens. *J Opt Soc Am A*. 2001;18:302–309.
45. Castignoles F, Flury M, Lepine T. Comparison of the efficiency, MTF and chromatic properties of four diffractive bifocal intraocular lens designs. *Opt Express*. 2010;18:5245–5256.
46. Hill W, Carson D, Hong X, Karakelle M. Optical bench performance of AcrySof IQ ReSTOR, AT LISA tri, and FineVision intraocular lenses. *Clin Ophthalmol*. 2014:8:2105–2113.
47. Kawamorita T, Uozato H. Modulation transfer function and pupil size in multifocal and monofocal intraocular lenses in vitro. *J Cataract Refract Surg*. 2005;31:2379–2385.
48. Lee S, Choi M, Xu Z, Zhao Z, Alexander E, Liu Y. Optical bench performance of a novel trifocal intraocular lens compared with a multifocal intraocular lens. *Clin Ophthalmol*. 2016;10:1031–1038.
49. Kohnen T, Herzog M, Hemkeppler E, et al. Visual Performance of a Quadrifocal (Trifocal) Intraocular Lens Following Removal of the Crystalline Lens. *Am J Ophthalmol*. 2017;184:52–62.

translational vision science & technology

Downloaded from tvst.arvojournals.org on 10/17/2025